OPTICAL SPECTROSCOPY FOR THE EVALUATION OF SURGICAL MARGIN STATUS

FOLLOWING BREAST CANCER RESECTION

By

Matthew David Keller

Dissertation

Submitted to the Faculty of the

Graduate School of Vanderbilt University

in partial fulfillment of the requirements

of the degree of

DOCTOR OF PHILOSOPHY

in

Biomedical Engineering

December, 2009

Nashville, Tennessee

Approved:

Professor Anita Mahadevan-Jansen

Professor Mark C. Kelley

Professor E. Duco Jansen

Professor Todd D. Giorgio

Professor Thomas E. Yankeelov

Professor Robert L. Galloway

ACKNOWLEDGMENTS

TABLE OF CONTENTS

LIST OF FIGURES

CHAPTER I

INTRODUCTION

1.1 Motivation and Objectives

Of the approximately 180,000 patients each year diagnosed with early-stage invasive breast cancer or breast carcinoma *in situ* [1], most have the option of breast conserving therapy (BCT). This method consists of removing the primary breast lesion via a partial mastectomy, or lumpectomy, which is often followed by directed radiotherapy. Several prospective, randomized studies have demonstrated equivalent 10-year survival for BCT versus total mastectomy [2], and BCT provides superior functional and aesthetic results. To be successful, the surgical portion of BCT must ensure that no tumor cells remain within a specified distance (typically 1 or 2 millimeters) of the surgical margin on the excised specimen; in this case, the margins are said to be negative. The presence of tumor-positive margins is strongly correlated with the risk of local tumor recurrence and necessitates a second operation for the patient [3].

Currently available methods of evaluating margin status intraoperatively include visual inspection of the excised tissue by the surgeon, which is incorrect in at least 25 % of cases [4]. Frozen section pathology and cytological examination ("touch prep") are commonly used but require tissue to be sent to pathology and are prone to sampling error [4, 5]; additionally, "touch prep" only samples the specimen superficially. While ultrasound is available in the operating room, its poor spatial resolution results in limited sensitivity [4, 6]. The current gold standard in margin analysis is serial sectioning with standard histopathology, but results may take several days to over a week. These limitations emphasize the need for a real-time, intraoperative margin

1

evaluation tool that can assure complete removal of breast tumors with negative margins in a single procedure.

Optical spectroscopy has the potential to be such a tool because it can provide automated, fast, non-invasive classification of a tissue's histopathological status. The overall objective of this project therefore was to develop the use of optical spectroscopy to improve the intraoperative evaluation of surgical margin status during breast conserving therapy. Preliminary results indicated that both Raman spectroscopy and combined autofluorescence and diffuse reflectance spectroscopy can rapidly and accurately discriminate normal from malignant breast tissues. Both modalities were pursued further due to their unique advantages that would be desirable features in a margin analysis tool – combined fluorescence and reflectance can be adapted into a macroscopic spectral imaging device to interrogate larger regions of tissue, and Raman spectroscopy can "look" further beneath the surface of tissue to evaluate margins to a greater depth.

1.2 Specific Aims

Specific Aim (1): Characterize the ability of combined fluorescence and diffuse reflectance spectroscopy and spectral imaging to evaluate the surgical margin status of excised breast tissues _ex vivo_ in the operating room. A portable fluorescence and reflectance spectroscopy system was used in a clinical setting to take measurements from excised breast specimens. Spectra were recorded from the surface of the specimen, with one measurement from each of the six facets of the tissue (when thought of as a cuboidal shape), plus additional measurements at the surgeon's discretion. A multivariate statistical technique was used to classify the tissues as normal or malignant, and therefore whether the margins were tumor-positive or tumor-free

2

(negative). The feasibility of examining larger areas was investigated by obtaining 25 mm by 25 mm fluorescence- and reflectance-based multi-spectral images. Methods to increase the depth information in these measurements were pursued as well.

Specific Aim (2a): Characterize the relationship between source-detector separation and depth of interrogation in spatially offset Raman spectroscopy (SORS) of breast tissues. In previous results, both in our lab and others', Raman spectroscopy has provided superior classification results compared with fluorescence and reflectance for breast tissues. It is exceedingly difficult to use in an imaging modality due to its weak signal and equipment limitations, but it can gather signal from deeper regions than fluorescence and reflectance can. In particular, SORS is a new technique shown to be capable of recovering Raman spectra from bone below several millimeters of soft tissue, but it had not previously been used for examining layered soft tissues. The relationship between source-detector separation and depth of interrogation with SORS for breast tissues was investigated with tissue constructs consisting of varying thicknesses of normal breast tissue overlying breast tumors.

Specific Aim (2b): Model the relationship between source-detector separation and depth of interrogation in spatially offset Raman spectroscopy (SORS) of breast tissues. A Monte Carlo simulation model of SORS was also developed to validate experimental results and to investigate factors that would be difficult to precisely examine experimentally, such as how various tissue geometries affect the measured SORS signals.

Specific Aim (3) Design and test a SORS probe for evaluating margin status in the operating room. Using results from aim 2, a fiber optic-based SORS probe with multiple

source-detector separations was designed to interrogate breast tissue up to the clinically relevant 2 mm depth. The probe was tested with layered tissue constructs to ensure its depth performance. It was then used to obtain spectra from heterogeneous breast tissue samples *ex vivo* to validate this approach in intact tissue specimens rather than in layered constructs. A small pilot study to use SORS for evaluating margin status in the clinic was then completed to ensure this technique's applicability in such an environment.

1.3 Summary of Chapters

Following this introductory chapter, chapter II provides relevant background information on breast cancer, surgical margin evaluation, and several aspects of optical spectroscopy.

Chapter III provides details of a preliminary study that provided the basis of this work by comparing the performances of Raman spectroscopy and combined autofluorescence and diffuse reflectance spectroscopy in classifying breast tissue samples.

Chapter IV is the first manuscript in the main body of this dissertation. It details the results of the clinical reflectance and fluorescence measurements. It also shows the feasibility of performing multi-spectral imaging and examines the effects of chemotherapy on the spectral measurements.

Chapter V is a short, letter-style manuscript containing the first experimental demonstration of being able to discriminate layered soft tissues (normal breast over breast tumor) using SORS.

Chapter VI details the development of a Monte Carlo code that was first validated by having it produce results equivalent to the experimental ones from Chapter V. It was then used to examine the effects on the inclusion of quartz coverslip layers in the experimental data, and to

see how the spectral responses change as both the overlying normal layer and the tumor layer change thicknesses.

Chapter VII contains details of the acquired SORS probe and its depth-testing results. It then demonstrates the ability of SORS (using this probe) to accurately classify breast tissues as normal or malignant up to 2 mm below the measurement surface on both tissue specimens in the laboratory and on freshly excised tissues in the clinic.

Chapter VIII provides a summary of the major results presented in this dissertation and recommended future directions for this project. It also contains information about my impact on the field and on society with this research.

1.4 References

1.   American Cancer Society, "Cancer Facts and Figures 2009," (American Cancer Society, Atlanta, 2009).

2.   E. B. C. T. C. Group, "Effects of radiotherapy and surgery in early breast cancer. An overview of the randomized trials.," N Engl J Med **333**, 1444-1455 (1995).

3.   K. C. Horst, M. C. Smitt, D. R. Goffinet, and R. W. Carlson, "Predictors of local recurrence after breast-conservation therapy," Clin Breast Cancer **5**, 425-438 (2005).

4.   G. C. Balch, S. K. Mithani, J. F. Simpson, and M. C. Kelley, "Accuracy of intraoperative gross examination of surgical margin status in women undergoing partial mastectomy for breast malignancy," Am Surg **71**, 22-27; discussion 27-28 (2005).

5.   N. Cabioglu, K. K. Hunt, A. A. Sahin, H. M. Kuerer, G. V. Babiera, S. E. Singletary, G. J. Whitman, M. I. Ross, F. C. Ames, B. W. Feig, T. A. Buchholz, and F. Meric-Bernstam, "Role for intraoperative margin assessment in patients undergoing breast-conserving surgery," Ann Surg Oncol **14**, 1458-1471 (2007).

6.   V. S. Klimberg, S. Harms, and S. Korourian, "Assessing margin status," Surg Oncol **8**, 77-84 (1999).

CHAPTER II

BACKGROUND

2.1 Normal Breast Tissue

As seen in Figure 2.1, the normal adult human breast consists of a variety of structures, attached to the pectoralis muscle anterior to the chest wall. The primary functional unit of the breast is often called the "terminal duct-lobular unit," and consists of the lobules that produce
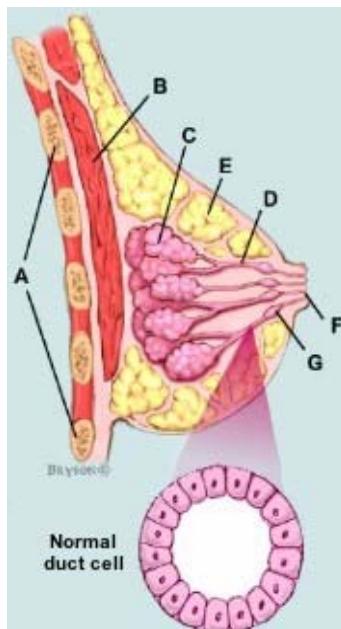
Figure 2.1 Normal breast anatomy. A – chest wall, B – pectoralis muscle, C – lobules, D – ducts, E – adipose tissue, F – nipple,   G – lactiferous sinuses

milk in response to prolactin stimulation, as well as the terminal ducts that carry milk to the nipple. The lobules are generally clustered into 15-20 lobes, drained by a converging series of ducts that open up into larger sinuses near the nipple to store milk. A normal duct has a lumen of approximately 2 mm in diameter surrounded by a layer of epithelial cells. These functional units

of the breast are encompassed and held in place by stromal tissue, consisting of both adipose

tissue and fibrous tissue. As a woman ages, this stromal component becomes less dense as more

fibrous tissue is replaced by fatty tissue. The extensive lymphatic system found in the breast

typically drains toward the axillary lymph nodes [1].

2.2 Breast Disease

Breast cancer is the most common cancer found in women in the United States, with an

estimated 240,000 new cases diagnosed in 2009. It is also the second leading cause of cancer

deaths in women, behind only lung cancer, estimated to be responsible for the deaths of over

40,000 women in the U.S. in 2009 [2]. The most common breast malignancy by far is invasive

ductal carcinoma (IDC), also called invasive mammary carcinoma – no special type, which

accounts for around 75-80% of invasive breast cancers. As shown in Figure 2.2, IDC occurs
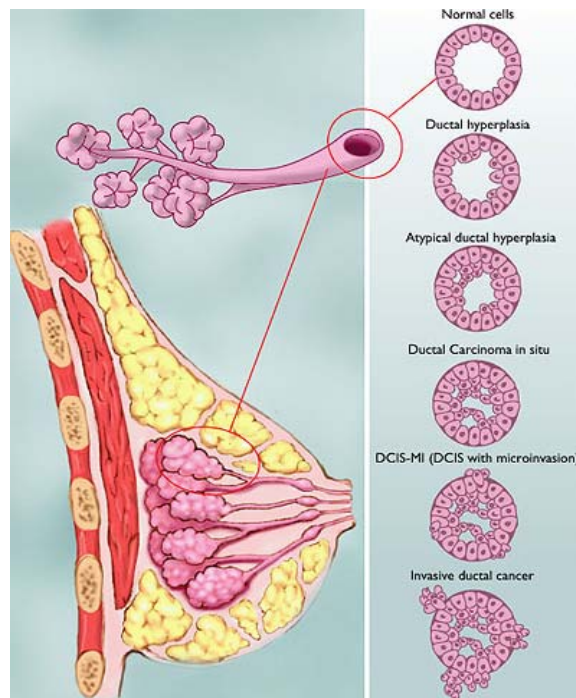
Figure 2.2 Progression of ductal lesions in the breast.

when malignant ductal epithelial cells invade past the basement membrane into the stromal tissue of the breast. If not detected early enough, these invasive cells can metastasize, most often to the lymph nodes, bones, lungs, or liver. As represented in Figure 2.2, ductal carcinoma *in situ* (DCIS) is an increasingly commonly diagnosed non-invasive neoplasm that presents a high risk of developing into invasive ductal carcinoma. It accounts for around 20% of all diagnosed breast cancers, when invasive and non-invasive cases are considered together. As DCIS progresses, microcalcifications often form, which are easily detected upon mammography, a major reason for its increased rate of diagnosis. From Figure 2, another early precursor lesion to ductal carcinomas is ductal hyperplasia, which occurs when normal epithelial cells lining the ducts begin to grow too much. If the cells start to lose some normal characteristics but are not yet considered DCIS, this benign condition becomes known as atypical ductal hyperplasia [3].

The other major form of invasive breast cancer is invasive lobular carcinoma (ILC), which accounts for 5-10% of invasive cases. As shown in Figure 2.3, it arises from malignant
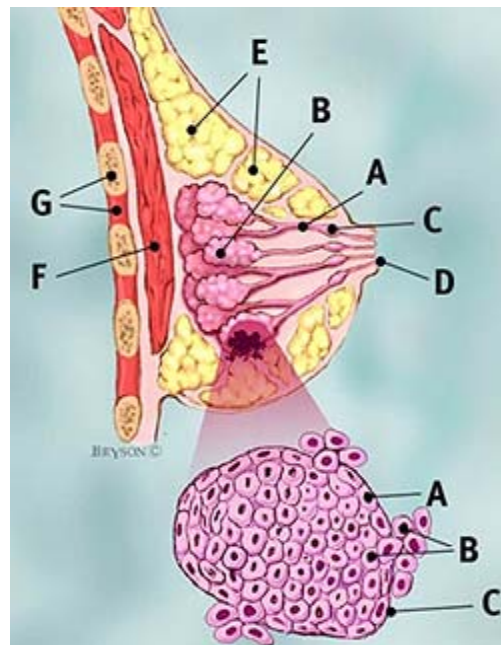
Figure 2.3 Representation of the histo-pathology of ILC. For close-up, A – normal cell, B – malignant cells, C – basement membrane

lobular cells invading past the basement membrane into the stroma. Unlike IDC, though, ILC tends to be a more diffuse disease, rather than forming a hard, fibrous tumor mass as often occurs with IDC. Lobular carcinoma *in situ* (LCIS) is similar to ILC, minus the invasive aspect, but generally presents no obvious clinical symptoms. Like DCIS, it indicates a woman is at risk for developing invasive cancer, but often it will be IDC and not necessarily ILC [3].

Several other forms of breast cancers exist, but are rarer than IDC, DCIS, ILC, and LCIS. Inflammatory breast cancer occurs when malignant cells block lymph vessels to cause swelling and inflammation and accounts for about 2% of all breast cancers. Paget's disease presents clinically with itching, swelling, and redness around the nipple, similar to eczema, but is usually concurrent with an underlying carcinoma. It accounts for 1-4% of all breast cancer cases. Other types that will not be discussed further include medullary, tubular, and mucinous carcinomas [3].

Several benign tumors are found in the breast as well. The most common one is fibroadenoma (FA), an encapsulated tumor that is most prevalent in young women. Fibroadenomas include both glandular (ductal and lobular epithelial cells) and stromal (collagen and other proteins) tissues. They usually present as a large, firm mass that can be mistaken for cancer upon initial examination, and they are often removed, although they typically only indicate a slightly higher risk for developing invasive cancer. Other benign tumors include Phyllodes tumors and papillomas. A single papilloma without atypical hyperplasia is generally not a significant risk factor for the development of invasive cancer, but multiple papillomas or ones with a good deal of accompanying atypical hyperplasia do generally indicate an increased risk of cancer [1].

Besides the benign tumors discussed above, the breast is also susceptible to several benign conditions not characterized as tumors. The terms fibrocystic change or fibrocystic

disease are fairly vague terms whose utility is debated among clinicians. They generally refer to the formation of cysts, apocrine changes in cells lining such cysts, and fibrosis. In general, these conditions are not considered a risk for the development of cancer. Fibrocystic change may sometimes also refer to hyperplasia, discussed above, or adenosis, an enlarging of the lobules. One particular example of the latter is sclerosing adenosis, in which fibrous tissue becomes interspersed within the lobules, mimicking invasive cancer; this is associated with a slightly increased risk of developing invasive cancer. Other benign conditions, which generally do not indicate an increased risk of invasive cancer, include fat necrosis, mastitis, and duct ectasia [1].

2.3 Breast Cancer Treatment

For most cases of breast cancer, surgical removal is the preferred method of treatment. Chemotherapy and radiation therapy are often used as well, though typically in conjunction with surgical treatment. In particular, chemotherapy can be used either after surgery to minimize the risk of recurrence, or in a neo-adjuvant manner to shrink the tumor prior to surgery. Other treatments include hormonal therapy, especially tamoxifen to limit the effects of estrogen on tumors whose growth is stimulated by estrogen, and targeted therapies against specific receptors, like Herceptin®, and against angiogenesis, like Avastin® [1].

The exact course of treatment for a breast cancer patient is determined by many factors, including the stage of disease present. Most of the approximately 180,000 breast patients diagnosed with early-stage (0, I, or II) invasive cancer or carcinoma *in situ* have the option of breast conserving therapy (BCT), a procedure that provides superior functional and aesthetic results compared with total mastectomy. This method of treatment involves a "lumpectomy," or the local excision of the primary breast lesion with clear tumor-free margins, as shown in the

"negative margins" case in Figure 2.4. This partial mastectomy, as it is also called, is typically followed by radiotherapy for optimal management of the disease. Several prospective,
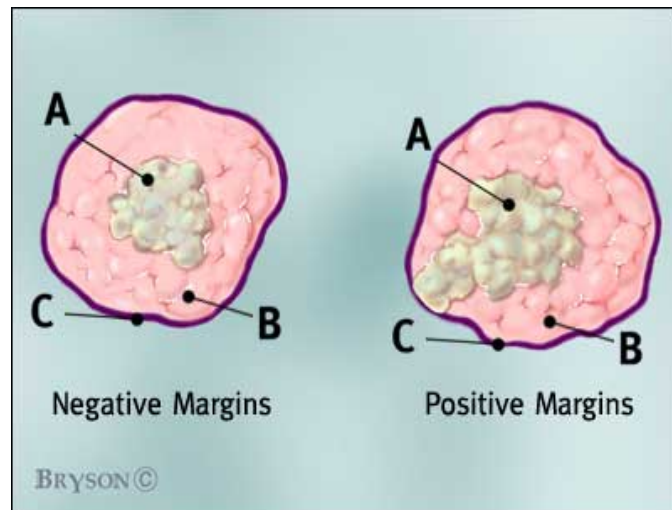
Figure 2.4 Demonstration of negative versus positive margins following a lumpectomy. A – tumor tissue, B – normal tissue, C – surgical margin

randomized studies, examined by the Early Breast Cancer Trialists' Collaborative Group, demonstrated no difference in 10-year survival for BCT versus total mastectomy [4], making it a viable option for many patients. It has also been shown that the presence of tumor within 1-2 mm of the margin, as depicted in the "positive margins" case in Figure 2.4, is strongly correlated with the risk of local tumor recurrence [5]. Margin status therefore plays a key role in the prognosis of the patient. Consequently, there is a need for intraoperative evaluation of the resection front so that immediate re-excision of suspicious margins can be performed. This development would minimize the need for a second surgical procedure, and thereby reduce the risks for the patient and costs for the health care system.

2.4 Surgical Margin Evaluation

Any method used to evaluate the surgical margins around the tumor following BCT must be rapid and relatively simple to implement if it is to be used in routine clinical care. Standard imaging modalities used to screen for or diagnose breast cancer, such as mammography and MRI, are not of use for this application due to their limited spatial resolutions, accuracies, and/or mobility. The simplest currently available technique for determining margin status is based on visual inspection of the excised tissue for evidence of tumor. This method is very rapid and does not require the use of any equipment, but the lack of microscopic detail leads to incorrect diagnoses in around 25% of cases [6]. Serial sectioning with standard histopathology provides a definitive diagnosis of margin status, but results may take several days to more than a week to become available, meaning the patient will go through a period of uncertainty and then require a second operation if tumor-positive margins are found. Other currently available intraoperative techniques include frozen section pathology, imprint cytological examination ("touch prep"), and ultrasound. Frozen section pathology, in which suspicious regions of the resected specimen are frozen and cut into thin sections for examination under a light microscope, is commonly used but is time consuming and prone to sampling error [6, 7]. Touch prep involves smearing the surface of the removed mass on glass slides and examining the superficial cells that stick to the glass. While this method of examination is more accurate than gross examination, it is time consuming and has limited sensitivity, which is also the major drawback of ultrasound due to its poor spatial resolution [6, 8]. In addition, frozen section analysis and touch prep still require the removed specimen be taken to pathology for examination. These limitations emphasize the need for a real-time, intraoperative guidance tool that can accurately differentiate normal breast tissue from tumor tissue at the margins to assure complete removal in a single procedure.

2.5 Optical Spectroscopy

Light-based methods have the potential to provide automated, fast determination of surgical margin status in the operating room during the surgery without disrupting or removing any tissue for such analysis. Although there are several techniques that have been used to investigate breast pathology, including diffuse optical tomography (DOT) and optical coherence tomography (OCT), these two techniques have limited applicability in surgical margin evaluation. This doctoral project used both Raman spectroscopy and combined autofluorescence and diffuse reflectance spectroscopy to achieve the stated aims. The physical principles of all three modalities are shown in the Jablonski diagram in Figure 2.5.
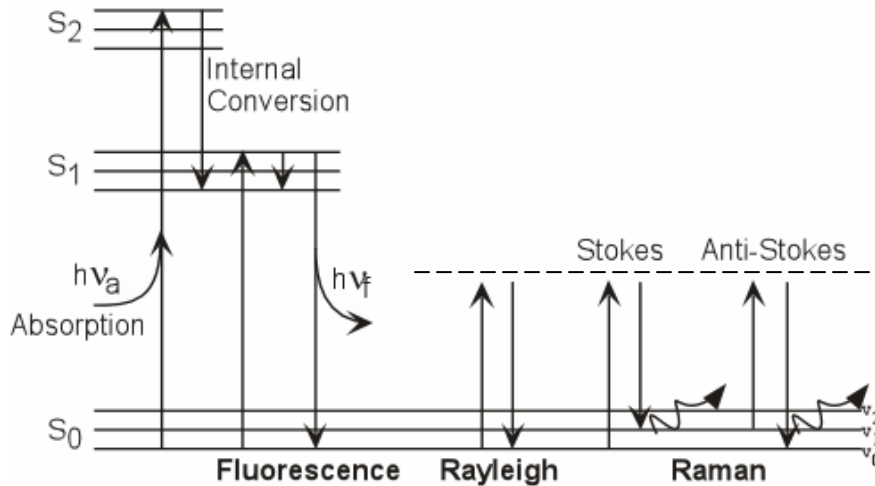
Figure 2.5 Jablonski diagram illustrating physical principles of common optical spectroscopic modalities. S_i refers to electronic energy levels; v_i to vibrational ones. Dashed line represents a virtual excited state.

2.5.1 Fluorescence and diffuse reflectance

Fluorescence and diffuse reflectance have been applied to cancer detection in many other areas of the body, including cervix [9-11], skin [12, 13], and brain [14, 15]. As shown in Figure 2.5, fluorescence involves absorption of a photon, internal conversion (heat dissipation), and then

13

re-release of a photon of lower energy, or a longer wavelength. Fluorescence spectroscopy of biological tissue generally uses ultraviolet or shorter visible wavelengths (violet or blue) for excitation, with emissions across the visible spectrum. One of the most common excitation sources is the nitrogen laser at 337 nm. At this excitation wavelength, the major biological fluorophores contributing to the measured spectra are the structural proteins collagen and elastin, the electron carriers NAD(P)H and FAD, and porphyrins [10]. Using fluorescence spectra for tissue discrimination is possible in part because many tumors cause collagen disorganization, which is apparent in UV-excited fluorescence spectra, and changes in metabolic rate, which are evidenced by differing spectral contributions of molecules like NADH and FAD [10].

Elastic scattering involves an incident photon having its path changed without losing or gaining any energy. This technique, also known as diffuse reflectance when applied to macroscopic samples, provides morphological information about the tissue, such as number and size of scattering nuclei and relative amounts of oxy- and deoxy-hemoglobin. Since these two techniques both have strong signals and provide complementary information (i.e. morphological for reflectance, biochemical for fluorescence), they are often combined to maximize diagnostic potential. While these techniques have experienced success in certain areas, the broad peaks can limit their ability to distinguish among many different classes of disease [16]. In this work, however, only a binary classification scheme is needed since the surgeon needs to know only if the margin is positive or negative.

2.5.2 Raman spectroscopy

Raman spectroscopy utilizes its namesake inelastic scattering, which occurs when an incident photon causes a scattering molecule to enter a virtual excited state, and then return to a

ground state either higher or lower than the original through the emission of another photon, as seen on the right side of Figure 2.5. Raman Stokes scattering occurs when the scattered photon has less energy than the incident photon, while Raman Anti-Stokes scattering occurs when the scattered photon has more energy than the incident photon. In contrast to fluorescence, which involves transitions between electronic energy levels, Raman scattering exploits smaller transitions between vibrational energy levels. This less intense signal requires a powerful laser source and a sensitive detector, and the much stronger fluorescence must be subtracted from the raw spectrum as well.

A Raman spectrum is a plot of scattered light intensity versus the frequency shift of the scattered photon, making it independent of excitation wavelength. The frequency shift is expressed in units of wavenumber (usually cm^{-1}), which is the reciprocal of the wavelength. The spectrum consists of a series of peaks, each of which represents a different vibrational mode of the scattering molecule. These peaks are narrow and highly specific to a particular chemical bond, so each molecule has a unique spectrum, or "fingerprint," associated with it from about 400 to 1800 cm^{-1}. Many biological molecules have distinguishable spectra, so one can determine the gross biochemical composition of a tissue from its Raman spectrum. One particularly relevant biochemical change for cancer cells is an increase in the nucleic acid content concomitant with increased proliferation and genetic instability. This change, among others, can be detected with Raman spectroscopy [17, 18].

Raman spectroscopy was historically used in analytical chemistry to determine chemical structures or the presence of certain molecules, and it has only been in the last ten to twelve years that it has become a more popular choice for studying tissue. The majority of early studies were *in vitro*, attempting to distinguish normal from cancerous tissue in areas like cervix [19], bladder

15

and prostate [20], lung [21], and the GI tract [22]. More recent studies have brought Raman to *in vivo* applications [23, 24], where it has been successfully applied to the cervix [25] and GI tract [22, 26], among other uses.

2.6 Optical Spectroscopy of Breast Tissue

There have been numerous studies using fluorescence, reflectance, or Raman spectroscopy to classify breast tissues. Most of these studies, which use widely different experimental setups, focus on purely diagnostic applications.

2.6.1 Fluorescence for Breast Tissue

Several studies have found significant differences in both emission and excitation spectra from normal, benign, and/or malignant breast tissues. Alfano et al. first demonstrated differences between normal and malignant breast tissues in their fluorescence emission spectra at various excitation wavelengths, and in their excitation spectra measured at various emission wavelengths [27, 28]. Yang et al. used 300 nm-excited emission spectra and excitation spectra at 340 nm emission to discriminate between malignant and fibrous samples with 93% sensitivity and 95% specificity, but results were worse for discriminating normal fatty and malignant tissues [29-31]. Gupta and Majumder et al. measured emission spectra at 337 and 488 nm excitation wavelengths from normal, benign (fibroadenoma), and malignant (IDC) breast tissue samples, and using the integrated emission intensity from the 337 nm excitation, malignant tissues were separated in a binary fashion from both benign and normal with 98% sensitivity and specificity [32, 33]. The samples used in this study, though, were very homogeneous and not entirely indicative of clinically relevant situations. More recently, Ramanujam et al. used the fluorescence emission

spectra from multiple excitation wavelengths ranging from 300 to 460 nm to separate malignant from normal or benign tissues with 70% sensitivity and 92% specificity [34]. Using a probe with three different delivery to collection fiber distances, the same group found that analyzing integrated fluorescence emission intensities from a single excitation wavelength at all three separations could provide results comparable to the previous study, but with a simpler setup [35]. This group has subsequently achieved somewhat better results (87% sensitivity and 89% specificity) with a model-based approach to extract intrinsic fluorescence spectra [36, 37]. Another recent report by Volynskaya et al. used a similar extraction scheme to achieve 91% overall classification accuracy [38].

2.6.2 Reflectance for Breast Tissue

A few groups have investigated the utility of UV-Visible diffuse reflectance (or elastic scattering) spectroscopy, either alone or in conjunction with fluorescence, for breast cancer diagnosis. Several studies have determined that diffuse reflectance spectroscopy can detect changes in scattering and absorption due to malignancy-associated alterations in levels and organization of DNA, β-carotene, hemoglobin, and other proteins [29, 34-42]. Of these, Bigio et al. used *in vivo* measurements to distinguish malignant from normal tissue with sensitivities up to 69% and specificities up to 93% [41].

2.6.3 Raman for Breast Tissue

Alfano et. al. were the first to examine the ability of Raman spectroscopy to distinguish normal from malignant breast tissue [43-46]. Later, Redd et al. demonstrated the advantages of NIR excitation, particularly in the context of breast cancer. Although no rigorous algorithm was

attempted, they saw results similar to those of Alfano – namely a decrease in lipid contributions to spectra from IDC samples, as well as an increase in the collagen contributions in benign and malignant samples [47]. Feld et al. have done extensive work on using Raman spectroscopy for breast cancer diagnosis. An early study similar to Redd's showed comparable spectra, but multivariate statistical algorithms improved diagnosis [48]. Over the past several years, Feld's group has developed a system that classifies (*in vitro* only) breast Raman spectra according to the modeled contributions of individual component spectra from materials like fat, collagen, and DNA [49-52] to discriminate malignant from normal and benign tissues with 94% sensitivity and 96% specificity [53]. Martin et al. have used Fourier transform (FT)-Raman to look at qualitative, but not quantitative differences among seven different types of normal or diseased breast tissues [54]. This group has also used FT-Raman in a preliminary attempt to differentiate normal, tumor, and tumor boundary tissues in breast tissue samples, again with limited quantitative analysis [55]. Chowdary et al. used PCA to classify Raman spectra as normal, benign, or malignant with a moderate success rate of 75% [56], and Kast et al. showed that Raman could differentiate normal, tumor, and tumor bed tissue in a rat model [57].

Most of the above work is focused on diagnosis and has not been implemented for guidance of therapy. Two reports were found with references to utilizing optical methods for guidance of therapy. Bigio et al. used *in vivo* measurements in an attempt both to make a diagnosis and help guide resection, and as mentioned above, they achieved good specificities but only fair sensitivities [41]. Additionally, Feld et al. conducted a small pilot *in vivo* trial for guiding resection with Raman spectroscopy in which normal, fibrocystic change, and malignant tissues were classified with an overall accuracy rate of 93% [58]. However, neither report considered the need for determining negative margins to a depth of 1-2 mm below the surface of

the excised specimen, portending to a need for sub-surface detection. Additionally, these reports focused on using a point-like fiber optic probe to examine tissue *in vivo* prior to resection, rather than interrogating the resected specimen, as is the current standard of care for surgical pathology.

2.7 Spectral Imaging

An aspect that has not been addressed in previous work in the area of optical spectroscopy for therapeutic guidance is the impracticality of a method that probes a small area (~1 x 1 mm) each time on a sample that is typically a few centimeters in diameter in each of three dimensions. Fluorescence and diffuse reflectance-based spectral imaging, in which fluorescence and reflectance spectra are recorded for each pixel of a two dimensional image, is a more viable method for a surgical guidance tool. This kind of system typically includes excitation sources for fluorescence and reflectance, a collection lens, a tunable filter such as an acousto-optic tunable filter (AOTF) or liquid crystal tunable filter (LCTF), and a charge-coupled device (CCD) camera to record the image at each wavelength selected by the filter. Using such a system, a surgeon could identify the spatial extent of a tumor or positive margin rather than simply knowing whether a given point is normal or cancerous. Our lab has previously achieved a 95% classification rate for discriminating normal from tumor core and infiltrating margin tissues in brain tissues using point spectroscopy [59], and subsequently developed a spectral imaging system for use in guiding brain tumor resection that can obtain spectra at each 26 by 26 μm pixel in a one inch diameter field of view [60]. While breast and brain tissues have different compositions, the primary biological fluorophores mentioned above would still be present in both tissue types.

2.8 Depth-Sensitive Techniques

Additional aspects of spectral measurements relevant to this work are the ability to take measurements with a degree of depth sensitivity, and to interrogate tissue to a deeper extent than is possible with standard configurations. The penetration depth of optical methods depends on the wavelength of the source used to excite the optical signals. Fluorescence and diffuse reflectance spectra are typically collected from a volume that is about 100-500 μm in depth, while traditional Raman probes can typically probe closer to 1 millimeter in depth. Since BCT requires that the excised tissue have clear margins of at least 1 mm from the tumor, for practical utility, any method developed should be capable of probing tissue up to this depth. Several fiber optic probe designs have been developed over the years to obtain spectra from more superficial versus deeper layers of tissue [61], but these are generally limited to no more than the first 1 mm in depth of epithelial tissues. Using a Kerr gate, which can open and close on a picosecond scale, one can selectively gate signals from different layers of tissue [62-64], but the instrumentation is too expensive and large to be clinically viable. Other methods that are more applicable for this work are using polarization optics in the excitation and detection legs, particularly for fluorescence and reflectance, and using a spatial offset between delivery and collection fibers.

2.8.1 Fluorescence Polarization

One possible method to acquire spectral information at varying depths is by changing the relative angle between polarizers placed in the excitation and detection legs, based on work by Majumder and Ghosh et al. [65]. Fluorescence emission largely maintains the polarization of excitation photons, but multiple scattering degrades polarization [66]. Thus, measurements made with excitation and collection legs co-polarized will emphasize signatures from superficial

components, while cross-polarized measurements will be more sensitive to fluorescence photons originating from deeper tissue layers that are more likely to have undergone multiple scattering. Polarized fluorescence and reflectance (non-spectral) imaging has been used for demarcating skin cancers during Mohs micrographic surgeries [67, 68], although in this case they are more interested in superficial than deeper layers, which is the opposite aim of margin evaluation.

2.8.2 Spatially Offset Raman Spectroscopy (SORS)

As demonstrated in Figure 2.6, introducing a spatial offset between source and detection elements allows for depth selectivity in spectral measurements. Larger separations are more likely to detect photons that have traveled deeper into tissue and have been multiply scattered to a greater radial distance compared with photons that have only undergone minimal scattering events and have stayed in the superficial layers. Matousek first demonstrated this effect with Raman spectroscopy of diffusely scattering media using a two-layer phantom in which each layer had a chemical with a distinctive spectrum, and the measured spectra became more similar
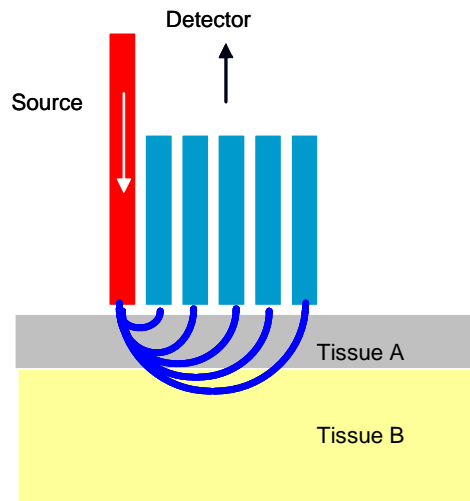
Figure 2.6 Visualization of source - detector separation for depth selectivity in spatially offset Raman spectroscopyo (SORS). Blue "banana curves" represent mean photon paths.

to the bottom layer with increased separation [69]. The same group demonstrated the first biological application of this technique in detecting the strong, unique Raman signature of bone through several millimeters of soft tissue [70]. A 6 mm diameter fiber optic probe with varying distances between source and detector fibers was used by Morris et al. to detect and map different polymers under a layer of another polymer [71]. Further work by this group has been aimed at determining optimal probe designs for colleting SORS spectra from bone transcutaneously [72-74]. In another application, Matousek and Stone et al. used a fiber optic probe with a central excitation fiber and an annulus of collection fibers to detect the Raman spectral features of hydroxyapatite, a mineral commonly present in breast cancer calcifications, through varying thicknesses of overlying lean chicken breast tissue [75].

Detecting breast tumors under normal breast tissue is a more challenging application than the above ones. Hard tissues like bone and calcifications have strong Raman bands that are not present in soft tissue, but Raman spectra from normal breast tissue and breast tumors differ in more subtle ways, such as widths of peaks and relative ratios of peaks. Even so, it is hypothesized that the SORS technique could provide sufficient contrast to enable margin evaluation up to the clinically relevant 1-2 mm in depth in excised partial mastectomy specimens.

2.9 Significance and Impact

The development of a method to improve the intraoperative evaluation of surgical margin status during breast cancer resection would have a sizeable impact on the health care system. Of the roughly 180,000 patients eligible for breast conserving therapy each year in the US, about three-fourths of them, or 135,000, will choose BCT. According to one study, 25% of patients

undergoing BCT require a second surgery because the complete tumor was not removed with a 1-2 mm clear margin [6]. At $6,000 to $10,000 of hospital charges for a typical breast tissue resection, the inability to ensure complete removal of breast tumors with clear margins is costing patients and the health care industry hundreds of millions of dollars per year. Besides the direct costs, patients may suffer from a great deal of anxiety as they wait up to a week or more to get definitive results from pathology regarding the completeness of the resection. This work will also serve as an important base for researchers considering this problem or similar ones that require looking at a large area of tissue in a depth-sensitive manner, as it is a mostly unexplored domain in the relatively young field of biomedical optical spectroscopy.

2.10 References

1.   K. I. Bland, and E. M. C. III, eds. *The Breast: Comprehensive Management of Benign and Malignant Disorders* (Saunders, St. Louis, 2004).

2.   American Cancer Society, "Cancer Facts and Figures 2009," (American Cancer Society, Atlanta, 2009).

3.   J. R. Harris, M. E. Lippman, M. Morrow, and C. K. Osborne, eds. *Diseases of the Breast* (Lippincott, Williams, and Wilkins, 2000).

4.   E. B. C. T. C. Group, "Effects of radiotherapy and surgery in early breast cancer. An overview of the randomized trials.," N Engl J Med **333**, 1444-1455 (1995).

5.   K. C. Horst, M. C. Smitt, D. R. Goffinet, and R. W. Carlson, "Predictors of local recurrence after breast-conservation therapy," Clin Breast Cancer **5**, 425-438 (2005).

6.   G. C. Balch, S. K. Mithani, J. F. Simpson, and M. C. Kelley, "Accuracy of intraoperative gross examination of surgical margin status in women undergoing partial mastectomy for breast malignancy," Am Surg **71**, 22-27; discussion 27-28 (2005).

7.   N. Cabioglu, K. K. Hunt, A. A. Sahin, H. M. Kuerer, G. V. Babiera, S. E. Singletary, G. J. Whitman, M. I. Ross, F. C. Ames, B. W. Feig, T. A. Buchholz, and F. Meric-Bernstam, "Role for intraoperative margin assessment in patients undergoing breast-conserving surgery," Ann Surg Oncol **14**, 1458-1471 (2007).

8.   V. S. Klimberg, S. Harms, and S. Korourian, "Assessing margin status," Surg Oncol **8**, 77-84 (1999).

9.   M. F. Mitchell, S. B. Cantor, N. Ramanujam, G. Tortolero-Luna, and R. Richards-Kortum, "Fluorescence spectroscopy for diagnosis of squamous intraepithelial lesions of the cervix," Obstet Gynecol **93**, 462-470 (1999).

10.   N. Ramanujam, "Fluorescence spectroscopy of neoplastic and non-neoplastic tissues," Neoplasia **2**, 89-117 (2000).

11.   N. Ramanujam, M. F. Mitchell, A. Mahadevan, S. Thomsen, A. Malpica, T. Wright, N. Atkinson, and R. Richards-Kortum, "Spectroscopic diagnosis of cervical intraepithelial neoplasia (CIN) in vivo using laser-induced fluorescence spectra at multiple excitation wavelengths," Lasers Surg Med **19**, 63-74 (1996).

12.   L. Brancaleon, A. J. Durkin, J. H. Tu, G. Menaker, J. D. Fallon, and N. Kollias, "In vivo fluorescence spectroscopy of nonmelanoma skin cancer," Photochem Photobiol **73**, 178-183 (2001).

13.   R. Gillies, G. Zonios, R. R. Anderson, and N. Kollias, "Fluorescence excitation spectroscopy provides information about human skin in vivo," J Invest Dermatol **115**, 704-707 (2000).

14.   W. C. Lin, S. A. Toms, M. Johnson, E. D. Jansen, and A. Mahadevan-Jansen, "In vivo brain tumor demarcation using optical spectroscopy," Photochem Photobiol **73**, 396-402 (2001).

15.   W. C. Lin, S. A. Toms, M. Motamedi, E. D. Jansen, and A. Mahadevan-Jansen, "Brain tumor demarcation using optical spectroscopy; an in vitro study," J Biomed Opt **5**, 214-220 (2000).

16.   N. Ramanujam, M. F. Mitchell, A. Mahadevan, S. Thomsen, A. Malpica, T. Wright, N. Atkinson, and R. Richards-Kortum, "Development of a multivariate statistical algorithm to analyze human cervical tissue fluorescence spectra acquired in vivo," Lasers Surg Med **19**, 46-62 (1996).

17.   A. Mahadevan-Jansen, "Raman Spectroscopy: From Benchtop to Bedside," in *Biomedical Photonics Handbook*, T. Vo-Dinh, ed. (CRC Press, Washington DC, 2003), pp. 30:31-30:27.

18.   A. Mahadevan-Jansen, and R. Richards-Kortum, "Raman Spectroscopy for the Detection of Cancers and Precancers," J Biomed Optics **1**, 31-70 (1996).

19.   A. Mahadevan-Jansen, M. F. Mitchell, N. Ramanujam, A. Malpica, S. Thomsen, U. Utzinger, and R. Richards-Kortum, "Near-infrared Raman spectroscopy for in vitro detection of cervical precancers," Photochem Photobiol **68**, 123-132 (1998).

20.   P. Crow, A. Molckovsky, N. Stone, J. Uff, B. Wilson, and L. M. WongKeeSong, "Assessment of fiberoptic near-infrared raman spectroscopy for diagnosis of bladder and prostate cancer," Urology **65**, 1126-1130 (2005).

21.   Z. Huang, A. McWilliams, H. Lui, D. I. McLean, S. Lam, and H. Zeng, "Near-infrared Raman spectroscopy for optical diagnosis of lung cancer," Int J Cancer **107**, 1047-1052 (2003).

22.   A. Molckovsky, L. M. Song, M. G. Shim, N. E. Marcon, and B. C. Wilson, "Diagnostic potential of near-infrared Raman spectroscopy in the colon: differentiating adenomatous from hyperplastic polyps," Gastrointest Endosc **57**, 396-402 (2003).

23.   L. P. Choo-Smith, H. G. Edwards, H. P. Endtz, J. M. Kros, F. Heule, H. Barr, J. S. Robinson, Jr., H. A. Bruining, and G. J. Puppels, "Medical applications of Raman spectroscopy: from proof of principle to clinical implementation," Biopolymers **67**, 1-9 (2002).

24.   E. B. Hanlon, R. Manoharan, T. W. Koo, K. E. Shafer, J. T. Motz, M. Fitzmaurice, J. R. Kramer, I. Itzkan, R. R. Dasari, and M. S. Feld, "Prospects for in vivo Raman spectroscopy," Phys Med Biol **45**, R1-59 (2000).

25.   A. Mahadevan-Jansen, M. F. Mitchell, N. Ramanujam, U. Utzinger, and R. Richards-Kortum, "Development of a fiber optic probe to measure NIR Raman spectra of cervical tissue in vivo," Photochem Photobiol **68**, 427-431 (1998).

26.   M. G. Shim, L. M. Song, N. E. Marcon, and B. C. Wilson, "In vivo near-infrared Raman spectroscopy: demonstration of feasibility during clinical gastrointestinal endoscopy," Photochem Photobiol **72**, 146-150 (2000).

27.   R. R. Alfano, G. C. Tang, A. Pradhan, W. Lam, D. S. J. Choy, and E. Opher, "Fluorescence-Spectra from Cancerous and Normal Human-Breast and Lung Tissues," Ieee Journal of Quantum Electronics **23**, 1806-1811 (1987).

28.   R. R. Alfano, A. Pradhan, G. C. Tang, and S. J. Wahl, "Optical Spectroscopic Diagnosis of Cancer and Normal Breast Tissues," J. Opt. Soc. Amer. B (Opt Phys) **6**, 1015-1023 (1989).

29.   Y. Yang, A. Katz, E. J. Celmer, M. Zurawska-Szczepaniak, and R. R. Alfano, "Optical spectroscopy of benign and malignant breast tissues," Lasers Life Sci **7**, 115-127 (1996).

30.   Y. Yang, A. Katz, E. J. Celmer, M. Zurawska-Szczepaniak, and R. R. Alfano, "Fundamental differences of excitation spectrum between malignant and benign breast tissues," Photochem Photobiol **66**, 518-522 (1997).

31.   Y. Yang, E. J. Celmer, M. Zurawska-Szczepaniak, and R. R. Alfano, "Excitation spectrum of malignant and benign breast tissues: a potential optical biopsy approach," Lasers Life Sci **7**, 249-265 (1997).

32.   P. K. Gupta, S. K. Majumder, and A. Uppal, "Breast cancer diagnosis using N2 laser excited autofluorescence spectroscopy," Lasers Surg Med **21**, 417-422 (1997).

33.   S. K. Majumder, P. K. Gupta, B. Jain, and A. Uppal, "UV excited autofluorescence spectroscopy of human breast tissues for discriminating cancerous tissue from benign tumor and normal tissue," Lasers Life Sci **8**, 249-264 (1998).

34.   G. M. Palmer, C. Zhu, T. M. Breslin, F. Xu, K. W. Gilchrist, and N. Ramanujam, "Comparison of multiexcitation fluorescence and diffuse reflectance spectroscopy for the diagnosis of breast cancer (March 2003)," IEEE Trans Biomed Eng **50**, 1233-1242 (2003).

35.   C. Zhu, G. M. Palmer, T. M. Breslin, F. Xu, and N. Ramanujam, "Use of a multiseparation fiber optic probe for the optical diagnosis of breast cancer," J Biomed Opt **10**, 024032 (2005).

36.   C. Zhu, G. M. Palmer, T. M. Breslin, J. Harter, and N. Ramanujam, "Diagnosis of breast cancer using fluorescence and diffuse reflectance spectroscopy: a Monte-Carlo-model-based approach," J Biomed Opt **13**, 034015 (2008).

37.   C. Zhu, T. M. Breslin, J. Harter, and N. Ramanujam, "Model based and empirical spectral analysis for the diagnosis of breast cancer," Optics express **16**, 14961-14978 (2008).

38.   Z. Volynskaya, A. S. Haka, K. L. Bechtel, M. Fitzmaurice, R. Shenk, N. Wang, J. Nazemi, R. R. Dasari, and M. S. Feld, "Diagnosing breast cancer using diffuse reflectance spectroscopy and intrinsic fluorescence spectroscopy," Journal of Biomedical Optics **13**, 024012-024019 (2008).

39.   Y. Yang, E. J. Celmer, J. A. Koutcher, and R. R. Alfano, "UV reflectance spectroscopy probes DNA and protein changes in human breast tissues," J Clin Laser Med Surg **19**, 35-39 (2001).

40.   Y. Yang, E. J. Celmer, J. A. Koutcher, and R. R. Alfano, "DNA and protein changes caused by disease in human breast tissues probed by the Kubelka-Munk spectral functional," Photochem Photobiol **75**, 627-632 (2002).

41.   I. J. Bigio, S. G. Bown, G. Briggs, C. Kelley, S. Lakhani, D. Pickard, P. M. Ripley, I. G. Rose, and C. Saunders, "Diagnosis of breast cancer using elastic-scattering spectroscopy: preliminary clinical results," J Biomed Opt **5**, 221-228 (2000).

42.   N. Ghosh, S. K. Mohanty, S. K. Majumder, and P. K. Gupta, "Measurement of optical transport properties of normal and malignant human breast tissue," Applied Optics **40**, 176-184 (2001).

43.   R. R. Alfano, A. Pradhan, G. C. Tang, and S. J. Wahl, "Optical spectroscopic diagnosis of cancer and normal breast tissues," J. Opt. Soc. Am. B **6**, 1015-1023 (1989).

44.   R. R. Alfano, C. H. Liu, W. L. Sha, H. R. Zhu, D. L. Akins, J. Cleary, R. Prudente, and E. Celmer, "Human breast tissue studied by IR Fourier transform Raman spectroscopy," Laser Life Sci **4**, 23-28 (1991).

45.   G. C. Tang, A. Pradhan, and R. R. Alfano, "Spectroscopic differences between human cancer and normal lung and breast tissues," Lasers Surg Med **9**, 290-295 (1989).

46.   C. H. Liu, B. B. Das, W. L. S. Glassman, G. C. Tang, K. M. Yoo, H. R. Zhu, D. L. Akins, S. S. Lubicz, J. Cleary, R. Prudente, E. Celmer, A. Caron, and R. R. Alfano, "Raman, Fluorescence, and Time-Resolved Light-Scattering as Optical Diagnostic-Techniques to Separate Diseased and Normal Biomedical Media," Journal of Photochemistry and Photobiology B-Biology **16**, 187-209 (1992).

47.   C. J. Frank, R. L. McCreery, and D. C. Redd, "Raman spectroscopy of normal and diseased human breast tissues," Anal Chem **67**, 777-783 (1995).

48.   R. Manoharan, K. Shafer, L. Perelman, J. Wu, K. Chen, G. Deinum, M. Fitzmaurice, J. Myles, J. Crowe, R. R. Dasari, and M. S. Feld, "Raman spectroscopy and fluorescence photon migration for breast cancer diagnosis and imaging," Photochem Photobiol **67**, 15-22 (1998).

49.   A. S. Haka, K. E. Shafer-Peltier, M. Fitzmaurice, J. Crowe, R. R. Dasari, and M. S. Feld, "Identifying microcalcifications in benign and malignant breast lesions by probing differences in their chemical composition using Raman spectroscopy," Cancer Res **62**, 5375-5380 (2002).

50.   K. E. Shafer-Peltier, A. S. Haka, M. Fitzmaurice, J. Crowe, J. Myles, R. R. Dasari, and M. S. Feld, "Raman microspectroscopic model of human breast tissue: implications for breast cancer diagnosis in vivo," Journal of Raman Spectroscopy **33**, 552-563 (2002).

51.   K. E. Shafer-Peltier, A. S. Haka, J. T. Motz, M. Fitzmaurice, R. R. Dasari, and M. S. Feld, "Model-based biological Raman spectral imaging," J Cell Biochem Suppl **39**, 125-137 (2002).

52.   J. T. Motz, S. J. Gandhi, O. R. Scepanovic, A. S. Haka, J. R. Kramer, R. R. Dasari, and M. S. Feld, "Real-time Raman system for in vivo disease diagnosis," J Biomed Opt **10**, 031113 (2005).

53.   A. S. Haka, K. E. Shafer-Peltier, M. Fitzmaurice, J. Crowe, R. R. Dasari, and M. S. Feld, "Diagnosing breast cancer by using Raman spectroscopy," Proc Natl Acad Sci U S A **102**, 12371-12376 (2005).

54.   R. A. Bitar, S. Martinho Hda, C. J. Tierra-Criollo, L. N. Zambelli Ramalho, M. M. Netto, and A. A. Martin, "Biochemical analysis of human breast tissues using Fourier-transform Raman spectroscopy," J Biomed Opt **11**, 054001 (2006).

55.   A. C. de Miranda Marzullo, O. P. Neto, R. A. Bitar, H. da Silva Martinho, and A. A. Martin, "FT-raman spectra of the border of infiltrating ductal carcinoma lesions," Photomed Laser Surg **25**, 455-460 (2007).

56.   M. V. Chowdary, K. K. Kumar, J. Kurien, S. Mathew, and C. M. Krishna, "Discrimination of normal, benign, and malignant breast tissues by Raman spectroscopy," Biopolymers **83**, 556-569 (2006).

57.   R. E. Kast, G. K. Serhatkulu, A. Cao, A. K. Pandya, H. Dai, J. S. Thakur, V. M. Naik, R. Naik, M. D. Klein, G. W. Auner, and R. Rabah, "Raman spectroscopy can differentiate malignant tumors from normal breast tissue and detect early neoplastic changes in a mouse model," Biopolymers **89**, 235-241 (2008).

58.   A. S. Haka, Z. Volynskaya, J. A. Gardecki, J. Nazemi, J. Lyons, D. Hicks, M. Fitzmaurice, R. R. Dasari, J. P. Crowe, and M. S. Feld, "In vivo margin assessment during partial mastectomy breast surgery using raman spectroscopy," Cancer Res **66**, 3317-3322 (2006).

59.   S. K. Majumder, S. Gebhart, M. D. Johnson, R. Thompson, W. C. Lin, and A. Mahadevan-Jansen, "A probability-based spectroscopic diagnostic algorithm for simultaneous discrimination of brain tumor and tumor margins from normal brain tissue," Appl Spectrosc **61**, 548-557 (2007).

60.   S. C. Gebhart, R. C. Thompson, and A. Mahadevan-Jansen, "Liquid-crystal tunable filter spectral imaging for brain tumor demarcation," Appl Opt **46**, 1896-1910 (2007).

61.   U. Utzinger, and R. R. Richards-Kortum, "Fiber optic probes for biomedical optical spectroscopy," J Biomed Opt **8**, 121-147 (2003).

62.   R. Baker, P. Matousek, K. L. Ronayne, A. W. Parker, K. Rogers, and N. Stone, "Depth profiling of calcifications in breast tissue using picosecond Kerr-gated Raman spectroscopy," Analyst **132**, 48-53 (2007).

63.   M. C. Prieto, P. Matousek, M. Towrie, A. W. Parker, M. Wright, A. W. Ritchie, and N. Stone, "Use of picosecond Kerr-gated Raman spectroscopy to suppress signals from both surface and deep layers in bladder and prostate tissue," J Biomed Opt **10**, 44006 (2005).

64.   P. Matousek, N. Everall, M. Towrie, and A. W. Parker, "Depth profiling in diffusely scattering media using Raman spectroscopy and picosecond Kerr gating," Appl Spectrosc **59**, 200-205 (2005).

65.   N. Ghosh, S. K. Majumder, H. S. Patel, and P. K. Gupta, "Depth-resolved fluorescence measurement in a layered turbid medium by polarized fluorescence spectroscopy," Opt Lett **30**, 162-164 (2005).

66.   N. Ghosh, S. K. Majumder, and P. K. Gupta, "Fluorescence depolarization in a scattering medium: Effect of size parameter of a scatterer," Physical Review E **65**, 026608 (2002).

67.   A. N. Yaroslavsky, E. V. Salomatina, V. Neel, R. Anderson, and T. Flotte, "Fluorescence polarization of tetracycline derivatives as a technique for mapping nonmelanoma skin cancers," J Biomed Opt **12**, 014005 (2007).

68.   A. N. Yaroslavsky, V. Neel, and R. R. Anderson, "Fluorescence polarization imaging for delineating nonmelanoma skin cancers," Opt Lett **29**, 2010-2012 (2004).

69.   P. Matousek, I. P. Clark, E. R. Draper, M. D. Morris, A. E. Goodship, N. Everall, M. Towrie, W. F. Finney, and A. W. Parker, "Subsurface probing in diffusely scattering media using spatially offset Raman spectroscopy," Appl Spectrosc **59**, 393-400 (2005).

70.   P. Matousek, E. R. Draper, A. E. Goodship, I. P. Clark, K. L. Ronayne, and A. W. Parker, "Noninvasive Raman spectroscopy of human tissue in vivo," Appl Spectrosc **60**, 758-763 (2006).

71.   M. V. Schulmerich, W. F. Finney, R. A. Fredricks, and M. D. Morris, "Subsurface Raman spectroscopy and mapping using a globally illuminated non-confocal fiber-optic array probe in the presence of Raman photon migration," Appl Spectrosc **60**, 109-114 (2006).

72.   M. V. Schulmerich, J. H. Cole, J. M. Kreider, F. Esmonde-White, K. A. Dooley, S. A. Goldstein, and M. D. Morris, "Transcutaneous Raman Spectroscopy of Murine Bone In Vivo," Appl. Spectrosc. **63**, 286-295 (2009).

73.   M. V. Schulmerich, K. A. Dooley, T. M. Vanasse, S. A. Goldstein, and M. D. Morris, "Subsurface and transcutaneous Raman spectroscopy and mapping using concentric illumination rings and collection with a circular fiber-optic array," Appl Spectrosc **61**, 671-678 (2007).

74.   M. V. Schulmerich, K. A. Dooley, M. D. Morris, T. M. Vanasse, and S. A. Goldstein, "Transcutaneous fiber optic Raman spectroscopy of bone using annular illumination and a circular array of collection fibers," J Biomed Opt **11**, 060502 (2006).

75.   N. Stone, R. Baker, K. Rogers, A. W. Parker, and P. Matousek, "Subsurface probing of calcifications with spatially offset Raman spectroscopy (SORS): future possibilities for the diagnosis of breast cancer," Analyst **132**, 899-905 (2007).

CHAPTER III

PRELIMINARY STUDIES

3.1 Introduction

Although the studies described in the background section use autofluorescence, diffuse reflectance, combined autofluorescence and reflectance, or Raman spectroscopy for breast tissue discrimination, there is no published report of a direct, side-by-side comparison of the efficacy of these modalities for specific types of discrimination. The goal of this preliminary study, completed in a joint effort with Dr. Shovan Majumder, was to carry out a comparative evaluation of the relative capabilities of fluorescence, diffuse reflectance, combined fluorescence and reflectance, and Raman spectroscopy for discriminating the different histopathological categories of human breast tissues. Fluorescence, reflectance, and Raman spectra were acquired *in vitro* from human breast tissue samples belonging to four histopathological categories: invasive ductal carcinoma (IDC), ductal carcinoma *in-situ* (DCIS), fibroadenoma (FA), and normal. A probability-based multivariate statistical algorithm capable of direct multi-class classification was developed to analyze the diagnostic content of these different sets of optical spectra measured from the same set of breast tissue sites.

3.2 Materials and Methods

3.2.1 Breast tissue samples

The human breast tissue samples were obtained under a protocol approved by the Vanderbilt University Institutional Review Board (IRB #050551). The samples were obtained

fresh-frozen from the Vanderbilt Tissue Repository or from the National Cancer Institute's Cooperative Human Tissue Network (CHTN). In all, 74 tissue samples from different patients were obtained for this study. Normal samples were obtained from either reduction mammoplasty or uninvolved areas from mastectomy specimens, and tumor samples were partial sections of surgically removed breast lesions. All samples were stored at -80 ^{o}C until spectroscopic study, at which point they were thawed to room temperature in phosphate-buffered saline.

3.2.2 Instrumentation

In vitro fluorescence and diffuse reflectance spectra of breast tissue samples were measured using a portable spectroscopic system as illustrated in Figure 3.1. A high-pressure nitrogen laser (Spectra Physics, Mountain View, CA) at 337 nm was used as the excitation
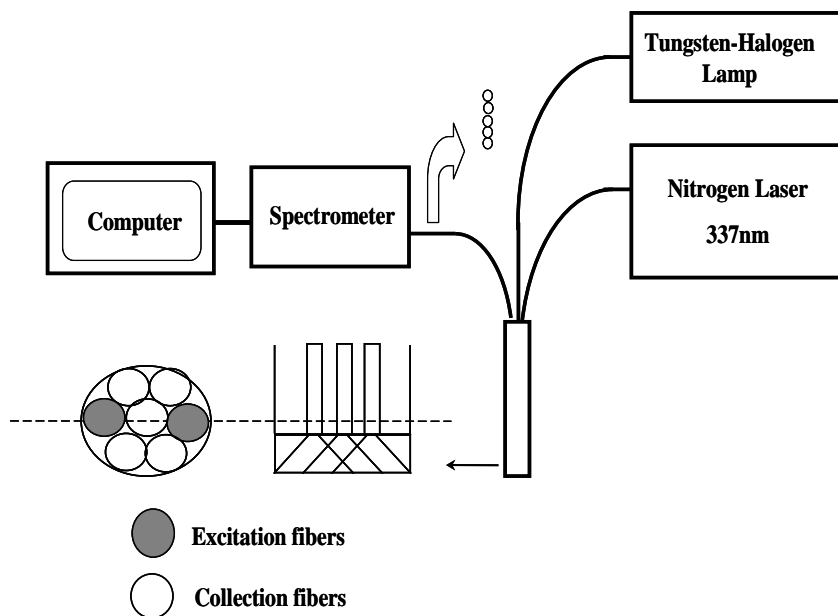
Figure 3.1 Schematic of the combined fluorescence and reflectance spectroscopy system used in the study.

source for fluorescence measurements, and a 150-Watt tungsten-halogen lamp (Ocean Optics, Dunedin, FL) emitting broadband white light from 400 nm to 850 nm was used for diffuse

reflectance measurements. Light delivery to and collection from the sample was achieved with a fiber-optic probe consisting of seven 300 μm core diameter fibers arranged in a six-around-one configuration (Romack, Williamsburg, VA). Two of the surrounding fibers delivered laser and white light consecutively to the tissue sample while the remaining fibers collected fluorescence and diffuse reflectance from the tissue sample. Diffuse reflectance and fluorescence emissions collected by the fiber-optic probe were serially dispersed and detected with a chip-based spectrometer (model number S-2000, Ocean Optics, Dunedin, FL). For this study, the output power of the white light was ~0.6 mW at the tissue surface, and the nitrogen laser was operated at a 20-Hz repetition rate, 5-nanosecond pulse width, and average pulse energy of 45±5 μJ at the tissue surface. An integration time of 100 ms was used for each spectral measurement.

Raman spectra of the breast tissue samples were measured with a portable Raman spectroscopy system shown in Figure 3.2. The system consists of a 785 nm diode laser (Process Instruments, Inc., Salt Lake City, UT), a seven-around-one beam-steered fiber optic probe
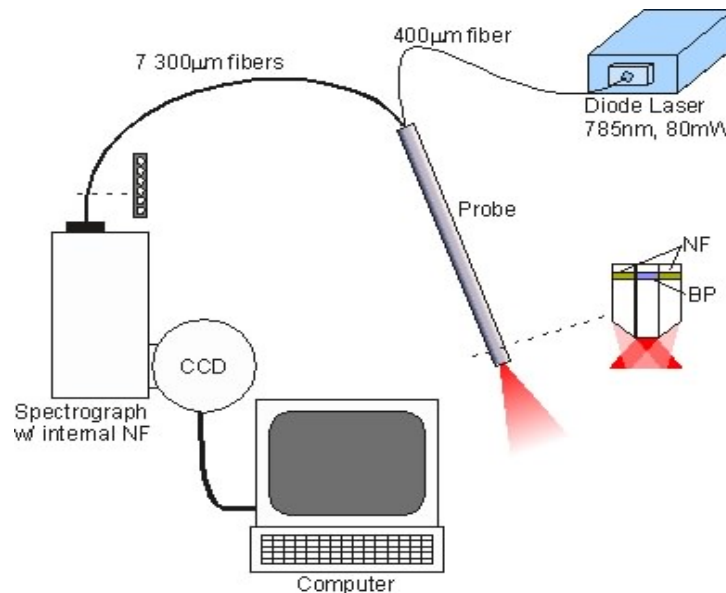
Figure 3.2 Schematic of Raman system used for study.

(Visionex Inc., Atlanta, GA), an imaging spectrograph (Kaiser Optical Systems, Inc., Ann Arbor, MI), and a back-illuminated, deep-depletion, thermoelectrically cooled CCD (Princeton Instruments, Princeton, NJ), all controlled with a laptop computer. The beam-steered fiber optic probe delivered the 785 nm light, band-pass-filtered at the probe tip, onto the tissue. It then collected the Raman scattered light, which was filtered with an inline notch filter within the probe itself. The light was then fed into the spectrograph, where it was filtered again with a 785 nm holographic notch filter and dispersed onto the CCD. For this study, the fiber optic probe delivered 80mW onto the tissue and collected the scattered light for 1-3 seconds.

3.2.3 Experimental methods

A standard protocol was followed for the spectral measurements and maintained for all the samples in this study. Prior to spectral acquisition, each sample was thawed to room temperature in phosphate-buffered saline. For recording spectra, the tips of the fiber-optic probes were placed normally in gentle contact with the target tissue. From each tissue sample, spectra were recorded from 2-6 sites depending on the size of the sample. From each individual site, autofluorescence, diffuse reflectance, and Raman spectra were measured sequentially. In all cases, the overhead fluorescent lights were turned off during the measurements. Following spectral acquisition from each sample, the investigated sites were inked to record their locations, and then fixed in formalin for standard hematoxylin and eosin staining and examination by an experienced pathologist blinded to the results of the optical spectra. The histopathology report of each site was considered to be the gold standard. All spectra were categorized according to their histological identities and grouped into IDC, DCIS, FA, or normal breast tissue.

3.2.4 Data processing

After acquisition of autofluorescence and diffuse reflectance spectra, a set of reference spectra from a fluorescence and a reflectance standard were recorded to correct for inter-sample variability due to variations in laser-pulse energy and white light power. The fluorescence standard was a low-concentration Rhodamine 6G solution (2mg/L) contained in a quartz cuvette, and the reflectance standard was a 20% reflectance plate (Labsphere, North Sutton, NH) placed in a black box. All *in vitro* raw fluorescence and diffuse reflectance spectra were processed to remove instrumentation-induced variations and to yield calibrated spectra. The resultant fluorescence and diffuse reflectance spectra were further corrected for the non-uniform spectral response of the detection system. Fluorescence emission spectra were recorded from 370-650 nm, and diffuse reflectance spectra were recorded from 400-800 nm.

Prior to Raman spectral measurements, the wavenumber axis was calibrated with a neon-argon lamp, acetaminophen, and naphthalene standards. For each Raman spectrum measured, the signal from the CCD was binned along the vertical axis to create a single spectrum per measurement site. Prior to any signal processing, the spectrum was truncated to only include the region from about 990 cm^{-1} to 1800 cm^{-1} to eliminate the large Raman peaks due to the silica present in the fiber optic probe that obscure any tissue Raman peaks, as well as the noise present at the very end of the spectral region. The spectrum was then binned along the wavenumber axis in 3.5 cm^{-1} intervals and filtered with a 2nd order Savitzky-Golay filter for noise smoothing. Fluorescence subtraction was accomplished using an automated, modified polynomial fitting method in which a 5th order polynomial is fit to the fluorescence baseline [1].

Following data processing, a method of normalization was adopted to remove the absolute intensity information from the spectra that might be affected by many unavoidable

experimental factors. In the case of fluorescence and diffuse reflectance, the spectrum from each site of a sample was normalized with respect to the integrated intensity from that site. In the case of Raman, each spectrum was normalized to its mean spectral intensity across all Raman bands. For combined fluorescence and diffuse reflectance, the respective area-normalized spectra from each tissue site were concatenated end-to-end to form a single vector

3.2.5 Data analysis

The algorithm developed for classifying spectra was described previously [2] and consisted of two steps: i) extraction of diagnostic features from the spectra using nonlinear maximum representation and discrimination feature (MRDF) [3] and ii) development of a probabilistic scheme of classification based on sparse multinomial logistic regression (SMLR) [4] for classifying the nonlinear features into corresponding tissue categories. Each step is described in detail below.

Given a set of input data comprising samples from different classes with a given dimensionality, nonlinear MRDF aims to find a set of nonlinear transformations of the input data that optimally discriminate between the different classes in a reduced dimensionality space. It invokes nonlinear transforms, in this case restricted order polynomial mappings of the input data, in two successive stages. In the case of present spectral data, the aim of nonlinear MRDF is to compute $K<M$ ($<N$) nonlinear transformation vectors, Φ_K, from N-dimensional (where N is the number of wavelengths over which spectra were recorded) spectra of breast tissue sites, such that the projections of the input data on Φ_K from the different tissue categories are statistically well separated from each other. In the first stage, the input spectral data $\mathbf{x}$ (normalized intensities corresponding to wavelengths of the spectra) from each tissue type are raised to the power p'

35

(range of p' values from [2]) to produce the associated nonlinear input vectors $\mathbf{x}_{p'}$, which are then subject to a transform Φ'_M such that $\mathbf{y}'_M = \Phi'^T_M \mathbf{x}_{p'}$ are the first stage output features in the nonlinear feature space of reduced dimension $M << N$. In the second stage, the reduced M dimensional output features $\mathbf{y}'_M$ for each tissue type are further transformed nonlinearly to the power p (range of p values from [2]) to produce higher order features $\mathbf{y}'_{Mp}$, and a second transform Φ_K is computed so as to yield the final output features $\mathbf{y}_K = \Phi^T_K \mathbf{y}'_{Mp}$ in the nonlinear feature space of dimension K ($K \le M$). Since $p' \ne p$, this is expected to produce more general nonlinear transforms on the input spectral data, leading to improved separation of the final nonlinear features for the tissue categories in the new feature space. Thus MRDF automatically finds a closed form solution for the best set of nonlinear transforms.

Classification with SMLR is a probabilistic multi-class model based on the sparse Bayesian machine-learning framework of statistical pattern recognition. The central idea of SMLR is to separate a set of labeled input data into its constituent classes by predicting the posterior probabilities of their class membership. It computes the posterior probabilities using a multinomial logistic regression model and constructs a decision boundary that separates the data into its constituent classes based on the computed posterior probabilities following Bayes' rule. Classification of a given set of input data $\mathbf{x}$ is based on the vector of posterior probability estimates yielded by the SMLR algorithm, and a class is assigned to a spectrum for which its posterior probability is the highest:

$$\hat{y}(\mathbf{x}) = \arg\max P(y_i = 1 | \mathbf{x}) \tag{3.1}$$

An important task following development of the diagnostic algorithm was to evaluate its classification ability in an unbiased way through cross-validation. Since we had a limited number

36

of spectra in each tissue category, the cross-validation of the algorithm was performed using leave-one-sample-out cross-validation. In this method, the training of the algorithm was performed using N-1 samples (where N=74 samples), and tests were carried out using the excluded sample. This was repeated N times, each time excluding a different sample. Thus, training was achieved using, in a sense, all samples, and at the same time independence between the training and test sets was maintained.

3.2.6 Multi-Class Receiver Operating Characteristic (ROC) analysis

In order to quantitatively compare the relative performance of the diagnostic algorithms developed for fluorescence, diffuse reflectance, combined fluorescence and diffuse reflectance, and Raman spectral data sets, a multi-class receiver-operating characteristic (ROC) analysis was carried out on the classification results yielded by the corresponding algorithms. The formulation developed by Hand and Till [5] was followed for this purpose. The formulation extends the two-class ROC analysis in a straightforward way for a multi-class case, and computes a generalized metric indicative of overall performance of a given multi-class diagnostic algorithm. Given n number of classes, the Hand and Till measure (HTM) is the average of the pairwise area under the ROC curves between $n(n-1)/2$ pairs of classes:

$$HTM = \frac{2}{|n|(|n|-1)} \sum_{\{c_i, c_j\} \in C} AUC(c_i, c_j)$$

(3.2)

where AUC is the area under the two-class ROC curve involving classes c_i and c_j. The summation is calculated over all pairs of distinct classes. Similar to the two-class case, the closer the HTM is to a value of 1, the more accurate is the corresponding diagnostic algorithm.

3.3 Results

In vitro fluorescence, diffuse reflectance and Raman spectroscopic measurements were carried out on a total of 74 different tissue samples from 74 different patients. Optical spectra were acquired from 293 unique tissue sites on these samples. The details of the histopathological distribution of the tissue sites are summarized below in Table 3.1.

Table 3.1 Histological breakdown of tissue samples used in the study, along with the number of spectra recorded.

Category	No. of spectra	No. of tissue samples
Invasive ductal carcinoma (IDC)	86	25
Ductal carcinoma in-situ (DCIS)	18	6
Fibroadenoma (FA)	55	11
Normal (adipose, glandular)	134	32

Figures 3.3A-C below show the average normalized diffuse reflectance, fluorescence, and Raman spectra for IDC (86), DCIS (18), FA (55), and normal breast tissues (134). For comparison of spectral differences among the different tissue types, one can see that while fluorescence from FA tissue is visibly different than that from the rest of the tissue types throughout the spectral region, the differences among IDC, DCIS, and normal breast tissues are fairly subtle except in the 390 nm band region, where the relative band intensities show prominent differences. Similarly, while the average reflectance spectra show visible differences among all the tissue types in general, almost no difference is seen between IDC and normal breast tissue in the 590-800nm wavelength region. In contrast, the differences in the average Raman spectra appear to be somewhat more pronounced among all the tissue types across all the major Raman bands present.
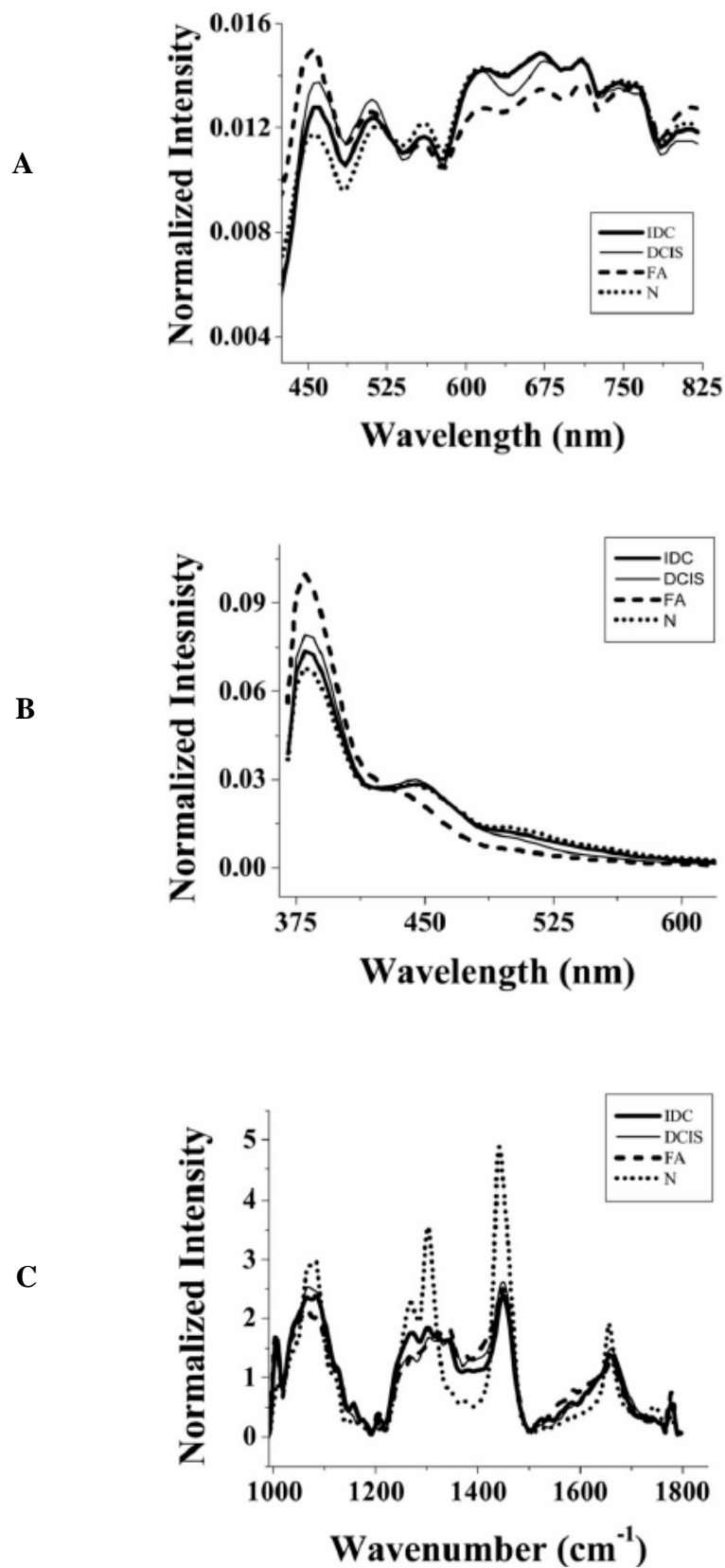
Figure 3.3 Mean (A) reflectance, (B) fluorescence, (C) Raman spectra for each tissue class

Tables 3.2 and 3.3 show the diagnostic results in the form of confusion matrices that compare the pathological diagnosis with that of the MRDF-SMLR diagnostic algorithms for the combined fluorescence and reflectance case and the Raman case, respectively. In all instances, the classification results were obtained based on leave-one-sample-out cross-validation of the entire data set. Although not shown, the diffuse reflectance data alone achieved an overall classification accuracy of 72% (211 out of 293). Its best performance was in classifying FA tissue (85% accuracy), though it fared worse in classifying other tissue types, and errors were spread among the various classes. Fluorescence data alone, again not shown, provided the worst overall accuracy, correctly classifying only 209 measurement sites (71%). It proved most adept at classifying normal breast tissues, though accuracy in that diagnosis was still only 85%.

Table 3.2 Confusion matrix for classifying breast tissue using MRDF-SMLR based algorithm with combined fluorescence and reflectance spectra.

Pathology diagnosis (# sites)	Combined fluorescence and diffuse reflectance diagnosis			
	IDC	DCIS	FA	Normal
IDC (86)	**62**	2	0	22
DCIS (18)	2	**16**	0	0
FA (55)	0	0	**54**	1
Normal (134)	17	2	0	**115**

Table 3.3 Confusion matrix for classifying breast tissue using MRDF-SMLR based algorithm with Raman spectra.

Pathology diagnosis (# sites)	Raman diagnosis			
	IDC	DCIS	FA	Normal
IDC (86)	**85**	0	0	1
DCIS (18)	0	**17**	0	1
FA (55)	0	1	**54**	0
Normal (134)	0	0	0	**134**

As seen in Table 3.2, when fluorescence and diffuse reflectance spectra were combined, the diagnostic accuracy improved quite a bit, classifying 247 out of 293 (84%) sites correctly. Normal tissues were correctly classified in 86% of cases, while DCIS and FA were classified correctly in 89% and 98% of the sites. The algorithm still struggled somewhat to classify IDC, but in general, misclassifications appeared less random than with either modality alone. With Raman spectra as the input data, as shown in Table 3.3, the algorithm discriminated all four classes very well, correctly classifying 290 out of 293 (99%) sites. Normal tissues, which include both fatty and glandular, were classified correctly for every site, while only one each IDC, DCIS, and FA sites were misclassified.

The multi-class ROC analyses of the classification results provided a quantitative evaluation of the overall performance of the diagnostic algorithms. Table 3.4 lists the *HTM* values obtained for the algorithms based on fluorescence, diffuse reflectance, combined fluorescence and reflectance, and Raman spectra. The estimated *HTM* value of the algorithm based on fluorescence spectra alone was the lowest at 0.83; those for diffuse reflectance, combined fluorescence and diffuse reflectance, and Raman spectra based algorithms are 0.88, 0.95, and 0.99, respectively.

Table 3.4 AUC_{Total} values corresponding to the diagnostic algorithms based on autofluorescence, diffuse reflectance, combined autofluorescence and diffuse reflectance, and Raman spectra of breast tissues.

AUC_{Total}	Autofluorescence	Diffuse reflectance	Combined autofluorescence and diffuse reflectance	Raman
	0.83	0.88	0.95	0.99

3.4 Discussion

Most of the studies reported to date on the application of optical spectroscopy for breast cancer detection have used one of three spectroscopic techniques: fluorescence, diffuse reflectance, or Raman scattering. However, a comprehensive, side-by-side evaluation of the relative efficacies of these different methods has not been addressed in the literature. The goal of the present study was to evaluate and compare the relative capabilities of fluorescence, diffuse reflectance, combined fluorescence and diffuse reflectance, and Raman spectroscopy for simultaneously discriminating the different histopathological categories of human breast tissues. Such an evaluation is important because it may help choose the optimal modality for a given diagnostic problem.

The primary basis for optical detection using spectroscopic techniques is an array of biochemical changes that take place as tissue undergoes neoplastic transformations. For example, IDC, FA, and normal breast tissues are known to show variable amounts of collagen and elastin, which is reflected in the fluorescence intensity of the 390 nm band characteristic of these connective tissue proteins. Similarly, the differences in the concentrations and oxidation states of coenzymes such as NADH and FAD due to metabolic changes in normal versus neoplastic breast tissues contribute to the changes in the fluorescence intensity of the broad 460 nm band [6, 7].

Some of the changes found in the fluorescence spectra of normal and abnormal breast tissues also result from changes in the wavelength dependent absorption and scattering properties of tissues. However, these changes are more prominent in the diffuse reflectance spectra of the corresponding tissue types, as diffuse reflectance provides a direct measurement of tissue absorption and scattering. For example, the several dips found in the diffuse reflectance spectra of breast tissues represent the signatures of absorption by oxygenated and deoxygenated

42

hemoglobin, which have structured absorption bands spanning nearly the entire visible and near-infrared region [7-9]. The differences in absorption properties between normal and abnormal breast tissues, as seen in Figure 3.3A, appear to be caused primarily by hemoglobin.

In contrast to fluorescence and reflectance, Raman spectroscopy probes the vibrational energy levels of molecules, and specific peaks in the Raman spectrum correspond to particular chemical bonds or bond groups. Because of Raman's chemical specificity, it has the ability to discern the slight biochemical changes associated with neoplastic transformation [10]. For example, the spectral variations between the different breast tissue pathologies observed at 1000-1150, 1170, 1200-1345, 1440, and 1650 cm^{-1} correspond to biochemical differences inherent in the different breast tissues, notably connective tissue proteins and fatty acids [10, 11]. The normal breast tissue spectra are noticeably different compared to all other categories, and are dominated by Raman bands characteristic of fatty acids (1650, 1440 and 1300 cm^{-1}). Differences between IDC, DCIS, and FA were found to be more subtle; the ratio of the bands between 1200-1300 (the amide III region due to proteins) and 1440 cm^{-1} (CH_2 bending due to proteins and lipids) varies with tissue types, and this variation is different between cancerous and non-cancerous breast tissues. Similarly, the ratio of peaks at 1650 cm^{-1} (amide I) and the small peak near 1550 cm^{-1} (amide II) is different in the IDC and FA spectra compared with DCIS. Other variations include changes in the band patterns and intensities between 1000 and 1100 cm^{-1}. In particular, the 1006 cm^{-1} peak associated with phenylalanine in collagen is stronger in the denser, more fibrous tissue spectra.

It is relevant to note here that although all the spectroscopic techniques lead to many observable spectral differences among different breast pathologies, it is more important to see the significance of these variations towards pathological classification. A gross comparison of the

classification results yielded by the four diagnostic algorithms indicates that fluorescence alone was the least capable in accurately discriminating among the four histopathologic categories of breast tissues. The performance of diffuse reflectance alone was slightly better. Although the results were improved to a large extent when fluorescence and diffuse reflectance spectra were combined, the performance of Raman spectroscopy alone was superior to that of all the other techniques employed. While diffuse reflectance primarily probes the absorption and scattering properties of tissue, fluorescence, in principle, has the additional advantage of biochemical specificity that arises from the fact that tissue contains several intrinsic fluorophores with characteristic fluorescence emission. The broad and overlapping emission profiles of these fluorophores, though, make the appearance of the resulting tissue fluorescence spectra mostly flat and featureless. This makes it difficult, though, to fully exploit this advantage in practice. In contrast, the Raman spectrum of a tissue consists of relatively narrower bands characteristic of specific molecular vibrations of a much larger number of Raman-active biochemicals present in tissue. This allows one to detect molecular information in a tissue in greater detail than with fluorescence or diffuse reflectance.

A critical evaluation of the diagnostic results discussed above reveals some interesting points. Both fluorescence and diffuse reflectance alone consistently misclassified 30-45% of IDC tissue sites as normal, and the situation did not improve much even with the combined approach, which still led to a 25% misclassification rate. In contrast, the classification accuracy of Raman alone was 99% (85 out of 86 IDC tissue sites). The likely reason for this inferior classification performance of fluorescence and diffuse reflectance becomes apparent only when one critically examines the detailed physical appearance of all the tissue samples investigated. It was found that most of the malignant tissue sites that were misclassified as normal belonged to

those IDC samples which had layers of fat on their surfaces. It is known that both fluorescence and diffuse reflectance with UV and visible light excitation can probe only the superficial tissue layer [6, 7], whereas Raman with NIR excitation can probe to a larger depth inside tissue, generally on the order of several hundred microns in typical configurations [10]. On a similar note, a total of ~13-14% of the normal tissue sites were consistently misclassified as IDC, FA, or DCIS by either fluorescence or diffuse reflectance, and the results remained the same even with the combined approach. Although the majority of the normal breast tissue samples investigated were predominantly fatty, some of them were glandular or fibrous as well. It was noticed that the normal breast tissue sites that were consistently misclassified belonged to the samples which had very high fibro-glandular content according to the pathologist.

Another important point worth considering is that when it comes to distinguishing only normal from non-normal tissues, both Raman and combined fluorescence and diffuse reflectance perform quite well. For example, the diagnostic results in Table 3.2 show that combined fluorescence and diffuse reflectance spectroscopy can discriminate tumor in general from normal breast tissues with sensitivity and specificity of 83% and 85%, respectively. If the objective is only to delineate tumor from normal breast tissues, as may be required for certain clinical procedures, the combined fluorescence and diffuse reflectance approach may serve as a method of choice. This technique can be modified as well, such as adding polarization optics to provide depth-dependent information [12] to perhaps overcome the limitations of fluorescence and diffuse reflectance discussed above. A further incentive towards using this approach is that, given currently available instruments and the inherent differences in signal strengths, combined fluorescence and diffuse reflectance is a viable candidate for macroscopic imaging techniques, while Raman is not. In many applications, such as evaluating margin status during breast

conserving therapy, it is highly desirable to move to an imaging-based system rather than point spectroscopy to gather more information from an entire tissue surface in a much quicker time. At this point, one can perhaps think of exploiting the advantages of all three spectroscopic techniques in one setting by combining imaging based on combined fluorescence and diffuse reflectance with Raman-based point spectroscopy if the goal is to cover a larger area while also having the ability to investigate smaller suspicious areas with a an even more accurate technique to distinguish normal from non-normal tissue.

3.5 References

1.   C. A. Lieber, and A. Mahadevan-Jansen, "Automated method for subtraction of fluorescence from biological Raman spectra," Appl Spectrosc **57**, 1363-1367 (2003).

2.   S. K. Majumder, S. Gebhart, M. D. Johnson, R. Thompson, W. C. Lin, and A. Mahadevan-Jansen, "A probability-based spectroscopic diagnostic algorithm for simultaneous discrimination of brain tumor and tumor margins from normal brain tissue," Appl Spectrosc **61**, 548-557 (2007).

3.   A. Talukder, and D. Casasent, "General methodology for simultaneous representation and discrimination of multiple object classes," Optical Engineering **37**, 904-913 (1998).

4.   B. Krishnapuram, L. Carin, M. A. T. Figueiredo, and A. J. Hartemink, "Sparse multinomial logistic regression: Fast algorithms and generalization bounds," Ieee Transactions on Pattern Analysis and Machine Intelligence **27**, 957-968 (2005).

5.   D. J. Hand, and R. J. Till, "A simple generalization of the area under the ROC curve for multiclass classification problems," Machine Learning **45**, 171-186 (2001).

6.   N. Ramanujam, "Fluorescence spectroscopy of neoplastic and non-neoplastic tissues," Neoplasia **2**, 89-117 (2000).

7.   R. Richards-Kortum, and E. Sevick-Muraca, "Quantitative optical spectroscopy for tissue diagnosis," Annu Rev Phys Chem **47**, 555-606 (1996).

8.   I. J. Bigio, S. G. Bown, G. Briggs, C. Kelley, S. Lakhani, D. Pickard, P. M. Ripley, I. G. Rose, and C. Saunders, "Diagnosis of breast cancer using elastic-scattering spectroscopy: preliminary clinical results," J Biomed Opt **5**, 221-228 (2000).

9.   G. M. Palmer, C. Zhu, T. M. Breslin, F. Xu, K. W. Gilchrist, and N. Ramanujam, "Comparison of multiexcitation fluorescence and diffuse reflectance spectroscopy for the diagnosis of breast cancer (March 2003)," IEEE Trans Biomed Eng **50**, 1233-1242 (2003).

10.   A. Mahadevan-Jansen, "Raman Spectroscopy: From Benchtop to Bedside," in *Biomedical Photonics Handbook*, T. Vo-Dinh, ed. (CRC Press, Washington DC, 2003), pp. 30:31-30:27.

11.   R. R. Alfano, C. H. Liu, W. L. Sha, H. R. Zhu, D. L. Akins, J. Cleary, R. Prudente, and E. Celmer, "Human breast tissue studied by IR Fourier transform Raman spectroscopy," Laser Life Sci **4**, 23-28 (1991).

12.   N. Ghosh, S. K. Majumder, H. S. Patel, and P. K. Gupta, "Depth-resolved fluorescence measurement in a layered turbid medium by polarized fluorescence spectroscopy," Opt Lett **30**, 162-164 (2005).

CHAPTER IV

AUTOFLUORESCENCE AND DIFFUSE REFLECTANCE SPECTROSCOPY AND

SPECTRAL IMAGING FOR BREAST SURGICAL MARGIN ANALYSIS

4.1 Abstract

Most women with early stage breast cancer have the option of breast conserving therapy, which involves a partial mastectomy for removal of the primary tumor, usually followed by radiotherapy. The presence of tumor at or near the margin is strongly correlated with the risk of local tumor recurrence, so there is a need for a non-invasive, real-time tool to evaluate margin status. This study examined the use of autofluorescence and diffuse reflectance spectroscopy and spectral imaging to evaluate margin status intraoperatively. Spectral measurements were taken from the surface of the tissue mass immediately following removal during partial mastectomies and/or from tissues immediately after sectioning by surgical pathology. A total of 145 normal spectra were obtained from 28 patients, and 34 tumor spectra were obtained from 12 patients. After correlation with histopathology, a multivariate statistical algorithm classified the spectra as normal (negative margins) or tumor (positive margins) with 85% sensitivity and 96% specificity. A separate algorithm achieved 100% classification between neo-adjuvant chemotherapy-treated tissues and non-treated tissues, and fluorescence and reflectance-based spectral images were able to demarcate a calcified lesion on the surface of a resected specimen as well. With these results, fluorescence and reflectance spectroscopy could be a valuable tool for examining the superficial margin status of excised breast tumor specimens, particularly in the form of spectral imaging to examine entire margins in a single acquisition.

4.2 Introduction

Of the approximately 180,000 patients each year diagnosed with early-stage invasive breast cancer or breast carcinoma *in situ* [1], most have the option of breast conserving therapy (BCT). This method consists of removing the primary breast lesion via a lumpectomy, or partial mastectomy, which is often followed by directed radiotherapy. To be successful, the surgical portion of BCT must ensure that no tumor cells remain within a specified distance of the surgical margin on the removed specimen; this case is described as negative margins. The presence of positive margins is strongly correlated with the risk of local tumor recurrence and necessitates a second operation for the patient [2]. The exact size of the negative margin required varies significantly among different hospitals and can range from simply finding no tumor cells on the surface to having > 5 mm between tumor cells and the surface of the specimen [3, 4]. Some women with tumors considered too large for BCT may elect to have neo-adjuvant chemotherapy (NAC) to shrink the tumor and eliminate the necessity of a total mastectomy [5, 6]. NAC has also been shown to improve the prognosis following BCT for some groups of women [5, 6].

Currently available methods of evaluating margin status intraoperatively include visual inspection of the excised tissue by the surgeon, which is incorrect in at least 25% of cases [7]. Frozen section pathology and cytological examination ("touch prep") are commonly used but require tissue to be sent to pathology and are prone to sampling error [7, 8]. While ultrasound is available in the operating room, its poor spatial resolution results in limited sensitivity [7, 9]. The current gold standard in margin analysis is serial sectioning with standard histopathology, but results may take several days to over a week. These limitations emphasize the need for a real-time, intraoperative margin evaluation tool that can assure complete removal of breast tumors with negative margins in a single procedure.

Autofluorescence and diffuse reflectance spectroscopy have been researched extensively as a diagnostic tool for discriminating among normal, malignant, and/or benign breast tissues [10-22]. Some of the most extensive recent work has been performed by Ramanujam et. al., who have used numerous approaches to discriminate breast tissues with autofluorescence and/or diffuse reflectance, including the use of multiple excitation wavelengths [23, 24], multiple source-detector fiber separations [25], and Monte Carlo-based extraction algorithms [26-28]. The use of diffuse reflectance as well as intrinsic fluorescence from molecules like collagen and NADH for breast tissue classification was explored by Feld et. al. [29]. Most of this work, though, is focused on diagnostic applications rather than on therapeutic guidance. One exception to this comment is a study performed by Bigio et. al. using *in vivo* elastic scattering measurements to both make a diagnosis and help guide resection; they were able to distinguish malignant from normal tissue with sensitivities up to 69% and specificities up to 93% [30].

In a previous *ex vivo* study in our lab, autofluorescence (excited at 337 nm) and diffuse reflectance (400-800 nm) were used to classify breast tissue samples into four categories: invasive ductal carcinoma (IDC), ductal carcinoma *in situ* (DCIS), fibroadenoma (FA), and normal. Using a multi-class discrimination algorithm with leave-one-sample-out cross-validation, fluorescence only, reflectance only, and combined (concatenated) fluorescence and reflectance classified tissues with 72%, 71%, and 84% accuracies, respectively. The combined approach also had ~ 84% sensitivity and 90% specificity for distinguishing normal/benign tissue from malignant tissues in general [31].

The problem with the above approaches for intraoperative margin analysis is that probing a small area (~1mm diameter) at a time for each measurement on a sample that is typically at least a few centimeters in diameter is not very practical. Fluorescence and diffuse reflectance-

based multi-spectral imaging would be better suited for this application; this approach records reflectance and fluorescence spectra for each pixel in an image. In separate work in our lab, combined fluorescence and reflectance spectroscopy discriminated normal, tumor core, and tumor margin tissues in the brain with a 95% classification rate [32]. A multi-spectral imaging system with a 25 mm by 25 mm field of view was then developed, and its use has produced results similar to those obtained with the point spectroscopy system [33].

Based on these past results with breast and brain tissues, the goal of this study was to investigate the use of combined autofluorescence and diffuse reflectance spectroscopy and spectral imaging for evaluating the status of surgical margins intraoperatively during lumpectomies. Point spectra were gathered from freshly excised breast tissue specimens and correlated with histopathology/margin status at the measurement locations. In one case, spectral images were obtained as well to assess the feasibility of that approach.

4.3 Materials and Methods

4.3.1 Patient data

Women undergoing breast conserving therapy or, in some cases, total mastectomy, were recruited for this study by the surgical oncologists (MK and IM). Informed consent was obtained under a protocol approved by the Vanderbilt University Institutional Review Board (IRB #060554) and Vanderbilt-Ingram Cancer Center Scientific Review Committee (BRE 0718). Table 4.1 displays the breakdown of the types of measurements taken, after excluding spectra for which no detailed pathology was available. Spectra were also excluded if they showed drastically altered shapes due to strong absorption by blood (this was minimized by rinsing the tissue with saline) or by a blue dye used to identify sentinel lymph nodes; interference from the

Table 4.1. Breakdown of measurements by tissue types and by numbers of patients.

Tissue Category	Number of Spectra	Number of Patients
Normal	145	28
Tumor (IDC, DCIS)	34	12

blue dye was mostly eliminated by the surgeons' changing the site of its injection. A total of 145 spectra from clinically normal tissues, indicative of negative margins, from 28 patients were used in the below analysis. A total of 34 such spectra were obtained from tissue sites containing tumors (IDC or DCIS) within ~1 mm in depth from the measurement surface, indicative of positive margins, from 12 patients. Eight of the patients had measurements taken from both normal and tumor regions. An average of five to six, minimum of one, and maximum of 12 spectra were used from any one patient; however, the maximum number of spectra from a given tissue type from any one patient was seven. In addition, a total of 19 spectra were obtained from normal regions of three patients who had undergone neo-adjuvant chemotherapy; these spectra were excluded from further analysis except where explicitly noted. Due to the nature of the study population, no measurements were obtained from benign tumors such as fibroadenomas.

4.3.2 Instrumentation

Autofluorescence and diffuse reflectance spectra of breast tissues were measured using a portable spectroscopic system. A high-pressure nitrogen laser (Spectra Physics, Mountain View, CA) at 337 nm was used as the excitation source for autofluorescence measurements, and a 150-Watt tungsten-halogen lamp (Ocean Optics, Dunedin, FL) emitting broadband white light from 400 nm to 800 nm was used for diffuse reflectance measurements. Light delivery to and

collection from the sample was achieved with a fiber optic probe (Romack, Williamsburg, VA) consisting of seven 300 μm core diameter fibers arranged in a six-around-one configuration. Two of the surrounding fibers delivered laser and white light consecutively to the tissue sample while the remaining fibers collected autofluorescence and diffuse reflectance from the tissue sample. Emissions collected by the fiber optic probe were serially dispersed and detected with a chip-based spectrometer (Ocean Optics, Dunedin, FL). For autofluorescence measurements, reflected laser light was eliminated with a 365 nm long-pass filter placed in front of the entrance slit of the spectrometer. For this study, the output power of the white light was ~0.6 mW at the tissue surface, and the nitrogen laser was operated at a 20-Hz repetition rate, 5-nanosecond pulse width, and average pulse energy of 45±5 μJ at the tissue surface. An integration time of 100 ms was used for each spectral measurement.

Spectral images were obtained with a liquid-crystal tunable filter (LCTF) spectral imaging system, as previously described [33]. Briefly, a Varispec VIS-20 LCTF (CRI, Inc., Woburn, MA) was used to cycle through a user-defined range of detection wavelengths between 400 and 720 nm, and emitted light was collected with a variable focal-length camera lens (f/3.5, Nikon, Tokyo, Japan). Images at each defined wavelength were collected with a thermo-electrically cooled CCD camera (PhotonMax, Princeton Instruments, Princeton, NJ) to create a 3D data cube. Images were acquired in a non-contact manner with a 25 mm by 25 mm field of view and an object distance of 180 mm. A 500 W xenon arc lamp, bandpass filtered at 340 nm, was used for fluorescence excitation, while a 200 W halogen lamp (Luxtec, West Boylston, MA) was used for diffuse reflectance excitation. A 365 nm dichroic filter coupled both illumination sources into a single, 10-mm-core liquid light guide to deliver the excitation light to the sample.

4.3.3 Data acquisition

For lumpectomy procedures, autofluorescence and diffuse reflectance spectra were obtained from one point on each of the six facets of the removed specimen as soon as it was resected in the operating room. Additional measurements on the surface were made at times at the surgeon's discretion. If a large residual tumor was present and time permitted (i.e. it was done within ~30 minutes of removal), or for total mastectomy procedures, measurements were taken after initial gross sectioning of the tissue. Taking such measurements from sections including tumors was necessary to increase the sample size of tumor/positive margin measurements. For spectral imaging, one fluorescence and one reflectance image, along with the corresponding baseline image, were acquired for three of the six margins of the lumpectomy specimen. Total acquisition time for each margin was approximately 60-90 seconds.

In all point spectroscopy cases, the measured spots were marked for correlation with histopathology. For the standard six measurements on lumpectomies described above, surgical sutures were used both to orient the specimen and to indicate the measurement spots. For all other measurements, the spots were marked with a standard tissue dye. The marked spots were sampled by a trained pathologist (FB or GO) via shave biopsies for correlating the spectra with tissue histopathology. All findings were interpreted as they would be for margin analysis - i.e., any measured spots with malignant cells within 1mm of the surface on which the probe was placed were deemed to be tumor/positive margins. Thus, the phrases normal tissue or negative margins, and tumor tissue or positive margins are used interchangeably throughout the text.

4.3.4 Data processing and analysis

After autofluorescence and diffuse reflectance spectral acquisition, a set of reference

spectra from a fluorescence and a reflectance standard were recorded to correct for inter-sample variability due to variations in laser-pulse energy and white light power. The fluorescence standard was a low-concentration Rhodamine 6G solution (2mg/L) contained in a quartz cuvette, and the reflectance standard was a 20 % reflectance plate (Labsphere, North Sutton, NH) placed in a black box. All subsequent processing and analysis was performed in MATLAB 7.0.1 (Mathworks, Natick, MA). Raw fluorescence and diffuse reflectance spectra were processed to remove instrumentation-induced variations and to yield calibrated spectra, the details of which are described elsewhere [34]. Autofluorescence spectra were truncated from 365-650 nm, and diffuse reflectance spectra were truncated from 400-800 nm. The resultant spectra were further corrected for the non-uniform spectral response of the detection system and normalized to the overall integrated intensity to remove the absolute intensity information from the spectra that might be affected by many unavoidable experimental factors.

The processed fluorescence and reflectance spectra were merged prior to analysis with a two-part classification method, which was performed with leave-one-patient-out cross-validation. Maximum representation and discrimination feature (MRDF) was first used to reduce the dimensionality of the data and to extract the relevant diagnostic features. Those output features were then classified by sparse multinomial logistic regression (SMLR), which assigned a posterior probability of the measured spectrum belonging to each of the tissue classes. The spectrum was assigned to the category for which it had the highest probability of membership. More complete details on this procedure can be found in previous papers [31, 32]. In this case, tissues from measurement sites were classified only as normal/negative or tumor/positive because to the surgeon, knowing whether the tissue is something that should be removed is sufficient. Also, due to the nature of patients undergoing partial or total

mastectomies, no measurements of benign tumors or other such conditions were possible. Since the excised tissues were only sampled in a limited manner, analysis of margin status was limited to only those points directly sampled by the probe.

The spectral images were corrected for sensitivity of the detector and transmission of the LCTF, as well as for the lineshape of illumination in the case of reflectance images. Fluorescence images were binned over a 2 by 2 pixel area to account for the weaker nature of fluorescence. To display individual spectra from a point on the image, the spectra from a 20 by 20 pixel area (~1 mm^2) were averaged to match the size of the fiber probe. No quantitative analysis was done with the images since they were a simple test of feasibility.

4.4 Results

Mean, normalized autofluorescence and diffuse reflectance spectra, plus and minus one standard deviation for normal tissue / negative margins (n = 145) and tumor tissue / positive margins (n = 34) from 32 patients are shown in Figures 1A and 1B, respectively. The fluorescence spectra in Figure 1A show a variety of differences between normal and tumor tissues, notably a relatively more intense peak around 390 nm in tumor tissues compared with normal, and relatively greater contributions at wavelengths longer than about 475 nm in spectra from normal tissues. The 390 nm peak is generally attributed to collagen, while the most significant differences past ~475 nm are associated with the tail of the NADH emission spectrum and the broad peak of flavins from about 500 to 550 nm. The reflectance spectra do not show as visually obvious significant differences between the two tissue types, as the error bars always overlap. The normal reflectance spectra show an overall higher slope, though, and in many regions, the mean of each tissue class lies outside the error bars around the other class's mean.
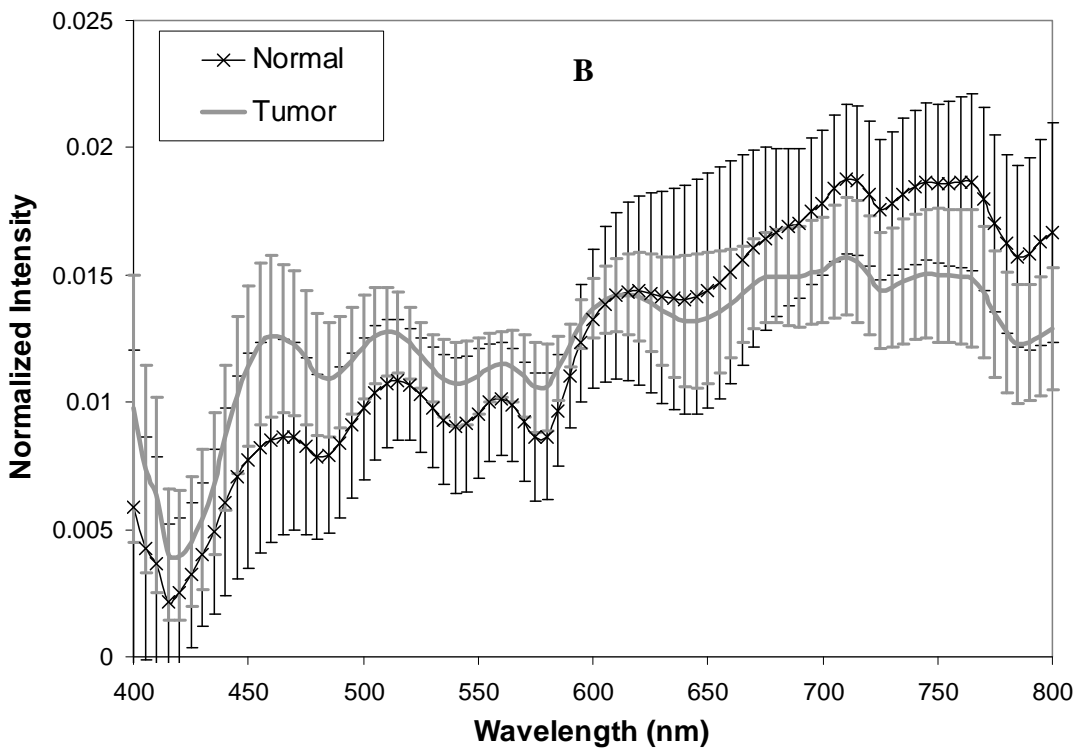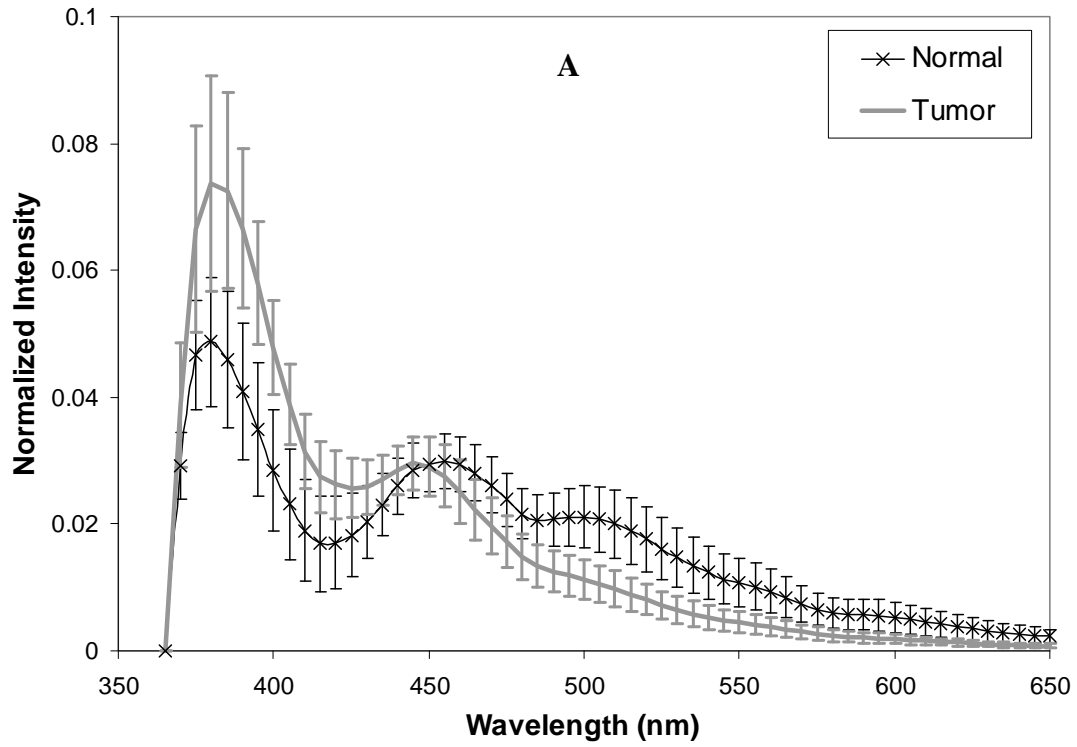
Figure 4.1. Mean, normalized (A) autofluorescence and (B) diffuse reflectance spectra for patients not receiving neo-adjuvant chemotherapy. Error bars represent one standard deviation.

Table 4.2 shows the confusion matrix for the performance of the MRDF-SMLR algorithm for combined fluorescence and reflectance with leave-one-patient-out cross-validation

Table 4.2. Confusion matrix for classification of non-chemo-treated tissues only.

		Spectral Classification		
		Normal	Tumor	
Histopathology	Normal	139	6	Specificity: 96%
Diagnosis	Tumor	5	29	Sensitivity: 85%
		NPV: 97%	PPV: 83%	

on all non-chemo-treated patients. Normal tissue, indicative of negative margins, was discriminated from tumor tissue / positive margins with 85% sensitivity and 96% specificity, or 83% positive predictive value (PPV) and 97% negative predictive value (NPV), or an overall accuracy of 94%. Figure 4.2 shows the posterior probabilities, as determined by SMLR, of each
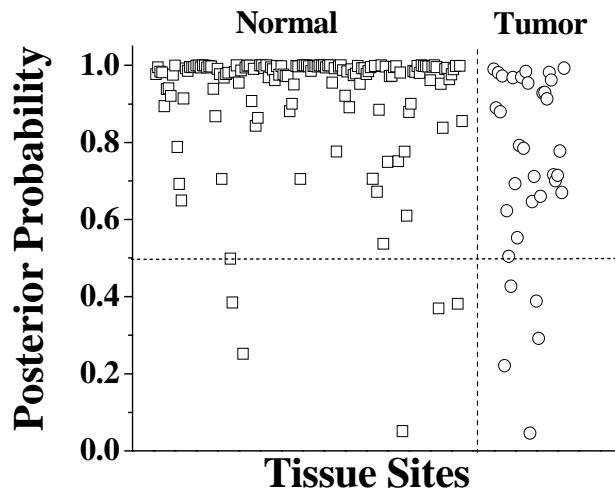
Figure 4.2. Results of SMLR classification. Each symbol denotes an interrogated tissue site (squares on left for histopathologically normal, circles on right for tumor), with their associated posterior probabilities of belonging to their true tissue class according to the spectral classification.

measured spectrum belonging to its true class, as determined by histopathology. Shapes near 1.0 on the vertical axis represent spectra that were determined to have a high probability of being obtained from the correct tissue type, while those below 0.5 represent spectra that were misclassified. Most normal tissue sites were classified with high probabilities, while tumor tissue probabilities are more spread out, but are still well classified.
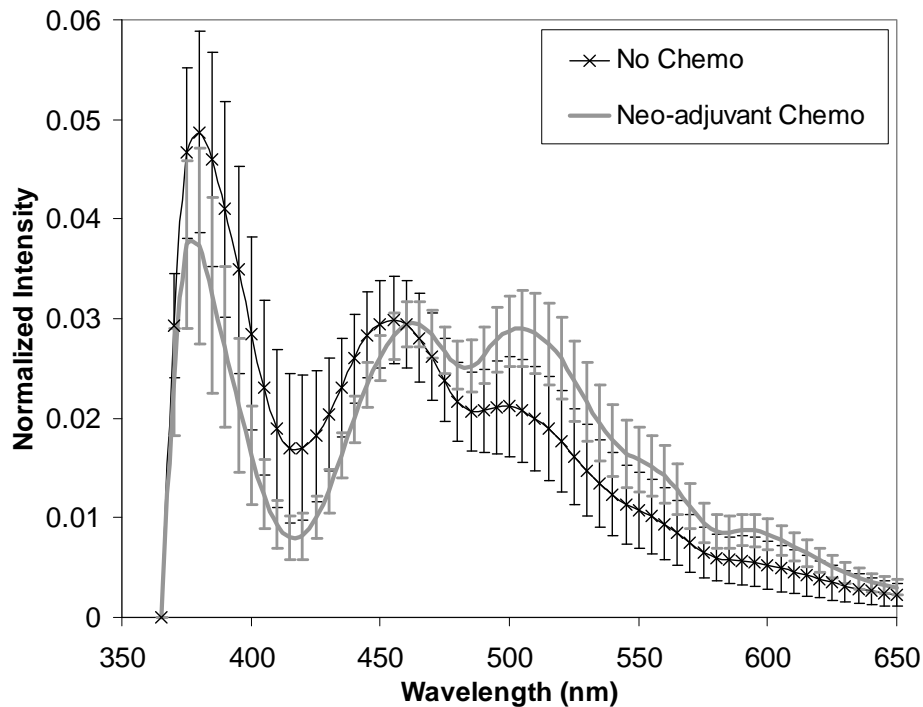
Figure 4.3. Mean, normalized autofluorescence spectra, plus or minus one standard deviation, for normal tissue measurements with and without neo-adjuvant chemotherapy.

Figure 4.3 displays the mean fluorescence spectra from all normal tissue sites without (n = 145) and with (n = 19) neo-adjuvant chemotherapy. The spectra from sites with NAC were excluded from the previous analysis. Although the sample size of NAC-treated normal tissues is fairly small, the spectra show a significant difference from non-NAC-treated normal tissues in the peak around 500 nm. As seen in Table 4.3, MRDF-SMLR was able to classify spectra according to the use of NAC with 100% sensitivity and specificity.

Table 4.3. Confusion matrix for classifying all normal tissues according to the use of neo-adjuvant chemotherapy.

		Spectral Classification	
		No Chemo	Neo-adjuvant Chemo
Chemotherapy Status	No Chemo	145	0
	Neo-adjuvant Chemo	0	19

Figure 4.4A (below) shows a sample fluorescence spectral image of breast tissue following a lumpectomy, while Figure 4.4B shows the corresponding reflectance spectral image (both false-colored). The areas marked by 1 and 2 in the images correspond to a calcified lesion "abutting the margin" and normal tissue, respectively. The normalized fluorescence and reflectance spectra obtained from averaging a 20 by 20 pixel region at the marked sites are shown in Figures 4C and 4D, respectively. These two regions were difficult to distinguish on the tissue surface with the naked eye and were only slightly easier to distinguish in Figure 4.4B, as evidenced by the relatively small reflectance spectral differences in Figure 4.4D. The same areas do show apparent fluorescence spectral differences in Figure 4.4C, though, and they are easily distinguished and delineated in Figure 4.4A.

4.5 Discussion

The goal of the present study was to investigate the use of combined autofluorescence and diffuse reflectance spectroscopy and spectral imaging for evaluating the status of breast surgical margins. As seen in Figure 4.1A, the normalized fluorescence spectra from tumor / positive margin and normal / negative margin sites show a number of differences. As previously mentioned, the most significant differences are seen at spectral regions usually associated with
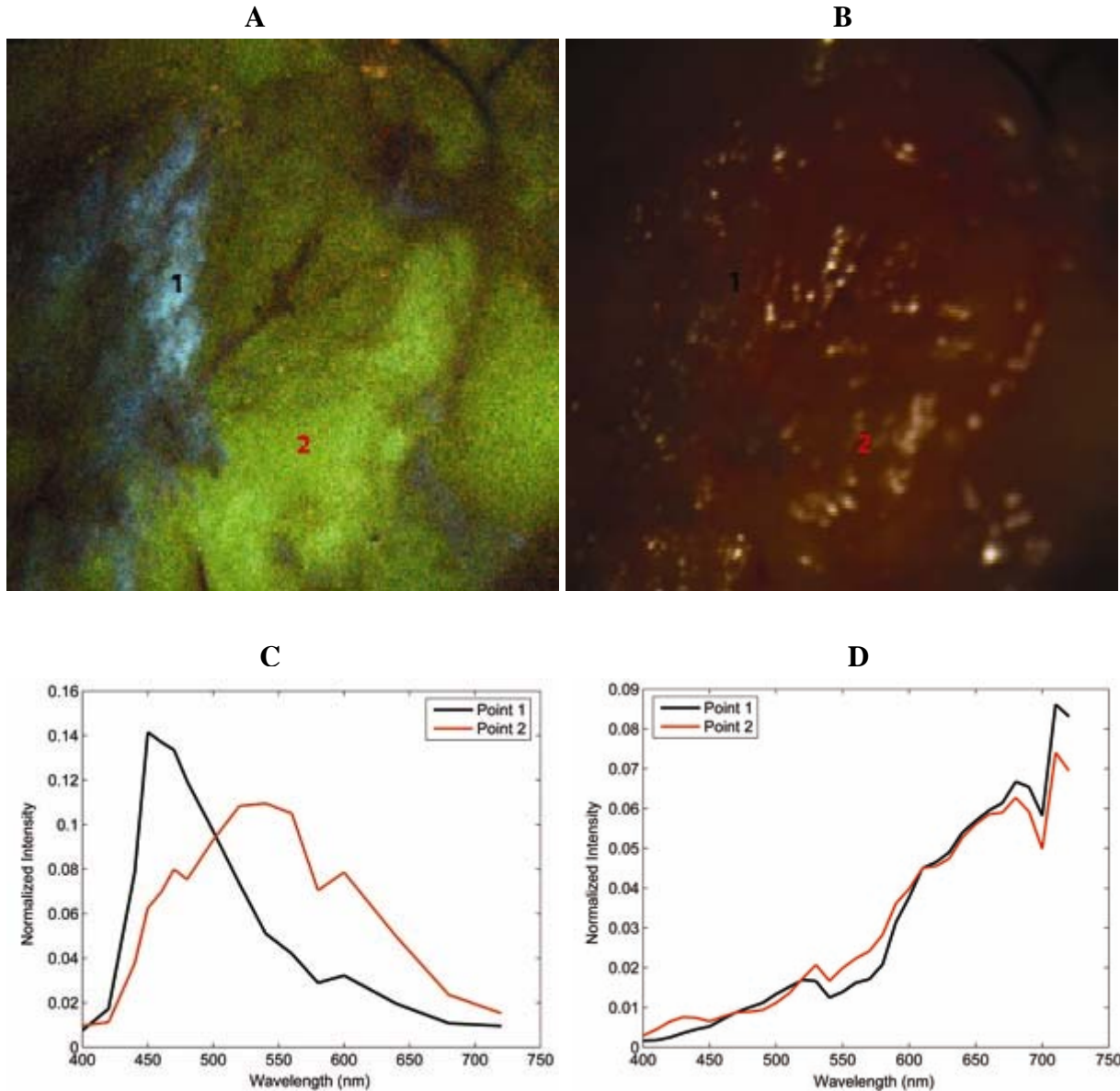
Figure 4.4. Spectral images and selected spectra from a lumpectomy specimen. (A) Fluorescence spectral image. (B) Diffuse reflectance spectral image. (C) Fluorescence and (D) diffuse reflectance spectra corresponding to points 1 and 2 in (A) and (B), respectively.

collagen around 390 nm, with the tail of NADH emission approaching 500 nm, and with flavins from around 500 to 550 nm. These changes are consistent with those seen in other studies [26, 29, 31] and result from structural and metabolic changes associated with cancer. Normalized diffuse reflectance spectra, as seen in Figure 4.1B, show some visual differences between normal

and tumor tissues, but not as significant as for some regions of the fluorescence spectra.

As seen in Table 4.2, the algorithm based on MRDF and SMLR classified the combined fluorescence and reflectance spectra from non-NAC-treated tissues as normal or tumor with 85% sensitivity and 96% specificity, with an overall classification accuracy of 94%. Of the six false positive results, one measurement was taken from a margin that was deemed positive by surgical pathology, but the shave biopsy from the measurement point was determined to be normal tissue. It is possible that the sampling was slightly off, or that the measurements were sensitive to nearby disease in an area deemed histologically normal. Two false positive diagnoses were from a single very dense, collagenous normal specimen. Another false positive came from a tissue sample with a positive finding at a different margin, while the other two had no notes indicating a possible reason for misclassification. Of the five false negatives, one measurement site had a ~1 mm layer of fat over the tumor, which is likely at or near the limit of margin size that these modalities can evaluate. No specific reasons for other misclassifications could be identified.

In terms of a clinical application, the most interesting statistic is likely negative predictive value. The surgeon would like to be confident that any diagnosis of normal or negative margins is an accurate one, and he or she is not leaving any tumor tissue in the patient. A high positive predictive value would be desirable as well to avoid unnecessary re-excisions during the operation. From this data set, the negative predictive value is 97%, and the positive predictive value is 83%. Although there were close to five times as many negative spectra as positive, predictive values often taken into account different population sizes, and the distribution of measurements in this sample set is a reasonable approximation of what might be encountered in actual medical use.

As seen in Figure 4.2, the MRDF-SMLR algorithm determined the class membership of

normal tissues with mostly high posterior probabilities. It showed less certainty in its classification of tumor tissues, seen by the greater spread of the circles on the y-axis, but still provided strong classification overall. One strength of this analysis technique is its probabilistic nature. It can provide a surgeon with the likelihood that a given measurement site is normal, indicating negative margins, or that the site contains tumor features and therefore represents a positive margin. Although two measurements may both be classified as tumor, their actual posterior probabilities of being such could differ by up to 0.49, from 0.51 to 1.0; this kind of information would be very useful in making informed medical decisions.

A number of decisions on the treatment of the data were made in the above analysis. When both non-normalized fluorescence and reflectance spectra (not shown) are examined, tumor tissue spectra are generally more intense across all wavelengths than normal spectra, a result which has been seen before [14]. Although that information may be diagnostically useful, given the difficulty of tightly controlling the measurement environment in an operating room, we felt it prudent to normalize spectra to area under the curve rather than to an intensity standard. The classification ability of either modality by itself was not evaluated; rather, the merged spectra were used since we found in a previous study on breast tissues that doing so significantly increased classification performance over the individual modalities [31]. That previous study used the same instrumentation, data processing, and data analysis procedures as this study. Further, the relative means, amount of error bar overlap between categories, etc. are similar for the two studies. On a related note, intrinsic fluorescence spectra were not extracted as part of this study. Though some studies have seen success with extracting such spectra and/or individual tissue parameters from reflectance spectra, MRDF-SMLR has achieved excellent classification results without first performing these additional mathematical procedures [31, 32].

It is possible, though, that performing such extractions could improve future evaluation algorithms from larger, more diverse data sets.

The classification performance presented in this paper compares favorably with other recent work on the use of combined fluorescence and reflectance for *ex vivo* breast tissue discrimination. The most recent work of Zhu and Ramanujam et. al. was able to classify malignant versus normal/benign tissues with up to 87% sensitivity, 89% specificity, and 88% overall accuracy using a support vector machine (SVM) on empirically chosen principal components, or with 89% sensitivity, specificity, and overall accuracy using a SVM on parameters extracted from the spectra with a Monte Carlo model [27]. A paper by Volynskaya and Feld et. al. used a diffusion equation-based model to extract parameters that were fed into a stepwise classification algorithm. That system classified spectra as malignant or normal/benign with 100% sensitivity and 96% specificity, as well as 91% overall accuracy, which reflects some normal and benign sites being misclassified among the three possible such categories. If only diffuse reflectance spectra were analyzed, they achieved 100% sensitivity and specificity, but with 81% overall accuracy [29].

It is difficult to truly compare the results in this paper and the two studies discussed above due to a number of factors. While all three obtain measurements shortly after excision, techniques vary between and within studies as to whether they are recorded in the operating room or after sectioning by pathology. The measurements in this paper were obtained as they would be for intraoperative margin analysis, while the others were focused on measuring specific diseased or normal areas. Slightly different wavelength ranges are used, and several physical components of the measurement systems are different among all three studies. Both above studies correct the fluorescence measurements to obtain intrinsic fluorescence spectra, while this

study did not, for reasons stated above. While all three studies use some form of spectral normalization, the implementations vary. The analysis methods differ as well, both in the statistical technique and in the number of tissue categories considered. Overall, the results presented in this paper for using combined fluorescence and reflectance to distinguish between malignant and normal/benign tissues are slightly better than the same measure presented by Zhu et. al. [27] but slightly worse than those of Volynskaya et. al. [29]. The reasons for this could be any of the factors discussed above. The MRDF-SMLR algorithm is the only one, to our knowledge, that displays probabilities of class membership as well.

Another interesting aspect of this study was looking at the effects of neo-adjuvant chemotherapy on measurements from normal breast tissues. No measurements from NAC-treated tumor measurements were available because in those cases, the tumors had been significantly shrunk by the chemotherapy. Most studies exclude such data, as this paper did in above analyses, since NAC can affect the biochemistry of the tissue. As seen in Figure 4.3, the only area of significant difference between normalized mean spectra of normal tissues with and without NAC is a peak around 500 nm. This finding is interesting because a similar phenomenon is seen in brain tissues with radiation damage [35]. No mechanism for this common finding has been proposed, but it is logical that chemotherapy and radiation could induce similar biochemical responses in tissues near tumors.

From Table 4.3, these spectral differences allowed perfect classification of spectra from normal tissues according to NAC treatment status. Although not shown in the table, if tumor spectra from patients not undergoing NAC were included as a third category, the 19 NAC-treated normal tissues were still classified with 100% accuracy, and no other spectra were classified as being NAC-treated. With only 19 spectra from three patients in the NAC category, these

analyses were not well-powered, and from a clinical perspective, "classifying" tissues according to NAC status is not relevant since that status is know *a priori*. These analyses do show that in future development of a clinical algorithm from a larger patient population, it is likely necessary to stratify tissue classes according to both histopathology and use of NAC since the chemotherapy alters the (normal) spectra.

This paper is the first, to our knowledge, to present wide-field fluorescence and reflectance-based spectral imaging data from *ex vivo* breast tissues. The spectral images and corresponding spectra from Figure 4.4 demonstrate the feasibility of this modality for evaluating the surgical margin status of a lumpectomy specimen over a large area. The images in Figure 4.4 are of a margin with a calcified lesion, which are typically treated as malignant, "abutting the margin" that was very difficult to see with the naked eye. It is also somewhat difficult to see in the reflectance image in Figure 4.4B, but it shows up as a very distinct blue-colored region in Figure 4.4A, labeled with the number 1. The spectra in Figures 4.4C-D corresponding to that lesion and to normal, fatty tissue (the number 2) confirm that these regions have very different fluorescent properties that can be demarcated on spectral images. From this very limited data set, it appears that such spectral imaging is a good candidate for evaluating the entire surface of excised breast specimens. Clear images can be obtained for a 25 mm by 25 mm field of view in a matter of minutes, and spectra with large signal to noise ratios can be obtained by averaging the spectra from a 20 by 20 pixel (1 mm^2) area. This area is equivalent to the area interrogated by the optical fiber probe and provides more than adequate spatial resolution to the surgeon.

A major limiting factor in moving from spectroscopy to imaging is the differing lineshapes of the recorded spectra [36]. Although the wavelength ranges are different, one can see that the general shapes of the fluorescence spectra from Figure 4.1A vs. 4C and the

reflectance spectra from 1B vs. 4D are different, despite all being corrected for system responses. The fluorescence spectra in Figure 4.4C show the same trends relative to each other as they do in Figure 4.1A, although both are much less intense near 400 nm. The reflectance spectra from Figure 4.4D have a much higher slope compared with those from Figure 4.1B. Both of these observations match those seen previously [36]. As a result, some kind of correction must be developed if one wishes to directly compare measurements from point spectroscopy versus imaging, or one can simply develop separate algorithms and compare the performance of the two, as was done with an analogous brain tumor demarcation study [33]. Given the preliminary nature of the spectral imaging data in this study, no attempt was made to correct its spectra to match those from the fiber probe instrument.

This paper has demonstrated that fluorescence and reflectance spectroscopy can evaluate the margin status of excised breast specimens with high sensitivity and specificity. In its current form, the technique presented in this paper would be clinically useful for the ~46 % of North American institutions that do not require negative margins > 1 mm [4]. The point-based measurements allow good discrimination, and the spectral imaging case indicates the promise of interrogating larger areas of tissue in clinically feasible times. Since the penetration depth of the wavelength range used in this study is not as deep as would be desired by many clinics, though, more advanced techniques would be needed to examine margin status to a greater depth. If polarized excitation light is used, varying the relative angle of a polarizer in the detection leg can make fluorescence measurements more or less sensitive to surface vs. deeper tissue components [37-39]. Unfortunately this technique did not provide additional depth information in practice. Another method to probe deeper into tissue is to physically separate the source and detector fibers to collect photons that have traveled further beneath the tissue surface after undergoing

multiple scattering [40]. If using a contact probe-based approach, though, it would likely make more sense to do so with Raman spectroscopy to take advantage of its deeper penetration depth and better ability to classify breast tissues [31].

4.6 Acknowledgments

4.7 References

1.   American Cancer Society, "Cancer Facts and Figures 2009," (American Cancer Society, Atlanta, 2009).

2.   K. C. Horst, M. C. Smitt, D. R. Goffinet, and R. W. Carlson, "Predictors of local recurrence after breast-conservation therapy," Clin Breast Cancer **5**, 425-438 (2005).

3.   C. Dunne, J. P. Burke, M. Morrow, and M. R. Kell, "Effect of margin status on local recurrence after breast conservation and radiation therapy for ductal carcinoma in situ," J Clin Oncol **27**, 1615-1620 (2009).

4.   A. Taghian, M. Mohiuddin, R. Jagsi, S. Goldberg, E. Ceilley, and S. Powell, "Current perceptions regarding surgical margin status after breast-conserving therapy: results of a survey," Annals of surgery **241**, 629-639 (2005).

5.   J. R. Gralow, H. J. Burstein, W. Wood, G. N. Hortobagyi, L. Gianni, G. von Minckwitz, A. U. Buzdar, I. E. Smith, W. F. Symmans, B. Singh, and E. P. Winer, "Preoperative therapy in invasive breast cancer: pathologic assessment and systemic therapy issues in operable disease," J Clin Oncol **26**, 814-819 (2008).

6.   D. Bafaloukos, "Neo-adjuvant therapy in breast cancer," Ann Oncol **16 Suppl 2**, ii174-181 (2005).

7.   G. C. Balch, S. K. Mithani, J. F. Simpson, and M. C. Kelley, "Accuracy of intraoperative gross examination of surgical margin status in women undergoing partial mastectomy for breast malignancy," Am Surg **71**, 22-27; discussion 27-28 (2005).

8.   N. Cabioglu, K. K. Hunt, A. A. Sahin, H. M. Kuerer, G. V. Babiera, S. E. Singletary, G. J. Whitman, M. I. Ross, F. C. Ames, B. W. Feig, T. A. Buchholz, and F. Meric-Bernstam, "Role for intraoperative margin assessment in patients undergoing breast-conserving surgery," Ann Surg Oncol **14**, 1458-1471 (2007).

9.   V. S. Klimberg, S. Harms, and S. Korourian, "Assessing margin status," Surg Oncol **8**, 77-84 (1999).

10.   R. R. Alfano, G. C. Tang, A. Pradhan, W. Lam, D. S. J. Choy, and E. Opher, "Fluorescence-Spectra from Cancerous and Normal Human-Breast and Lung Tissues," Ieee Journal of Quantum Electronics **23**, 1806-1811 (1987).

11.   R. R. Alfano, A. Pradhan, G. C. Tang, and S. J. Wahl, "Optical Spectroscopic Diagnosis of Cancer and Normal Breast Tissues," J. Opt. Soc. Amer. B (Opt Phys) **6**, 1015-1023 (1989).

12.   Y. Yang, A. Katz, E. J. Celmer, M. Zurawska-Szczepaniak, and R. R. Alfano, "Fundamental differences of excitation spectrum between malignant and benign breast tissues," Photochem Photobiol **66**, 518-522 (1997).

13.   Y. Yang, E. J. Celmer, M. Zurawska-Szczepaniak, and R. R. Alfano, "Excitation spectrum of malignant and benign breast tissues: a potential optical biopsy approach," Lasers Life Sci **7**, 249-265 (1997).

14.   P. K. Gupta, S. K. Majumder, and A. Uppal, "Breast cancer diagnosis using N2 laser excited autofluorescence spectroscopy," Lasers Surg Med **21**, 417-422 (1997).

15.   S. K. Majumder, P. K. Gupta, B. Jain, and A. Uppal, "UV excited autofluorescence spectroscopy of human breast tissues for discriminating cancerous tissue from benign tumor and normal tissue," Lasers Life Sci **8**, 249-264 (1998).

16.   A. H. Gharekhan, S. Arora, K. B. K. Mayya, P. K. Panigrahi, M. B. Sureshkumar, and A. Pradhan, "Characterizing breast cancer tissues through the spectral correlation properties of polarized fluorescence," Journal of Biomedical Optics **13**, 054063-054068 (2008).

17.   A. Alimova, A. Katz, V. Sriramoju, Y. Budansky, A. A. Bykov, R. Zeylikovich, and R. R. Alfano, "Hybrid phosphorescence and fluorescence native spectroscopy for breast cancer detection," Journal of Biomedical Optics **12**, 014004-014006 (2007).

18.   Y. Yang, E. J. Celmer, J. A. Koutcher, and R. R. Alfano, "DNA and protein changes caused by disease in human breast tissues probed by the Kubelka-Munk spectral functional," Photochem Photobiol **75**, 627-632 (2002).

19.	Y. Yang, E. J. Celmer, J. A. Koutcher, and R. R. Alfano, "UV reflectance spectroscopy probes DNA and protein changes in human breast tissues," J Clin Laser Med Surg **19**, 35-39 (2001).

20.	Y. Yang, A. Katz, E. J. Celmer, M. Zurawska-Szczepaniak, and R. R. Alfano, "Optical spectroscopy of benign and malignant breast tissues," Lasers Life Sci **7**, 115-127 (1996).

21.	M. S. Nair, N. Ghosh, N. S. Raju, and A. Pradhan, "Determination of optical parameters of human breast tissue from spatially resolved fluorescence: a diffusion theory model," Appl Opt **41**, 4024-4035 (2002).

22.	N. Ghosh, S. K. Mohanty, S. K. Majumder, and P. K. Gupta, "Measurement of optical transport properties of normal and malignant human breast tissue," Applied Optics **40**, 176-184 (2001).

23.	T. M. Breslin, F. Xu, G. M. Palmer, C. Zhu, K. W. Gilchrist, and N. Ramanujam, "Autofluorescence and diffuse reflectance properties of malignant and benign breast tissues," Ann Surg Oncol **11**, 65-70 (2004).

24.	G. M. Palmer, C. Zhu, T. M. Breslin, F. Xu, K. W. Gilchrist, and N. Ramanujam, "Comparison of multiexcitation fluorescence and diffuse reflectance spectroscopy for the diagnosis of breast cancer (March 2003)," IEEE Trans Biomed Eng **50**, 1233-1242 (2003).

25.	C. Zhu, G. M. Palmer, T. M. Breslin, F. Xu, and N. Ramanujam, "Use of a multiseparation fiber optic probe for the optical diagnosis of breast cancer," J Biomed Opt **10**, 024032 (2005).

26.	C. Zhu, G. M. Palmer, T. M. Breslin, J. Harter, and N. Ramanujam, "Diagnosis of breast cancer using fluorescence and diffuse reflectance spectroscopy: a Monte-Carlo-model-based approach," J Biomed Opt **13**, 034015 (2008).

27.	C. Zhu, T. M. Breslin, J. Harter, and N. Ramanujam, "Model based and empirical spectral analysis for the diagnosis of breast cancer," Optics express **16**, 14961-14978 (2008).

28.	C. Zhu, G. M. Palmer, T. M. Breslin, J. Harter, and N. Ramanujam, "Diagnosis of breast cancer using diffuse reflectance spectroscopy: Comparison of a Monte Carlo versus partial least squares analysis based feature extraction technique," Lasers Surg Med **38**, 714-724 (2006).

29.	Z. Volynskaya, A. S. Haka, K. L. Bechtel, M. Fitzmaurice, R. Shenk, N. Wang, J. Nazemi, R. R. Dasari, and M. S. Feld, "Diagnosing breast cancer using diffuse reflectance spectroscopy and intrinsic fluorescence spectroscopy," Journal of Biomedical Optics **13**, 024012-024019 (2008).

30.	I. J. Bigio, S. G. Bown, G. Briggs, C. Kelley, S. Lakhani, D. Pickard, P. M. Ripley, I. G. Rose, and C. Saunders, "Diagnosis of breast cancer using elastic-scattering spectroscopy: preliminary clinical results," J Biomed Opt **5**, 221-228 (2000).

31.   S. K. Majumder, M. D. Keller, F. I. Boulos, M. C. Kelley, and A. Mahadevan-Jansen, "Comparison of autofluorescence, diffuse reflectance, and Raman spectroscopy for breast tissue discrimination," J Biomed Opt **13**, 054009 (2008).

32.   S. K. Majumder, S. Gebhart, M. D. Johnson, R. Thompson, W. C. Lin, and A. Mahadevan-Jansen, "A probability-based spectroscopic diagnostic algorithm for simultaneous discrimination of brain tumor and tumor margins from normal brain tissue," Appl Spectrosc **61**, 548-557 (2007).

33.   S. C. Gebhart, R. C. Thompson, and A. Mahadevan-Jansen, "Liquid-crystal tunable filter spectral imaging for brain tumor demarcation," Appl Opt **46**, 1896-1910 (2007).

34.   W. C. Lin, S. A. Toms, M. Johnson, E. D. Jansen, and A. Mahadevan-Jansen, "In vivo brain tumor demarcation using optical spectroscopy," Photochem Photobiol **73**, 396-402 (2001).

35.   W. C. Lin, A. Mahadevan-Jansen, M. D. Johnson, R. J. Weil, and S. A. Toms, "In vivo optical spectroscopy detects radiation damage in brain tissue," Neurosurgery **57**, 518-525; discussion 518-525 (2005).

36.   S. C. Gebhart, S. K. Majumder, and A. Mahadevan-Jansen, "Comparison of spectral variation from spectroscopy to spectral imaging," Appl Opt **46**, 1343-1360 (2007).

37.   N. Ghosh, S. K. Majumder, H. S. Patel, and P. K. Gupta, "Depth-resolved fluorescence measurement in a layered turbid medium by polarized fluorescence spectroscopy," Opt Lett **30**, 162-164 (2005).

38.   A. N. Yaroslavsky, E. V. Salomatina, V. Neel, R. Anderson, and T. Flotte, "Fluorescence polarization of tetracycline derivatives as a technique for mapping nonmelanoma skin cancers," Journal of biomedical optics **12**, 014005 (2007).

39.   D. Roblyer, R. Richards-Kortum, K. Sokolov, A. K. El-Naggar, M. D. Williams, C. Kurachi, and A. M. Gillenwater, "Multispectral optical imaging device for in vivo detection of oral neoplasia," Journal of biomedical optics **13**, 024019 (2008).

40.   M. D. Keller, S. K. Majumder, and A. Mahadevan-Jansen, "Spatially offset Raman spectroscopy of layered soft tissues," Opt Lett **34**, 926-928 (2009).

CHAPTER V

SPATIALLY OFFSET RAMAN SPECTROSCOPY OF LAYERED SOFT TISSUES

5.1 Abstract

Raman spectroscopy has been widely used for cancer diagnosis, but conventional forms provide limited depth information. Spatially offset Raman spectroscopy (SORS) can solve the depth issue, but it has only been used to detect hard tissues like bone. The feasibility of using SORS to discriminate two layers of soft tissue is explored in this letter. Measurements were taken with individual source and detector fibers at a number of spatial offsets from samples consisting of various thicknesses of normal human breast tissues overlying breast tumors. Results show that SORS can detect tumors beneath normal tissue, marking the first application of SORS for discriminating two layers of soft tissue.

5.2 Introduction

Several groups have successfully applied Raman spectroscopy for cancer diagnosis, primarily in epithelial tissues [1] because of the limited depth from which typical Raman setups can gather significant signal. The most practical and promising method for detecting signals from deeper tissues, at least 1 mm below the surface, is introducing a spatial offset between the delivery and collection fibers in a technique known as spatially offset Raman spectroscopy (SORS) [2].

In SORS, larger offsets are more likely to detect photons that have traveled deeper into tissue via multiple scattering, compared with smaller separations, which detect superficial photons that have only undergone minimal scattering events. Matousek et al. first demonstrated SORS of diffusely scattering media using a two-layer chemical phantom [2]. To date, the primary biological application of this technique has been detecting the strong Raman signature of bone through several mm of soft tissue [3-5]. It has also been used to detect the Raman spectral features of hydroxyapatite crystals (found in breast calcifications) through overlying lean chicken breast tissue [6]. Thus, the application of SORS has been limited to detecting very strong scatterers with unique spectral features under a layer of generic soft tissue. No work has, to our knowledge, yet been published in applying SORS to discriminating multiple layers of soft tissue.

One relevant application of using SORS for soft tissues would be evaluating margin status during breast conserving therapy (BCT). This process involves a lumpectomy for the removal of the primary breast lesion, usually followed by radiotherapy. To be successful, BCT must provide negative margins, meaning there is no presence of tumor in the removed tissue within 1-2 mm (depending on hospital) of the surgical margin [7]. The definitive diagnosis of margin status is provided by serial sectioning with histopathology, but results are slow, and current intraoperative techniques all have limitations in accuracy and/or time required [8].

A recent review of the use of Raman spectroscopy for breast cancer diagnosis was offered by Krishna et al. [9]. We have also conducted a recent study in which nearly 300 Raman spectra from *in vitro* breast samples were classified into four histopathological categories with 99% overall accuracy [10]. It should be noted that the vast majority of the published work is focused on diagnosis of breast cancer and not for guidance of therapy or margin assessment. Additionally, no published work considers the need for determining margin status to a depth of

73

1-2 mm on the excised specimen. Besides the general purpose of demonstrating the use of SORS in soft tissues, the goal of this study was to assess the feasibility of using SORS to detect the Raman signatures of breast tumors beneath relevant thicknesses of normal breast tissue to mimic the clinical situation of evaluating margin status.

5.3 Experimental Methods

A schematic of the experimental setup used is shown in Figure 5.1. Layers of normal human breast tissue, which consisted of mostly adipose with some fibroglandular tissue, were sealed between two ~100 μm thick quartz coverslips to prevent dehydration and to minimize the impact of non-biological materials on the results. Normal layer thicknesses of 0.5, 1, and 2 mm were achieved by placing appropriate spacers between the coverslips. These thicknesses were chosen to represent the clinical margin standards and to include a thinner layer as a positive control. These normal layers were placed directly on top of invasive breast cancer tissue
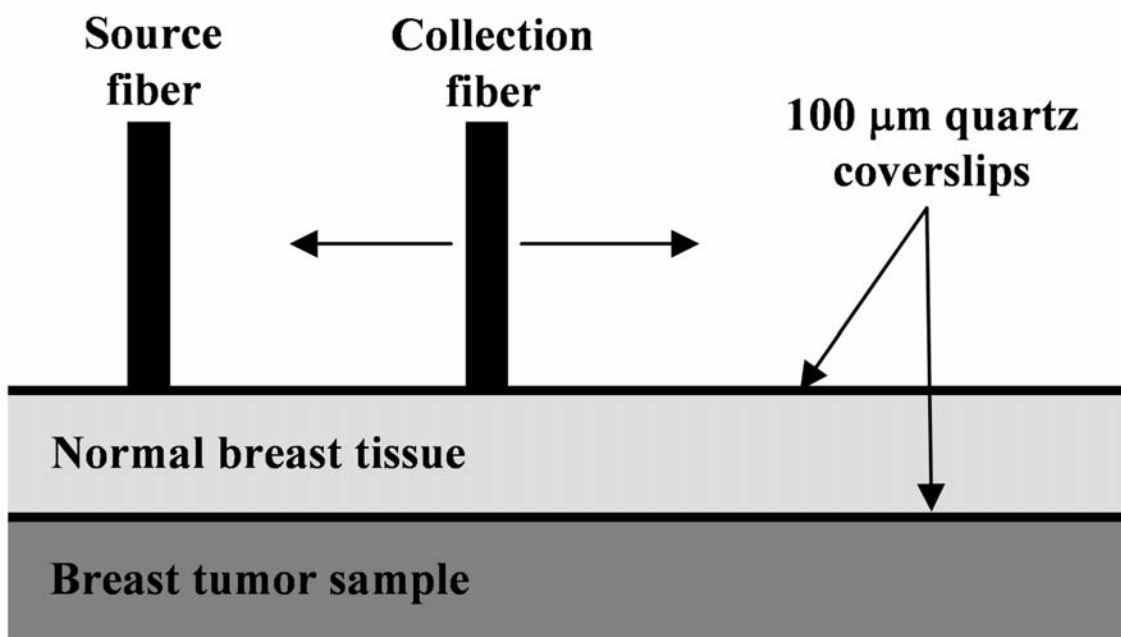
Figure 5.1. Schematic of experimental setup. Normal breast tissue thicknesses of 0.5, 1, and 2 mm were used.

samples, which ranged from ~2-5 mm thick, obtained fresh-frozen from the Cooperative Human Tissue Network and thawed at room temperature in buffered saline. In all, three tumor samples were used, while two normal tissue samples were used to create the normal layers.

SORS measurements were taken with single 200 μm excitation and collection fibers, featuring in-line bandpass and longpass filters, respectively, at their tips (Emvision, Loxahatchee, FL). The source fiber was fixed in place and delivered 80 mW of power from a 785 nm diode laser (Innovative Photonics Solutions, Monmouth Junction, NJ). The collection fiber was able to translate in a straight line and delivered light to the detection elements: an imaging spectrograph (Kaiser Optical Systems, Inc., Ann Arbor, MI) and a back illuminated, deep depletion, thermo-electrically cooled charge coupled device camera (Andor Technology, Belfast, Northern Ireland). Measurements were taken with spatial offsets from 0.75 to 4.75 mm in 0.5 mm intervals. For each offset, two 30 second integrations were acquired and averaged before further analysis. To achieve a smaller offset and as a point of comparison, spectra were also obtained with the same instrumentation but with a more standard fiber optic probe with a central 400 μm delivery fiber and seven surrounding 300 μm collection fibers, all featuring in-line filtering at their tips (Emvision). All seven fibers were binned after a single 3 second acquisition, and these measurements were considered to be taken with a 0.35 mm source-detector offset. All spectra were calibrated, noise smoothed, and had background fluorescence subtracted as previously described [11]. Normalization was achieved by dividing each processed spectrum by its overall mean intensity.

5.4 Results and Analysis

Figure 5.2 shows a sample of spectra obtained from a single experimental run with a 0.5
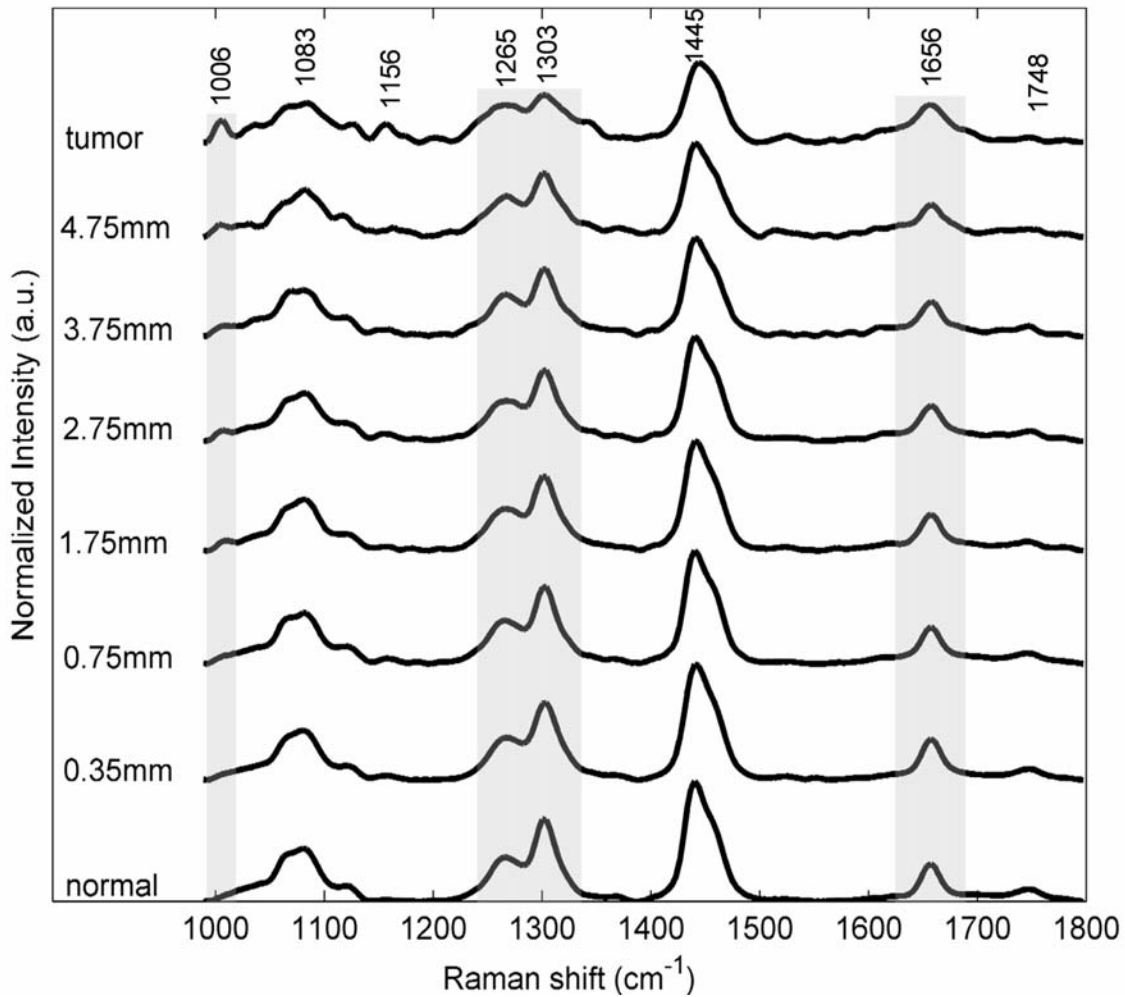
Figure 5.2. Raman spectra from an experimental run with a 0.5 mm normal layer. Gray boxes highlight regions with most dramatic changes from normal to tumor signatures as source-detector offset (labeled on left) increases.

mm normal layer over an invasive cancer tissue sample, as well as the mean spectra from the individual normal and tumor layers. From a visual inspection, it is clear that as spatial offset increases, the spectra begin to increasingly resemble the tumor spectrum compared with the normal spectrum. The light gray boxes in Figure 5.2 highlight the spectral regions subject to the most dramatic changes as spatial offset increases. These include the increased presence of the 1006 cm^{-1} peak generally attributed to phenylalanine; a decreasing ratio of the 1303 cm^{-1} to 1265 cm^{-1} peaks, which tends to indicate an increasing protein content; and the increasing width of the

76

amide I peak around 1656 cm^{-1}. Another significant change that is somewhat difficult to appreciate in Figure 5.2 is a decrease in the relative intensity of the 1445 cm^{-1} CH$_2$ deformation peak as spatial offset increases. Other subtle changes include a decrease in the 1748 cm^{-1} carbonyl stretch peak and an increase in the 1156 cm^{-1} carotenoid peak as offset increases.

The results of this study were quantified by developing a classical least squares (CLS) model via the PLS_toolbox (Eigenvector Research, Wenatchee, WA) within a MATLAB (Mathworks, Natick, MA) environment. Five Raman measurements from each normal tissue layer only were averaged together, and five measurements from each tumor sample only were averaged; these two means were then used as pure component spectral inputs to create a CLS model. This model was subsequently applied to the spectra collected from each spatial offset to determine the relative contributions of the normal and tumor spectral signatures to the offset spectra. These two relative contributions always sum to 1, and the model was constrained to fitting the data in a non-negative manner. The relative tumor contributions were then averaged across the three experimental runs for analysis.

Figures 5.3 and 5.4 show the results of the CLS analysis in complementary fashion. Both plot the relative tumor spectrum contributions to the offset spectra on the y axis, but Figure 5.3 shows how this metric changes as a function of source-detector offset for the three different normal layer thicknesses, while Figure 5.4 displays it as a function of normal layer thickness for a range of spatial offsets. Most generally, both figures quantitatively support the visual evidence from Figure 5.2 that SORS can indeed detect Raman spectral contributions from breast tumors beneath the relevant depths of normal tissue that standard configurations (0.35 mm offset) cannot. From Figure 5.3, this effect follows a quadratic- or logarithmic-shaped response as spatial offset increases, and it seems to indicate that for this tissue system, S-D offsets of more
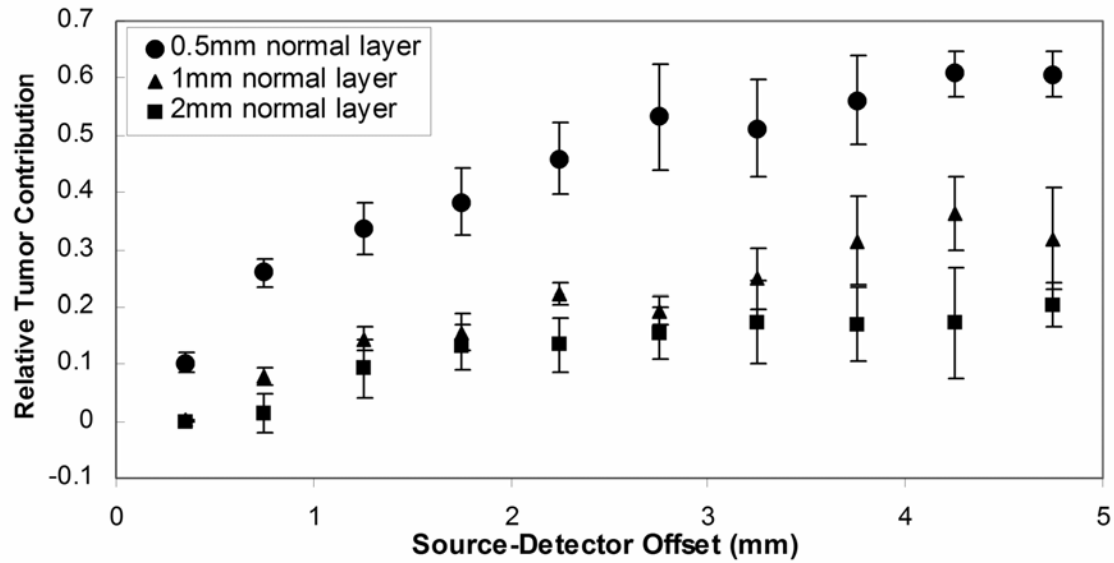
Figure 5.3. Mean relative contributions of the Raman tumor signature to the measured spectra at each source-detector offset for the various thicknesses of the normal tissue layer. Error bars represent standard error.
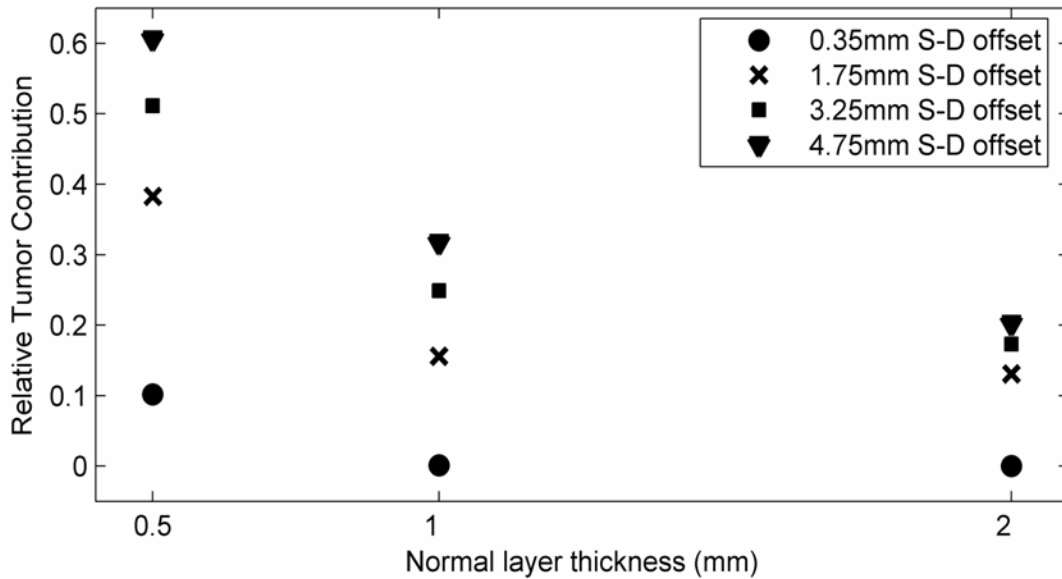
Figure 5.4. Same data from Figure 4.3, but shown as function of normal layer thickness for selected S-D separations.

than about 4 mm do not provide any additional useful information. An interesting effect is shown most explicitly in Figure 5.4, which shows that as the normal layer thickness increases, there is a tighter grouping of data points along the y axis. This trend hints at a maximum top layer

thickness that would allow detection of the bottom layer, which is likely limited by the achievable signal to noise ratio of the bottom layer and the absolute signal strength compared with the top layer.

5.5 Discussion

The findings of this letter have some key similarities to and differences from previous SORS studies. The shapes of the responses to changes in spatial offset and top layer thickness in Figures 5.3 and 5.4, respectively, match up well with similar plots in earlier studies [2, 5]. Unlike earlier reports, in which the spectrum of the bottom layer contained strong, unique bands, these trends were observed with two layers of soft tissue whose Raman spectra differ in a subtle manner. This limits, or at least severely complicates, the use of some analytical techniques used in other SORS studies. A simple, two component CLS model with a direct physical basis worked well for validating the application of SORS to soft tissues, although a more complex model or an entirely different method of analysis may be more appropriate for clinical applications.

A number of other issues will need to be addressed to move from this proof of principle experiment toward a clinical application. The variability within these measurements will need to be considered, particularly as it relates to tissue composition, since some of the "noise" in Figures 5.3 and 5.4 is likely due to tissue heterogeneities. While no obvious Raman signal from the coverslips was observed, their inclusion provided an unnatural discontinuity between tissue types. Based on previous measurements from a layered tissue model without using coverslips (unpublished), their presence did not seem to induce any spectral effects, so their ability to precisely control layer thickness outweighed other potential negatives at this stage. Given that tumors generally do not actually have planar boundaries, identifying the detection limit for

finding small pockets of cancer cells or micro-invasions becomes important. Since the smallest portion of a tumor sample used in this study was around 1-2 mm thick, it is difficult to speculate on the minimum number of tumor cells that could be detected. Based on trends in Figures 5.3 and 5.4, though, it appears likely that cancerous regions smaller than those used in this study could be detected under at least a 1 mm overlying layer. This issue of detection limits will be a focus of future research, which includes the development of suitable numerical simulations with a Monte Carlo model. While Raman tomography would also theoretically be a good tool to limit the negative effects of photon diffusion on finding small pockets, its resolution is currently too poor without the aid of spatial priors [12], which would be impractical to obtain for a BCT application.

This report has demonstrated that SORS can detect the spectral signatures of breast tumors as small as 1-2 mm thick under up to 2 mm of normal breast tissue. Although a number of questions about its efficacy require further study, this report shows that SORS of soft tissues likely holds promise for biomedical applications previously considered "out of reach" for Raman spectroscopy.

5.6 Acknowledgments

5.7 References

1.   M. D. Keller, E. M. Kanter, and A. Mahadevan-Jansen, "Raman spectroscopy for cancer diagnosis," Spectroscopy **21**, 33-41 (2006).

2.   P. Matousek, I. P. Clark, E. R. Draper, M. D. Morris, A. E. Goodship, N. Everall, M. Towrie, W. F. Finney, and A. W. Parker, "Subsurface probing in diffusely scattering media using spatially offset Raman spectroscopy," Appl Spectrosc **59**, 393-400 (2005).

3.   P. Matousek, E. R. Draper, A. E. Goodship, I. P. Clark, K. L. Ronayne, and A. W. Parker, "Noninvasive Raman spectroscopy of human tissue in vivo," Appl Spectrosc **60**, 758-763 (2006).

4.   M. V. Schulmerich, K. A. Dooley, M. D. Morris, T. M. Vanasse, and S. A. Goldstein, "Transcutaneous fiber optic Raman spectroscopy of bone using annular illumination and a circular array of collection fibers," J Biomed Opt **11**, 060502 (2006).

5.   N. A. Macleod, A. Goodship, A. W. Parker, and P. Matousek, "Prediction of sublayer depth in turbid media using spatially offset Raman spectroscopy," Analytical chemistry **80**, 8146-8152 (2008).

6.   N. Stone, R. Baker, K. Rogers, A. W. Parker, and P. Matousek, "Subsurface probing of calcifications with spatially offset Raman spectroscopy (SORS): future possibilities for the diagnosis of breast cancer," Analyst **132**, 899-905 (2007).

7.   K. C. Horst, M. C. Smitt, D. R. Goffinet, and R. W. Carlson, "Predictors of local recurrence after breast-conservation therapy," Clin Breast Cancer **5**, 425-438 (2005).

8.   N. Cabioglu, K. K. Hunt, A. A. Sahin, H. M. Kuerer, G. V. Babiera, S. E. Singletary, G. J. Whitman, M. I. Ross, F. C. Ames, B. W. Feig, T. A. Buchholz, and F. Meric-Bernstam, "Role for intraoperative margin assessment in patients undergoing breast-conserving surgery," Ann Surg Oncol **14**, 1458-1471 (2007).

9.   C. M. Krishna, J. Kurien, S. Mathew, L. Rao, K. Maheedhar, K. K. Kumar, and M. Chowdary, "Raman spectroscopy of breast tissues," Expert Rev Mol Diagn **8**, 149-166 (2008).

10.   S. K. Majumder, M. D. Keller, M. C. Kelley, F. I. Boulos, and A. Mahadevan-Jansen, "Comparison of autofluorescence, diffuse reflectance, and Raman spectroscopy for breast tissue discrimination.," J Biomed Optics **13**, 054009 (2008).

11.   C. A. Lieber, and A. Mahadevan-Jansen, "Automated method for subtraction of fluorescence from biological Raman spectra," Appl Spectrosc **57**, 1363-1367 (2003).

12.   S. Srinivasan, M. Schulmerich, J. H. Cole, K. A. Dooley, J. M. Kreider, B. W. Pogue, M. D. Morris, and S. A. Goldstein, "Image-guided Raman spectroscopic recovery of canine cortical bone contrast in situ," Optics express **16**, 12190-12200 (2008).

CHAPTER VI

NUMERICAL SIMULATIONS OF SPATIALLY OFFSET RAMAN SPECTROSCOPY FOR

BREAST TUMOR MARGIN ANALYSIS

6.1 Abstract

We previously demonstrated the discrimination of two layers of soft tissue, specifically normal breast tissue overlying breast tumor, using spatially offset Raman spectroscopy (SORS). In this report, a Monte Carlo code for performing SORS in soft tissues has been developed and validated by comparing it to experimental results. The model was then used to examine the effects on detected SORS signals of variables like normal and tumor layer size and overall tissue geometry, which are difficult to precisely control experimentally and could influence the use of SORS in breast tumor surgical margin evaluation.

6.2 Introduction

Spatially offset Raman spectroscopy (SORS) has been shown to be an effective tool in recovering Raman spectra from up to several millimeters beneath the surface of turbid media [1-11]. The enhanced depth information obtained from SORS, compared to standard Raman techniques, results from photons being multiply scattered and traveling further beneath the surface before exiting the medium at larger source-detector (S-D) offsets. After initial demonstrations on layered chemical samples [7, 9, 10], this technique has been applied to several biological systems as well. The most extensive biological work has been detecting Raman spectra from bone under several millimeters of soft tissue [1, 3, 4, 6, 8]. Other work has been

aimed at finding calcifications in breast tissues [3, 5].

In both of the above biological applications, the detection target was hard tissue with strong Raman bands not present in soft tissue – e.g. the phosphate stretch at ~960 cm^{-1}. Detecting the presence of one type of soft tissue below a different type is more challenging because the Raman spectra of the two layers will typically have all of the same general peaks present; discrimination relies on more subtle differences such as peak widths and relative ratios. In a previous study at Vanderbilt, we demonstrated the ability of SORS to detect breast cancer tissue under up to 2 millimeters of normal breast tissue [2]. This was accomplished by developing a classical least squares (CLS) model with the layers' pure component spectra as inputs. The CLS model was then applied to spectra taken at various spatial offsets from a layered tissue construct to determine the relative spectral contributions of the two layers. While this study effectively showed the feasibility of using SORS on layered soft tissues, it also raised questions about the limits of such an approach, particularly for evaluating margin status following breast conserving surgery (BCS).

Around 180,000 new breast cancer patients each year are eligible for BCS [12], in which the primary tumor is removed along with a surrounding margin of at least 1-2 mm of normal tissue. When the normal tissue margin is of insufficient size (i.e. the margin is "positive"), the patient's risk of recurrence significantly increases, and a second operation becomes necessary [13, 14]. The exact definition of a positive margin varies by institution [15], but reports show the lowest recurrence rates when a cutoff value of 2 mm is used [13]. Since current methods of intraoperative margin analysis are limited in terms of accuracy and/or time required [16-19], using SORS for this application could fill a major medical need. From the earlier feasibility study [2], it appears that SORS would be a good candidate for such a role; however, a major

issue to be addressed is the detection limit of this technique, in terms of the size of both the overlying normal layer and the tumor.

Since it is very difficult and largely impractical to precisely control tissue thicknesses and geometries in intact specimens, a Monte Carlo simulation model was sought to investigate the issue of detection limits. Since a more detailed approach than previously reported Monte Carlo models for Raman scattering [20-23] was desired, the first goal of this study was to adapt the multi-layer fluorescence Monte Carlo code of Vishwanath et. al. into a true Raman Monte Carlo model. The model was validated by comparing results to earlier experiments [2] and was then used to examine the effects on relative spectral contributions from each layer in models with normal human breast tissue overlying breast tumors. Models were constructed to examine a variety of factors, including the presence of quartz coverslips in the original experimental data, thicknesses of both the normal and tumor layers, and the presence of an additional normal layer underneath the tumor.

6.3 Materials and Methods

6.3.1 Raman Monte Carlo model

The Raman Monte Carlo model utilized in this report was developed by modifying the previously-existing multi-layer, multi-fluorophore Monte Carlo code of Vishwanath et al. [24]. In the fluorescence code, all photons are launched into the medium in accordance with the radius and numerical aperture of the source fiber, with an initial weight equal to 1; a given photon is then scattered through the medium until it exits the tissue or its weight falls below some pre-defined threshold (via absorption). The length of each scattering step of a photon in layer i of the tissue is determined from sampling a probability distribution dependent on the tissue total

attenuation coefficient $\mu_{st,}$ which is the sum of the tissue scattering coefficient μ_{si} and absorption coefficient μ_{ai} in the ith tissue layer. At each step of the photon's path, a new scattering angle is calculated by sampling the Henyey-Greenstein phase function based on the layer's scattering anisotropy g. At any point on its path, a photon can be absorbed by a fluorophore; the probability of this effect is determined by sampling a probability distribution function that is dependent on the fluorophore absorption coefficient μ_{afx} in the ith tissue layer. Photons that have been absorbed by a fluorophore will then be re-emitted at the emission wavelength, after some time delay τ, determined by sampling a probability distribution for the mean time spent by the fluorophore in the excited state. The efficiency of the re-emission of fluorescence photons is determined by the fluorophore quantum yield Φ_{QY}. If the weight of a photon falls below the threshold value, a roulette routine is performed to determine whether the photon will survive; if the photon does not survive the roulette, it is terminated via absorption into the tissue. When a photon exits the tissue, it is "detected" if the radial distance between its entry and exit positions is within one of the pre-defined "detector" bins and its angle of exit is within the acceptance cone defined by the numerical aperture of the detector fibers.

In order to accommodate Raman scattering, the fluorophore absorption coefficient μ_{afxi} and fluorescence quantum yield Φ_{QY} in tissue layer i were effectively merged into a single quantity R_x indicative of the Raman cross section (i.e. how likely it is that an excitation photon will undergo Raman scattering) for a given layer. Once a photon had been Raman scattered, any subsequent Raman scattering by that photon was neglected since even a single Raman event is a relatively rare occurrence. In addition, the mean time delay τ between fluorescence excitation and emission was set to zero to indicate that Raman scattering could be approximated as instantaneous. The initial angle of a Raman scattering event was considered an isotropic process.

While other Raman Monte Carlo reports [20-23] use this assumption as well, we could not find any experimental validation of this property for biological tissues. To that end, goniometric-like measurements were done first on a cylindrical cuvette of cyclohexane in the style of Passos et al. [25], and then on a 100 μm thick layer of chicken fat in the style of Arnfield et al. [26]; in both cases, Raman signal was detected rather than elastic scattering like in the references. These experiments (results not displayed in this report) confirmed the assumption that Raman scattering is an isotropic process.

The wavelength associated with the Raman scattered photons was chosen to be 884 nm. This wavelength falls almost exactly in the middle of the wavelength range corresponding to the relative wavenumber range used experimentally of 990 cm^{-1} (~851 nm) to 1800 cm^{-1} (~914 nm). Optical properties for normal breast and breast tumors are also available for this wavelength in the literature [27]. A single Raman wavelength was chosen because for wavelengths around this value, the tissue absorption is essentially negligible and the scattering is nearly constant [27-29].

The modified Monte Carlo code also included sections that accounted for the presence of clear layers that had no absorption or scattering but did have a different refractive index than the surrounding tissue layers. This modification was important since the experimental studies [2] included quartz coverslips between the tissue layers. To simulate the zero-scattering nature of the coverslips, the code was modified to immediately move any photon that had just entered a clear layer to the opposite edge of that layer. Therefore, the next step of any photon that had entered a clear layer would take that photon across the boundary of the clear layer, unless the photon was reflected at the boundary, in which case the reflected photon would be immediately transported to the opposite edge of the clear layer once again, and the aforementioned process would be repeated. Also, since the experimental tissue constructs had coverslips on top of the upper tissue

layer [2], the code was modified so that all photons began at the bottom edge of this first coverslip, to simulate the effect of the coverslip having no significant scattering properties.

6.3.2 Optical Properties

Values for the reduced scattering coefficient ($\mu_s' = \mu_s[1-g]$) and absorption coefficient for both excitation photons at 785 nm and Raman photons at 884 nm were taken from a study by Grosenick et. al. [27]. These values were also confirmed experimentally at 785 nm for a small sample set using a double integrating sphere and the inverse adding-doubling method [30]. Anisotropy values for elastic scattering were held constant at both wavelengths and were taken from a report by Ghosh et. al. [31]. Relative Raman cross sections were computed by comparing the total area under the curve from non-normalized Raman spectra of optically thick samples of normal breast and breast cancer tissues obtained in identical fashions. The above values are shown in Table 6.1. While no systematic analysis of the sensitivity of the model to changes in input optical properties was performed, it was observed that modifying the input values produced appropriately sized differences in the outputs. In particular, holding μ_s' constant while changing μ_s and g within an order of magnitude in either direction had essentially no impact on the output of the simulations (data not shown).

Table 6.1. Summary of optical properties for normal and tumor tissues at excitation (785 nm) and Raman (884 nm) wavelengths. μ_a – absorption coefficient, μ_s' – reduced scattering coefficient, g – elastic scattering anisotropy, R_x – relative Raman cross section

Parameter	Normal @ 785nm	Tumor @ 785nm	Normal @ 884nm	Tumor @ 884nm
μ_a (cm^{-1})	0.039	0.100	0.059	0.124
μ_s' (cm^{-1})	9.5	11.6	8.0	9.1
g	0.88	0.96	0.88	0.96
R_x	4	1	N/A	N/A

6.3.3 Simulation Details

Simulations whose results are shown in Figures 6.2 and 6.3 were run with 10^8 initial photons, and other simulations were run with 5×10^7 initial photons. The excitation region and detector bins were set up to match the size (200 μm diameter), placement, and numerical aperture (0.22) of the optical fibers used in the experimental data. Results were quantified by determining the fraction of detected Raman photons in each bin that originated in the tumor layer. This measure was equivalent to the "relative tumor contribution" metric derived from experimental data [2]. Unless otherwise specified, the thickness of the tumor layer was set to 5 mm to correspond to the approximate thicknesses of the experimental samples. For simulations with an additional normal layer under the tumor, the thickness of the normal layer was set to 2 cm to be considered semi-infinite.
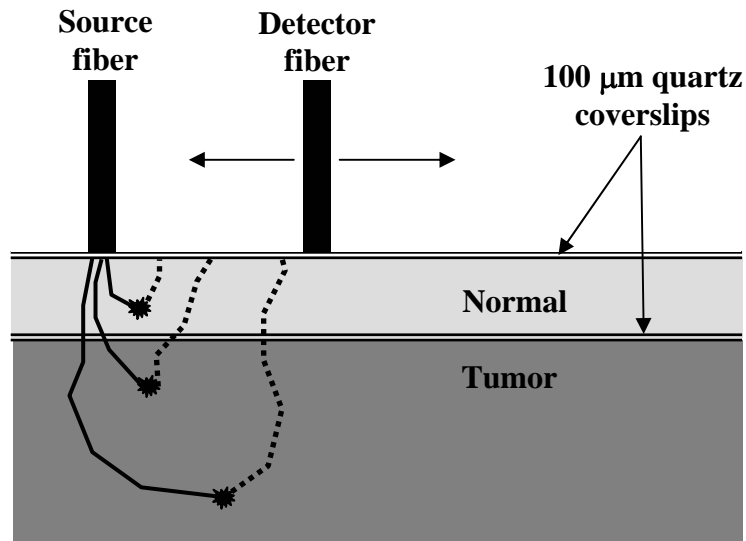
Figure 6.1 Experimental setup from previous report [2], along with sample Monte Carlo photon paths. Solid lines represent excitation photons, dotted lines represent Raman scattered photons. Raman scattering events represented by ✳.

6.3.4 Experimental Data

Figure 6.1 shows the experimental setup used in the earlier report [2], with the addition of sample paths from the source fiber to various spatial offsets taken by photons in the Monte Carlo simulations. The experimental data from Figure 6.2 is from that earlier report [2], with the exception of the 2 mm normal layer data. It was determined that experimental conditions for the original 2 mm data set may not have been optimally controlled. In addition, the residuals for the CLS fit of the original 2 mm data were several times higher than for the other top layer thicknesses. A new set of measurements from a 2 mm normal layer over three invasive breast cancer samples was therefore obtained in an identical manner to the earlier report [2].

6.4 Results

Figure 6.2 displays both the experimental and Monte Carlo results for relative tumor contribution versus source-detector offset for the constructs with normal breast tissue over breast tumors, including the presence of quartz coverslips as shown in Figure 6.1. Top normal layers of 0.5, 1, and 2 mm were used. Simulations used the optical properties from Table 6.1 and included the presence of the 100 μm thick quartz coverslips above and below the normal layer in experimental measurements. While it is difficult to quantify the fit between the experimental and modeling results due to the "noise" present in the experimental data, overall the data match quite well. The poorest fit in terms of S-D offset is for the 0.42 mm data point, which was taken experimentally with a 7-around-1 fiber probe rather than with individual source and collection fibers. The remainder of the 0.5 mm layer simulation data falls within the experimental error bars, and the 1 mm layer simulation captures the experimental trend very well. For the 2 mm layer data, the simulation and experiment line up well past the 1.75 mm S-D offset point. For
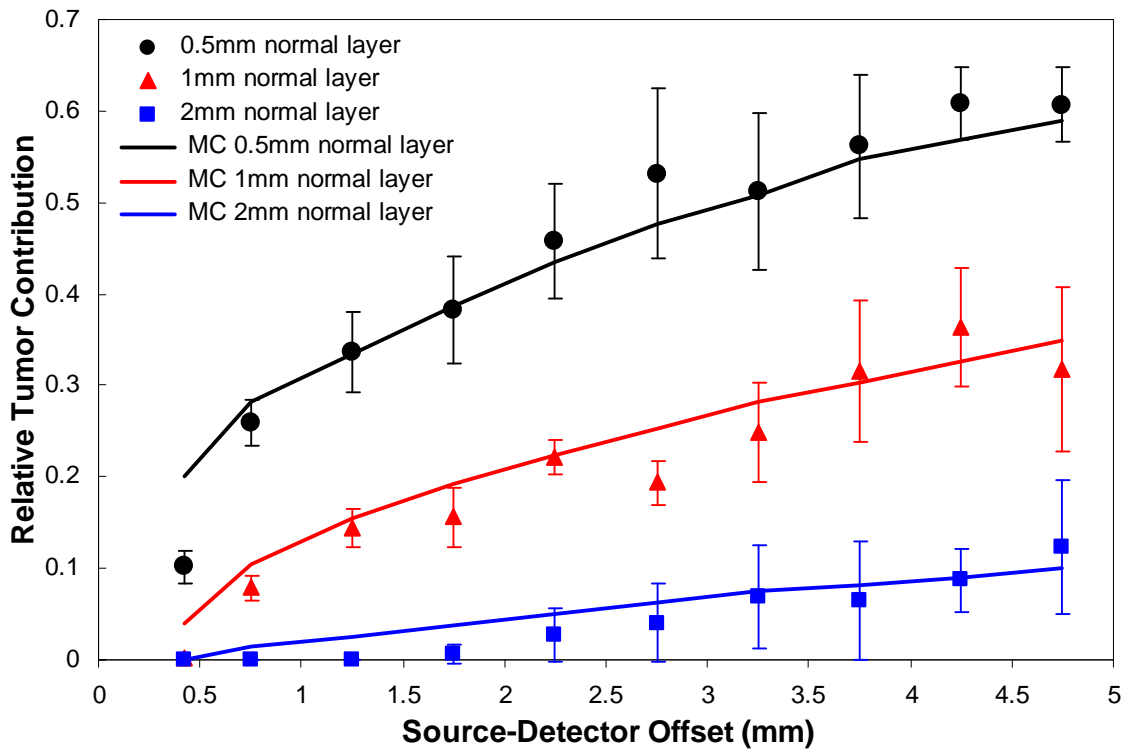
Figure 6.2 Experimental versus Monte Carlo results for relative tumor contributions from normal breast tissue layers 0.5, 1, and 2 mm thick, overlying breast tumors.

smaller S-D offsets, the experiments had trouble finding any tumor contribution, although the simulations indicated that there should be very small tumor spectral contributions for S-D offsets greater than 0.75 mm. Given the overall good fit between lab measurements and simulations, the Monte Carlo model was considered validated and was used to investigate the effects of changing various tissue construct parameters.

Figure 6.3A displays only the simulated relative tumor contributions from Figure 6.2, while Figure 6.3B displays the simulated results from identical models but without the presence of quartz coverslips and without the 0.42 mm offset since that point had been obtained with a different sampling geometry. The responses in Figure 6.3B are very similar to the ones in Figure 6.3A, but they show slightly stronger relative tumor contributions. These differences range from
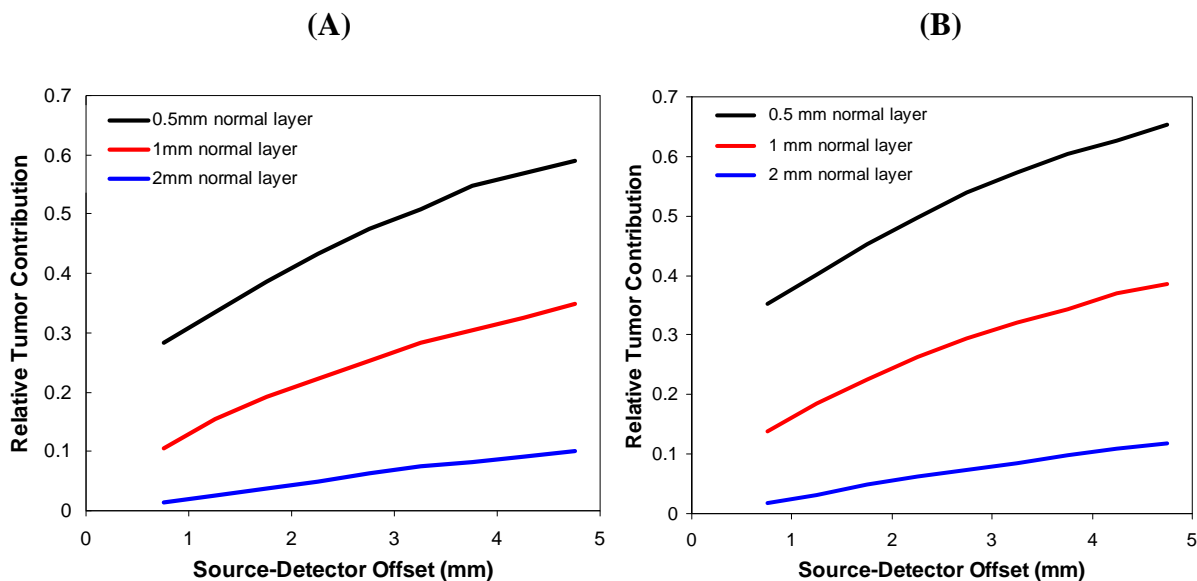
Figure 6.3 Simulated relative tumor contributions from layered tissue constructs with normal breast tissue layers of 0.5, 1, and 2 mm overlying breast tumors. (A) Constructs with coverslips included as above, and (B) constructs without the presence of coverslips.

~20-25 % at the smallest S-D offsets to ~10% at the largest S-D offsets. From this result, it appears that the inclusion of quartz coverslips in the original experiment did not drastically alter the relative tumor contributions; the primary effect was shifting the curves slightly downward on the y-axis.

The effect of changing the tumor thickness from the standard 5 mm used in the above simulations is shown in Figures 6.4A-D, for increasingly thick top normal layers. The tumor thicknesses ranged from an approximately semi-infinite (relative to penetration depth of NIR light) size of 2 cm down to 100 μm, about the size of a few cells. In general, it is apparent that relative tumor contributions do not start to show significant decreases from the semi-infinite state until thicknesses less than about 3 mm. Beyond that range, decreasing tumor thickness causes a sharp drop in how much tumor spectral signature can be detected at a given S-D offset. For the smaller tumor thicknesses, the response curves are flatter compared with Figures 6.2 and 6.3, and
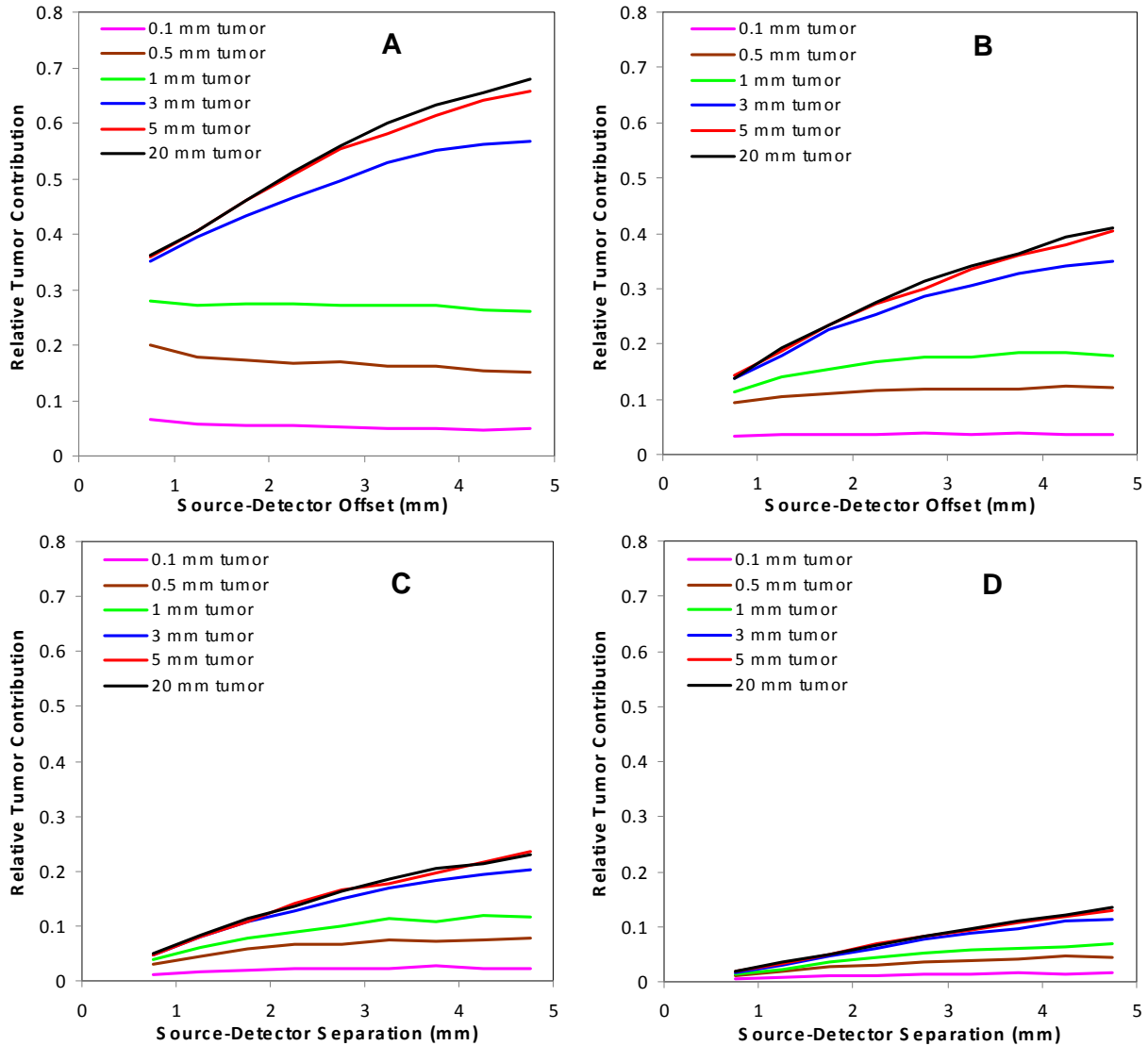
Figure 6.4 Simulated relative tumor contributions for various tumor layer thicknesses under (A) 0.5 mm, (B) 1 mm, (C) 1.5 mm, and (D) 2 mm normal layers

it also appears that the sub-millimeter thicknesses cannot be detected very well under a 2 mm normal layer. The result from the largest spatial offsets for the 0.1 mm tumor in Figure 6.4A is somewhat noisy, presumably due to the high percentage of excitation photons that were transmitted through the two very thin layers.

The results shown in Figure 6.5 are from simulations identical to those in Figure 6.4, but with the addition of a 2 cm normal breast tissue layer underneath the tumor to simulate
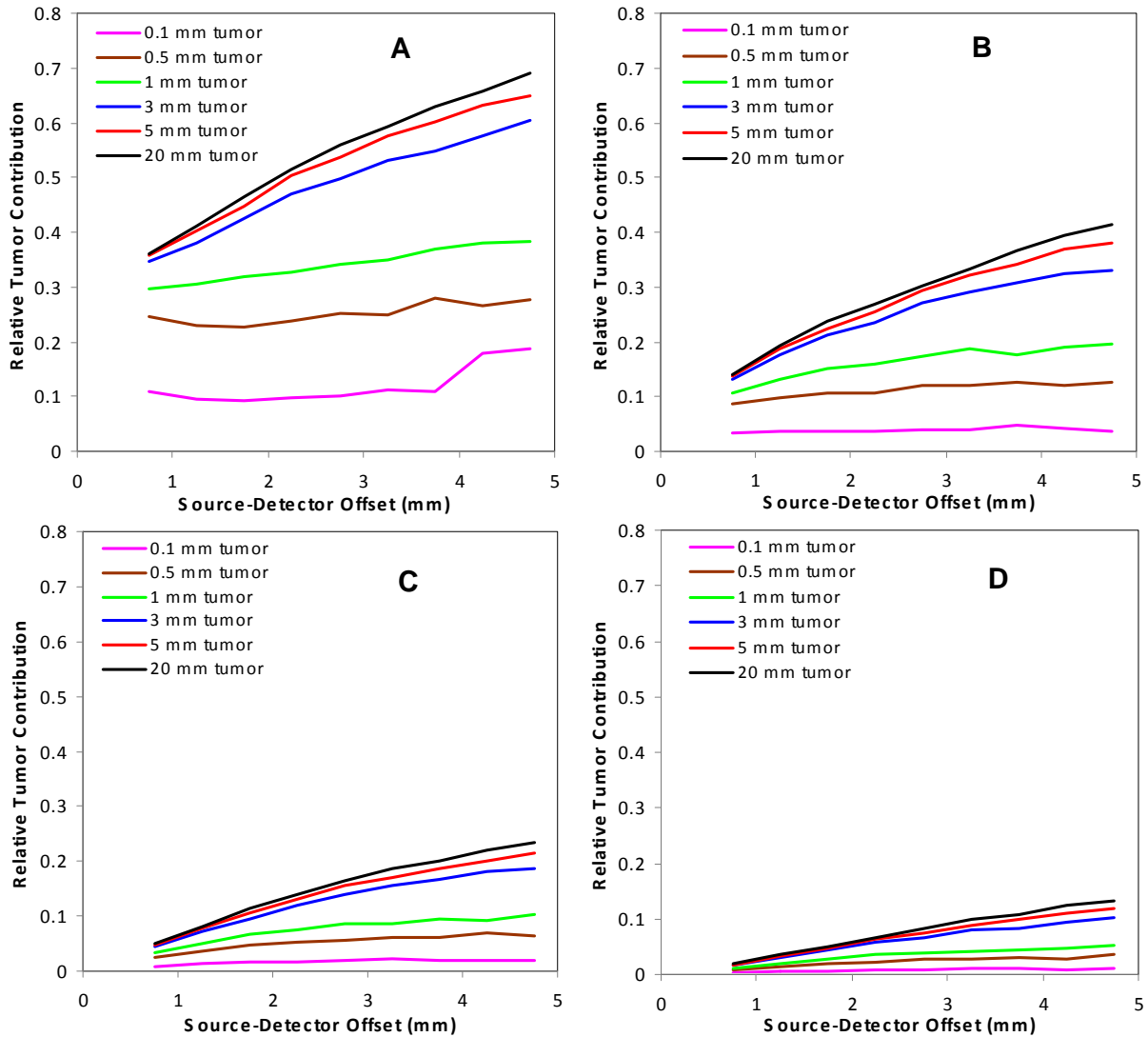
Figure 6.5 Simulated relative tumor contributions for various tumor layer thicknesses under (A) 0.5 mm, (B) 1 mm, (C) 1.5 mm, and (D) 2 mm normal layers, with an additional 20 mm normal layer underneath the tumor.

conditions more likely seen in a clinical sample. For the two thickest tumor layers, little to no difference is seen between corresponding portions of Figures 6.4 and 6.5, since not very many photons would enter the lower normal layer through the thick tumors. The same can be said for the thicker top normal layers in parts C and D of the figures. As normal and tumor thicknesses decrease, more differences become evident between the two figures. Most generally, response

curves in Figure 6.5A-B are shifted down somewhat as tumor volume remains the same, but now normal Raman photons can be generated below the tumor as well. In addition, relative tumor contributions of the 1 mm and 0.5 mm curves in Figure 6.5A are essentially flat, indicating that photons entering any detector bin have passed through about the same volume of tumor tissue.

6.5 Discussion

The initial goal of this study was to develop and validate a Monte Carlo model to accurately reflect experimental SORS results. As seen in Figure 6.2, the simulations were able to replicate the experimental data very well. While the simulation results did not hit every experimental data point, this was expected given the "noise" seen in the latter points. The smooth simulation lines do follow the trends of the experimental data, with two primary exceptions. The model predicted greater relative tumor contributions from the 0.42 mm spatial offset data point, which was taken with an optical fiber probe featuring a central 400 μm excitation fiber and seven surrounding 300 μm collection fibers, rather than with single 200 μm diameter excitation and collection fibers. The model was changed to reflect this different geometry as well. The most likely cause for the data disagreement is that the probe's geometry at its tip somehow differed from its ideal construction, which is difficult to achieve in practice. For this reason, only S-D offsets from the individual fibers were considered in later simulations.

The other region of Figure 6.2 with model-experiment mismatch was for the smaller spatial offset measurements with a 2 mm top normal layer. While the model predicted very small tumor contributions to the measured spectra ($<= \sim 5\%$), no such contributions could be detected in the experimental data. It is likely, then, that these values for the 'relative tumor contribution' metric represent the approximate detection limit in practice, as such small spectral

contributions would be about equivalent in strength to noise levels. Applying this finding to simulations without coverslips in Figure 6.4, it appears possible to experimentally detect a very small (100 μm) layer of tumor cells under 0.5 mm of normal breast tissue, while under 1 mm of normal tissue, the limit seems to increase to a value between 100 and 500 μm. For the thickest top normal layer of 2 mm, Figure 6.4D indicates that it would be difficult to detect a tumor smaller than about 1 mm thick. The plots in Figure 6.5, from simulations with an additional layer of normal tissue on the bottom, show similar detection limits.

The effects seen in this report have a number of implications for using SORS for breast surgical margin analysis. From the detection limits discussion, it is likely possible to experimentally detect a positive margin up to 2 mm below the surface, but not if the tumor is < 1 mm thick in that region. For thinner normal layers, though, SORS appears capable of detecting a tumor layer only a few cells thick. Another conclusion is that it would be very difficult to determine the exact depth of normal tissue over a tumor, given how sensitive the 'relative tumor contribution' metric is to a number of factors. For example, by comparing Figures 6.2 and 6.3, the inclusion of 100 μm thick, clear coverslips above and below the normal layer was enough to change the y-axis response by about 10-25 % for given S-D offsets. Such a change is expected, though, since these clear layers give the photons more of an opportunity to travel further, both in depth and radially, without being scattered or absorbed in those layers.

The larger confounding factor in determining exact margin size is evident in Figures 6.4 and 6.5; namely, the effect of tumor layer thickness. For the same normal tissue layer, the observed relative tumor contribution differed by up to a factor of ~7 based on size of the tumor. In addition, the presence of normal tissue beneath the tumor can change the shape of the signal; in some cases in Figure 6.5, the response is even flat. This occurs because all of the photons

being Raman scattered into any detector pass through the same volume of tumor regardless of how deep their banana-shaped curves of photon propagation enter into the lower normal layer. With all of these confounding factors, it therefore seems unfeasible to use SORS to determine an exact negative margin size unless significant *a priori* information is available about the tissue geometry; in such a case, though, further information from SORS would likely not be needed.

Based on these results, a more viable approach for using SORS to evaluate excised breast specimen surgical margins would be simply to look for any evidence of abnormal spectral signatures from detector channels that are known to sample to the desired depth. From Figures 6.3 and 6.4, limiting the spatial offsets to 3.5 mm or less would effectively suppress any spectral contributions from tumors > 2 mm below the surface of normal tissue, while still being able to interrogate up to 2 mm beneath the surface. At spatial offsets larger than this, achieving adequate signal-to-noise ratios can be difficult as well. Future experimental work will be focused on designing and testing a multi-separation probe capable of effective sampling from the surface down to the clinically relevant depth of 2 mm in normal breast tissue.

This version of the SORS Monte Carlo code has been validated and was able to provide some useful results, but its primary shortcoming is that tissues had to be represented as homogeneous layers. In real situations, breast tumors do not have planar boundaries with layers of normal tissue. Modeling a thin layer of tumor between two layers of normal tissue is a reasonable first step in investigating the detection of small tumor "projections," but it remains to be seen what would happen if such a projection ran in the direction parallel to the fiber optics rather than perpendicular. To this end, work is underway on a SORS simulation code capable of creating irregularly shaped layers to examine their effect on tumor detection limits. Ultimately, this work is expected to provide major insights into the use of SORS for evaluating margin status

after partial mastectomies. The Monte Carlo code developed here could easily be adapted to examine other layered tissues as well, provided information about their optical properties and relative Raman cross sections are known.

6.6 Acknowledgments

6.7 References

1.   M. V. Schulmerich, J. H. Cole, J. M. Kreider, F. Esmonde-White, K. A. Dooley, S. A. Goldstein, and M. D. Morris, "Transcutaneous Raman Spectroscopy of Murine Bone In Vivo," Appl. Spectrosc. **63**, 286-295 (2009).

2.   M. D. Keller, S. K. Majumder, and A. Mahadevan-Jansen, "Spatially offset Raman spectroscopy of layered soft tissues," Opt Lett **34**, 926-928 (2009).

3.   N. A. Macleod, and P. Matousek, "Deep noninvasive Raman spectroscopy of turbid media," Appl Spectrosc **62**, 291A-304A (2008).

4.   N. A. Macleod, A. Goodship, A. W. Parker, and P. Matousek, "Prediction of sublayer depth in turbid media using spatially offset Raman spectroscopy," Analytical chemistry **80**, 8146-8152 (2008).

5.   N. Stone, R. Baker, K. Rogers, A. W. Parker, and P. Matousek, "Subsurface probing of calcifications with spatially offset Raman spectroscopy (SORS): future possibilities for the diagnosis of breast cancer," Analyst **132**, 899-905 (2007).

6.   M. V. Schulmerich, K. A. Dooley, T. M. Vanasse, S. A. Goldstein, and M. D. Morris, "Subsurface and transcutaneous Raman spectroscopy and mapping using concentric illumination rings and collection with a circular fiber-optic array," Appl Spectrosc **61**, 671-678 (2007).

7.	M. V. Schulmerich, W. F. Finney, R. A. Fredricks, and M. D. Morris, "Subsurface Raman spectroscopy and mapping using a globally illuminated non-confocal fiber-optic array probe in the presence of Raman photon migration," Appl Spectrosc **60**, 109-114 (2006).

8.	M. V. Schulmerich, K. A. Dooley, M. D. Morris, T. M. Vanasse, and S. A. Goldstein, "Transcutaneous fiber optic Raman spectroscopy of bone using annular illumination and a circular array of collection fibers," J Biomed Opt **11**, 060502 (2006).

9.	P. Matousek, "Inverse spatially offset Raman spectroscopy for deep noninvasive probing of turbid media," Appl Spectrosc **60**, 1341-1347 (2006).

10.	P. Matousek, I. P. Clark, E. R. Draper, M. D. Morris, A. E. Goodship, N. Everall, M. Towrie, W. F. Finney, and A. W. Parker, "Subsurface probing in diffusely scattering media using spatially offset Raman spectroscopy," Appl Spectrosc **59**, 393-400 (2005).

11.	P. Matousek, E. R. Draper, A. E. Goodship, I. P. Clark, K. L. Ronayne, and A. W. Parker, "Noninvasive Raman spectroscopy of human tissue in vivo," Appl Spectrosc **60**, 758-763 (2006).

12.	American Cancer Society, "Cancer Facts and Figures 2009," (American Cancer Society, Atlanta, 2009).

13.	C. Dunne, J. P. Burke, M. Morrow, and M. R. Kell, "Effect of margin status on local recurrence after breast conservation and radiation therapy for ductal carcinoma in situ," J Clin Oncol **27**, 1615-1620 (2009).

14.	K. C. Horst, M. C. Smitt, D. R. Goffinet, and R. W. Carlson, "Predictors of local recurrence after breast-conservation therapy," Clin Breast Cancer **5**, 425-438 (2005).

15.	A. Taghian, M. Mohiuddin, R. Jagsi, S. Goldberg, E. Ceilley, and S. Powell, "Current perceptions regarding surgical margin status after breast-conserving therapy: results of a survey," Annals of surgery **241**, 629-639 (2005).

16.	E. K. Valdes, S. K. Boolbol, I. Ali, S. M. Feldman, and J. M. Cohen, "Intraoperative touch preparation cytology for margin assessment in breast-conservation surgery: does it work for lobular carcinoma?," Ann Surg Oncol **14**, 2940-2945 (2007).

17.	T. P. Olson, J. Harter, A. Munoz, D. M. Mahvi, and T. Breslin, "Frozen section analysis for intraoperative margin assessment during breast-conserving surgery results in low rates of re-excision and local recurrence," Ann Surg Oncol **14**, 2953-2960 (2007).

18.	N. Cabioglu, K. K. Hunt, A. A. Sahin, H. M. Kuerer, G. V. Babiera, S. E. Singletary, G. J. Whitman, M. I. Ross, F. C. Ames, B. W. Feig, T. A. Buchholz, and F. Meric-Bernstam, "Role for intraoperative margin assessment in patients undergoing breast-conserving surgery," Ann Surg Oncol **14**, 1458-1471 (2007).

19.	G. C. Balch, S. K. Mithani, J. F. Simpson, and M. C. Kelley, "Accuracy of intraoperative

gross examination of surgical margin status in women undergoing partial mastectomy for breast malignancy," Am Surg **71**, 22-27; discussion 27-28 (2005).

20.	W. C. Shih, K. L. Bechtel, and M. S. Feld, "Intrinsic Raman spectroscopy for quantitative biological spectroscopy Part I: Theory and simulations," Opt. Express **16**, 12726-12736 (2008).

21.	P. Matousek, M. D. Morris, N. Everall, I. P. Clark, M. Towrie, E. Draper, A. Goodship, and A. W. Parker, "Numerical simulations of subsurface probing in diffusely scattering media using spatially offset Raman spectroscopy," Appl Spectrosc **59**, 1485-1492 (2005).

22.	A. M. K. Enejder, T.-W. Koo, J. Oh, M. Hunter, S. Sasic, M. S. Feld, and G. L. Horowitz, "Blood analysis by Raman spectroscopy," Opt. Lett. **27**, 2004-2006 (2002).

23.	S. Sathyendranath, and T. Platt, "Ocean-color model incorporating transspectral processes," Appl. Optics **37**, 2216-2227 (1998).

24.	K. Vishwanath, and M. A. Mycek, "Time-resolved photon migration in bi-layered tissue models," Opt Express **13**, 7466-7482 (2005).

25.	D. Passos, J. C. Hebden, P. N. Pinto, and R. Guerra, "Tissue phantom for optical diagnostics based on a suspension of microspheres with a fractal size distribution," Journal of biomedical optics **10**, 064036 (2005).

26.	M. R. Arnfield, J. Tulip, and M. S. McPhee, "Optical propagation in tissue with anisotropic scattering," IEEE transactions on bio-medical engineering **35**, 372-381 (1988).

27.	D. Grosenick, H. Wabnitz, K. T. Moesta, J. Mucke, P. M. Schlag, and H. Rinneberg, "Time-domain scanning optical mammography: II. Optical properties and tissue parameters of 87 carcinomas," Physics in medicine and biology **50**, 2451-2468 (2005).

28.	A. Cerussi, N. Shah, D. Hsiang, A. Durkin, J. Butler, and B. J. Tromberg, "In vivo absorption, scattering, and physiologic properties of 58 malignant breast tumors determined by broadband diffuse optical spectroscopy," Journal of biomedical optics **11**, 044005 (2006).

29.	B. J. Tromberg, N. Shah, R. Lanning, A. Cerussi, J. Espinoza, T. Pham, L. Svaasand, and J. Butler, "Non-invasive in vivo characterization of breast tumors using photon migration spectroscopy," Neoplasia (New York, N.Y **2**, 26-40 (2000).

30.	S. A. Prahl, M. J. C. Vangemert, and A. J. Welch, "Determining the Optical-Properties of Turbid Media by Using the Adding-Doubling Method," Appl. Optics **32**, 559-568 (1993).

31.	N. Ghosh, S. K. Mohanty, S. K. Majumder, and P. K. Gupta, "Measurement of optical transport properties of normal and malignant human breast tissue," Appl Opt **40**, 176-184 (2001).

CHAPTER VII

DEVELOPMENT OF SPATIALLY OFFSET RAMAN SPECTROSCOPY FOR

EVALUATING MARGIN STATUS AFTER PARTIAL MASTECTOMIES

7.1 Abstract

The risk of local recurrence for breast cancers is strongly correlated with the presence of tumor within 1-2 mm of the surgical margin on the excised specimen. From previous experimental results and Monte Carlo simulations, spatially offset Raman spectroscopy (SORS) holds much promise for intraoperative margin analysis. Based on simulation results, a SORS probe with multiple source-detector offsets was designed and tested. It was then used to acquire spectra from 35 frozen-thawed breast tissue samples *in vitro* and from a pilot set of six freshly excised breast specimens in the clinic. Spectra from each detector ring were averaged to create a composite spectrum covering the entire range from the tissue surface to ~2 mm below the surface. A probabilistic classification scheme was used to classify these composite spectra as "negative" or "positive" margins. For the *in vitro* measurements, this discrimination was performed with 95% sensitivity and 100% specificity, and for clinical measurements, it achieved 91% for both sensitivity and specificity.

7.2 Introduction

For many of the approximately 180,000 women diagnosed with early-stage invasive breast cancer or carcinoma *in situ* each year [1], a viable treatment option is breast conserving therapy (BCT). BCT involves a partial mastectomy, or lumpectomy, to remove only the primary

100

lesion with a small amount of surrounding normal tissue [2]. Depending on the hospital, the depth of normal tissue required from the surgical margin on the excised specimen to the tumor is typically 1-2 millimeters [3]. If tumor-positive margins are found, a second operation is necessary because positive margins are a major predictor of local tumor recurrence [4]. Currently available intraoperative margin evaluation tools all have significant drawbacks in terms of accuracy and/or time [5-7], so there is a need for an automated, real-time method to accurately evaluate surgical margins during BCT.

In the one report of using Raman spectroscopy for such a tool [8], measurements were made *in vivo* rather than on the excised specimen, as is the standard practice in surgical pathology. That study also used a conventional fiber optic probe with limited depth sensing. More recently, spatially offset Raman spectroscopy (SORS) has been shown to be a reliable method for recovering biological Raman spectra from depths greater than those possible with standard techniques [9-17]. It does so because detection elements spaced radially further from source elements are more sensitive to photons traveling deeper beneath the tissue surface and to greater radial distances due to multiple scattering. We have previously demonstrated the ability of SORS to detect spectral contributions from breast tumors under .5 to 2 mm of normal breast tissue [9]. In addition, a SORS Monte Carlo code was developed to thoroughly characterize signals obtained from layered constructs of normal breast tissue overlying breast tumors [9]. In particular, it was used to examine the effects of layer thicknesses and overall geometries on relative tumor contributions to observed spectra at a range of source-detector (S-D) offsets [18].

Combining the results of experimental [9] and numerically simulated [18] SORS indicated that to be sensitive to breast tumors up to 2 mm beneath normal breast tissue, as needed for surgical margin evaluation, a maximum S-D offset of ~3.5 mm should be used. With further

offsets, the measurements could possibly detect large tumors from over 2 mm deep and create false positives; recording spectra with adequate signal-to-noise ratios (SNRs) with further offsets is difficult as well. This manuscript describes the design of a multi-separation SORS probe based on the above findings, its testing to ensure comparable signal quality in each detector ring, and its use in acquiring spectra from both frozen-thawed breast tissue samples and a small number of freshly excised breast specimens in the clinic to evaluate margin status.

7.3 Materials and Methods

7.3.1 SORS Probe Design

The primary criterion for designing a SORS probe for breast margin analysis was to ensure proper depth sampling - that is, to develop a probe sensitive to tumor spectral signatures if the tumor is anywhere within the first 2 mm in depth from the excised surface. From the previous experimental [9] and simulation [18] results, a range of S-D offsets from 0.5 to 3.5 mm is appropriate to sample breast tissue from the surface to 2 mm below the surface. Another factor to consider given this range of offsets was the corresponding drop in SNR as S-D offset increases, since fewer photons can traverse long enough paths to reach the further offset detectors compared with closer offset detectors. To that end, SORS Monte Carlo simulations were run using the same model as for previous results [18]. Simulations were run for 3-layered samples, consisting of a top layer of 0.5 to 2 mm of normal breast tissue, a 0.1 to 20 mm thick middle layer of breast tumor, and then a 2 cm thick bottom layer of normal breast tissue to mimic the clinical situation of semi-infinite geometry. As a metric for SNR, the total number of Raman photons reaching each detector bin was counted and normalized to a maximum of 1, since we are only interested in how SNR falls off with S-D offset. Figure 7.1 shows the mean of these curves;

since the standard deviation was less than 1% over the range of thicknesses for the top two layers, no error bars are shown. As expected, the number of Raman photons detected fell off at an exponential decay as a function of S-D offset.
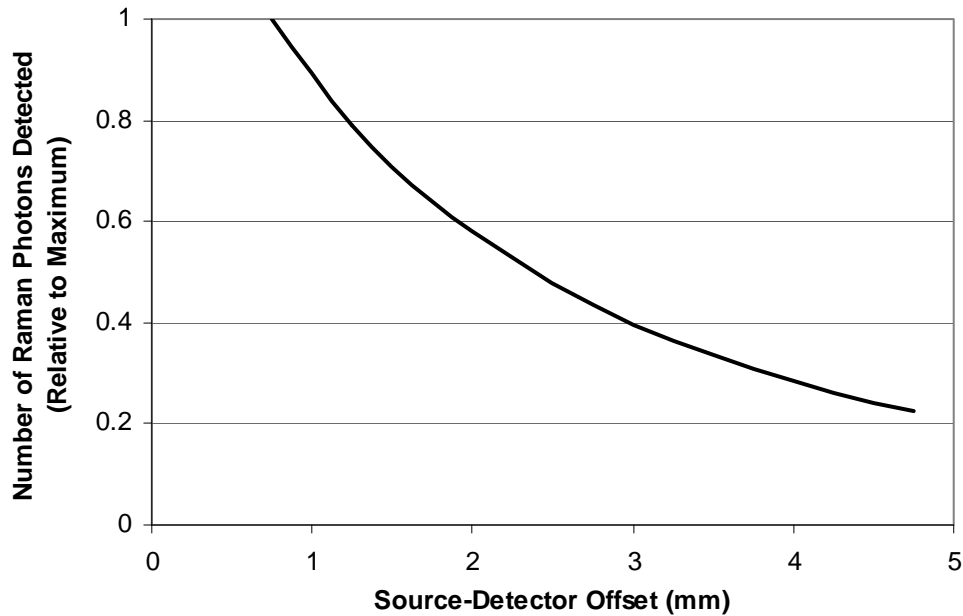
Figure 7.1 Total number of Raman photons detected as a function of S-D offset, normalized to a maximum of 1 and averaged for a variety of thicknesses of the top two tissue layers.

The above results were used to aid the design of a multi-separation SORS probe (assembled by EMVision, Loxahatchee, FL), whose distal tip is shown in Figure 7.2. A single 400 μm diameter excitation fiber is found on one end, and four (partial) rings of 300 μm diameter collection fibers extend radially outward. The excitation fiber includes a bandpass filter at its tip to clean up the laser line, and the collection fibers have longpass filters at their tips to reject elastically scattered light. The center to center distances of the excitation fiber to each detection ring are 0.5, 1.5, 2.5, and 3.5 mm. Based on Figure 7.1, an additional collection fiber was added to each consecutive detector ring to make the SNRs from each ring more comparable.

While the curve in Figure 7.1 is not linear, adding a single fiber between each ring provided the closest approximation of equivalent SNRs if all of the fibers in each ring were binned. Adding a fiber in each successive detector ring had an added benefit of increasing the sampling volume of the probe as well.
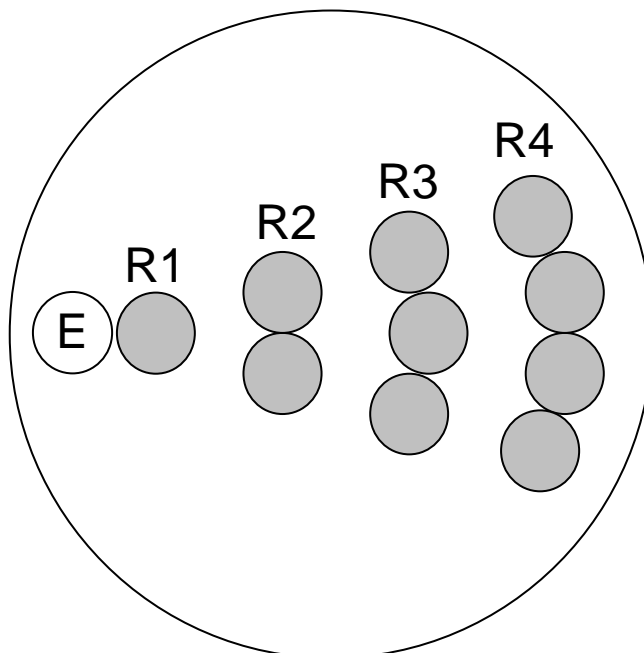
Figure 7.2 Schematic of tip of SORS probe. E – excitation fiber, gray circles – collection fibers. Each ring of collection fibers is separated by 1 mm (center to center) from the previous ring, with 0.5 mm between the excitation fiber and the first detector ring (R1).

7.3.2 Instrumentation and data processing

The SORS probe delivered 80 mW of power from a 785 nm diode laser (Innovative Photonics Solutions, Monmouth Junction, NJ). The collection fibers delivered light to a NIR-optimized spectrograph (Princeton Instruments, Princeton, NJ), which dispersed the light to be recorded by a deep depletion, thermo-electrically cooled CCD (Princeton Instruments).

Each acquisition with the SORS probe recorded four spectra – one from each detector ring. Each ring was calibrated separately since the inherent curvature in the detection system

created noticeable differences in peak locations on the CCD between different rings. A neon-argon lamp, naphthalene, and acetaminophen standards were used to calibrate the wavenumber axis, and a NIST-calibrated tungsten-halogen lamp was used to correct for the system response. After wavenumber binning and noise smoothing, the background fluorescence was subtracted with a modified polynomial fit algorithm [19], and the spectra were normalized according to their overall mean intensities. To create a composite spectrum from all four rings, which would contain information from the entire 2 mm sampling depth, the binned spectra from each of the four rings were averaged after processing.

7.3.3 SNR testing

To ensure the probe's ability to gather spectra from each ring with comparable SNRs, spectra were acquired for 20 seconds each from 12 different spots on a ~1 cm thick piece of chicken muscle. The spectra were processed as described in 7.2.2, and the SNR of the binned spectrum from each ring was calculated by dividing the height of the 1445 cm^{-1} peak by the standard deviation of the flat spectral range between the 1656 and 1750 cm^{-1} peaks.

7.3.4 *In vitro* sample measurements

With approval by the Vanderbilt Institutional Review Board (#050551) and the US Army Medical Research and Materiel Command's Human Research Protection Office (USAMRMC HRPO), fresh-frozen human breast tissue samples were acquired from the Cooperative Human Tissue Network. In total, 35 samples were included in the study; 15 samples had either no tumor or tumor > 2 mm beneath normal tissue at the point of measurement and were thus labeled as "negative margins," while 20 samples had tumor regions within the first 2 mm from the

measurement surface, and were thus labeled "positive margins." Wherever possible, measurements from tumor samples were taken such that the SORS probe was placed on a small region of visually normal-appearing tissue on top of the actual tumor to mimic the situation of margin evaluation. Spectra were recorded for 10-30 seconds and processed as above. Measurement sites were inked, fixed in formalin, and serially sectioned to correlate the spectra with histopathology diagnoses of tissue type and precise depths of those tissues. In this manner, the analysis was done to discriminate "negative" margins from "positive" margins.

7.3.5 *Ex vivo* measurements in clinic

With approval by the Vanderbilt IRB (#060554) and USAMRMC HRPO, patients undergoing partial or total mastectomy for the treatment of breast cancer were recruited and consented for this study by a participating surgeon. For partial mastectomies, the SORS probe was placed in light contact with the tissue at one spot on each of the six facets (lateral, superior, posterior, etc. margins) of the excised specimen. For total mastectomies, measurements were taken immediately upon sectioning, which was expedited in these cases to avoid the tissue having been removed from the body for any longer than ~20 minutes. Measurements were taken from at least one distant normal site, at least one site directly on the tumor, and at least two spots where it appeared that a small layer of normal tissue was overlying the tumor, again to mimic margin analysis. In all cases, measurement spots were inked and sectioned to obtain a histopathological diagnosis of margin status (or equivalently, the tissue types down to 2 mm below the measurement surface). In total, 5 tumor-positive and 19 tumor-negative measurement sites were obtained from 4 partial mastectomy specimens, and 5 tumor-positive and 4 tumor-negative spectra were obtained from 2 total mastectomy specimens.

7.3.6 Classification of margin status

In both the laboratory and clinical measurements, the composite spectrum from averaging all four detector rings was used for analysis, and if there were histological evidence of tumor cells within 2 mm of the measurement surface, the "margin" was considered positive. Discrimination was performed with sparse multinomial logistic regression (SMLR) [20], a Bayesian machine-learning framework that computes the posterior probability of a spectrum belonging to each tissue class based on a labeled training set. In the case of this binary analysis, whichever class had the higher probability of membership was the one to which the spectrum was classified. SMLR also includes inherent dimensionality reduction as it seeks to create sparse basis vectors, which is important for these data sets given their small sizes. Since each *in vitro* sample had only one measurement site, SMLR was run with leave-one-out cross-validation. For the clinical measurements, SMLR was performed with leave-one-*patient*-out cross-validation to avoid any undue bias.

7.4 Results

Figure 7.3 shows the results of the SNR testing on chicken muscle. Rings 1 and 4 of the SORS probe, with one and four fibers per ring, and with S-D offsets of 0.5 and 3.5 mm, respectively, displayed nearly identical SNRs. Rings 2 and 3 showed smaller SNRs compared with Ring 1, but only by ~30% and 20%, respectively. This trend was expected based on the shape of Figure 7.1, although the signal strengths of rings 2 and 3 were smaller than predicted by the simulations. The likely reason is that the detection fibers for the two middle rings were not able to be focused as tightly onto the CCD compared with the fibers for rings 1 and 4. Even so, the design of the SORS probe effectively accounted for SNR fall-off with increasing S-D offset.
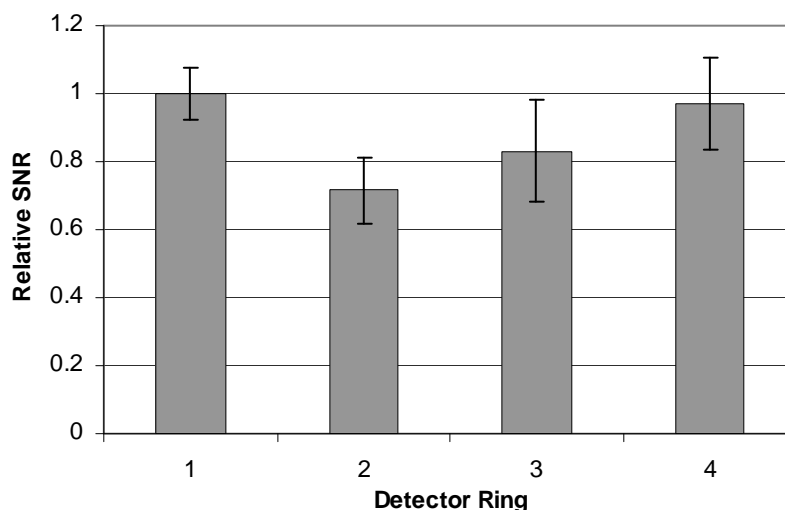
Figure 7.3 Mean (n=12) signal-to-noise ratios (SNR), plus or minus one standard deviation, for spectra of chicken muscle binned within each detector ring and normalized to SNR of first ring.

Figure 7.4 shows typical composite spectra recorded from pure normal breast tissue and pure breast tumor (invasive ductal carcinoma) tissue with the SORS probe.   As in the previous study [9], there are numerous spectral regions with major differences between the two tissue types.   In particular, tumor tissue contains a strong band at 1006 cm^{-1}, usually attributed to phenylalanine, while normal tissue does not; the ratios of the 1303 cm^{-1} to 1265 cm^{-1} bands are very different between the tissue types; the amide I band centered around 1656 cm^{-1} is much wider in tumor compared to normal; the 1445 cm^{-1} CH stretch band is relatively more intense in normal tissue; and the normal tissue contains a carbonyl stretch peak around 1750 cm^{-1}, while the tumor tissue does not.

Figures 7.5 and 7.6 show the H&E stained tissue section and the SORS spectra from that section from two *in vitro* tumor samples. In both Figures 7.5A and 7.6A, the "S" arrow indicates the placement of the source fiber, while "R1," "R2," etc. denote the location of the individual collection fiber rings.   In the tissue sample from Figure 7.5A, the probe was delivering light to a
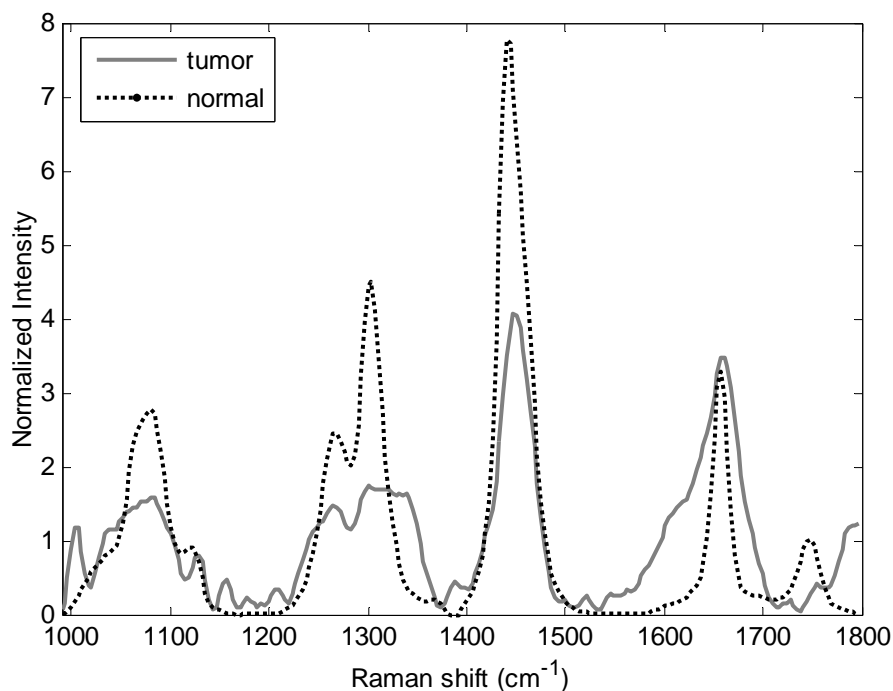
Figure 7.4 Typical composite spectra from SORS probe of normal breast tissue versus breast tumor (invasive ductal carcinoma) tissue.

large fatty area, as seen by the whitish lipid-filled vacuoles, while only the outermost collection fibers were placed over a portion of the invasive ductal carcinoma (IDC) tumor, which comprises the remainder of the darkly stained section. Although spectral differences among detector rings in Figure 7.5B are visually subtle, there are definite trends indicating that the closer rings are sampling normal tissue, while the outer rings are picking up slight spectral contributions from the tumor as well. By comparing the spectra in Figure 7.5B with the pure normal and tumor spectra from Figure 7.4, these trends are indicative of picking up some tumor signature including the increasing presence of the 1003 cm^{-1} peak, the lesser relative contributions from the 1303 and 1445 cm^{-1} peaks, and the increasing width of the 1656 cm^{-1} peak as source-detector offset increases. These trends are similar to those seen in the earlier report of SORS on layered breast tissues [9], but in this case, the tissue boundary was vertical rather than horizontal.
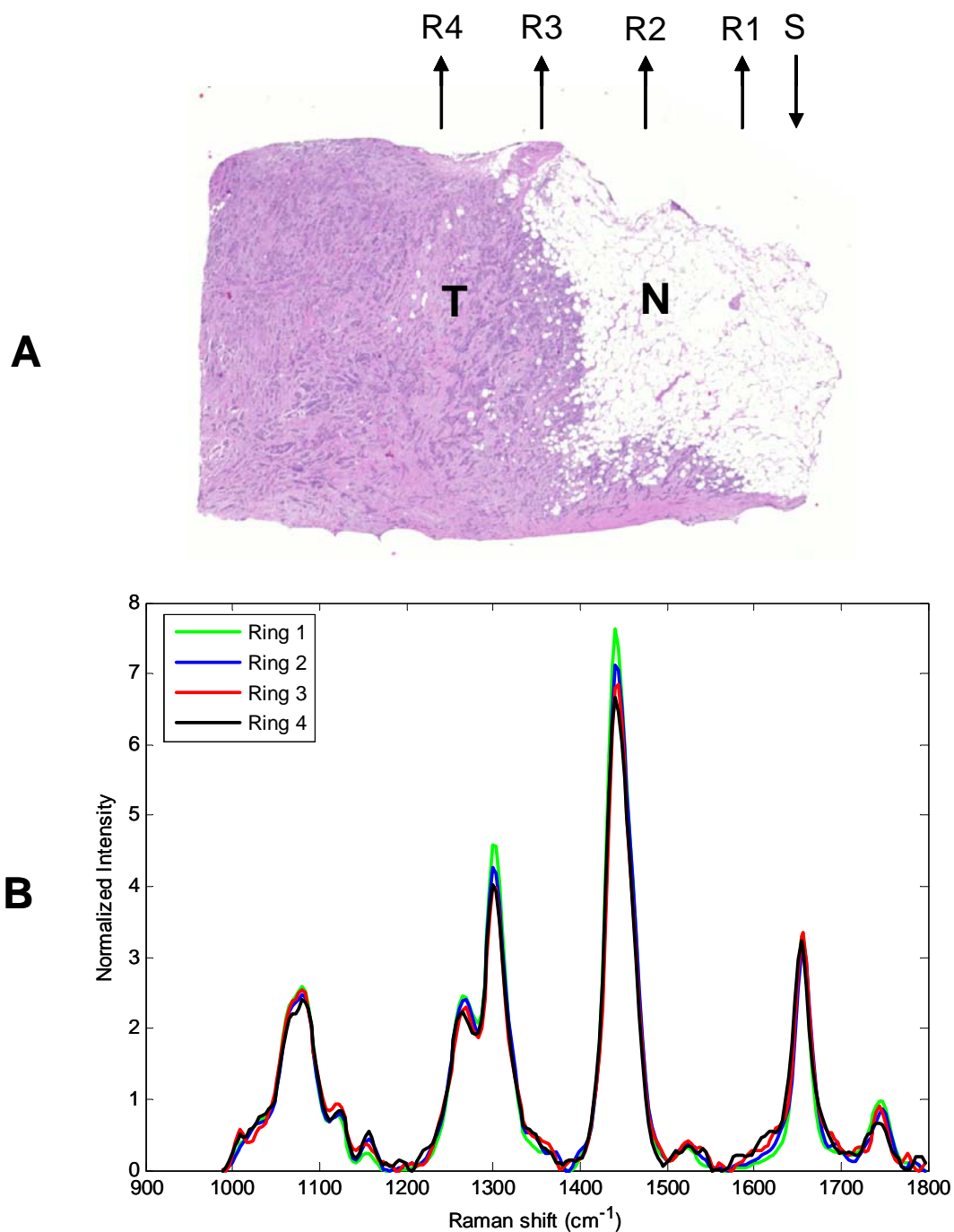
Figure 7.5 (A) H&E stained tissue section of IDC sample with large area of normal fat (white colored area with "N") on the right, and solid IDC tumor (darkly stained area with "T") on the left. Arrows indicate the placement of the source fiber (S) and each of the detector rings. (B) Binned SORS spectra for each detector ring from tissue in A.

The example in Figure 7.6 provides an illustration of what happens with smaller layers of normal tissue over a tumor. Figure 7.6A shows an invasive lobular carcinoma (ILC) sample with pockets of normal adipose cells near the surface, including directly under the location where the excitation fiber from the probe was placed. From Figure 7.6B, in comparison to Figure 7.4, the spectrum from the smallest S-D offset contains mostly features indicative of normal fatty breast tissue, while spectra from the further S-D offsets contain features indicative of tumor spectral signatures, as noted above. Thus, it is clear that the different detector rings are sampling different volumes, as desired.

To simplify the "margin analysis" procedure, the spectra from each detector ring were averaged to create one composite spectrum per *in vitro* sample. Thus, a single histological classification could be correlated to a single spectral classification. Table 7.1 shows the confusion matrix for classification of these composite spectra with SMLR. This analysis showed

Table 7.1. Confusion matrix for "margin analysis" on *in vitro* specimens.

		Spectral Margin Status		
		Negative	Positive	
Histopathology	Negative	15	0	Specificity: 100%
Margin Status	Positive	1	19	Sensitivity: 95%
		NPV: 94%	PPV: 100%	

an excellent ability for SORS to evaluate margin status in breast specimens, with sensitivity, specificity, negative predictive value (NPV), and positive predictive value (PPV) all at least 94%. The one false negative came from a tumor sample which, after formalin fixation and sectioning, was found to have a ~1.5 mm layer of normal tissue between the measurement site
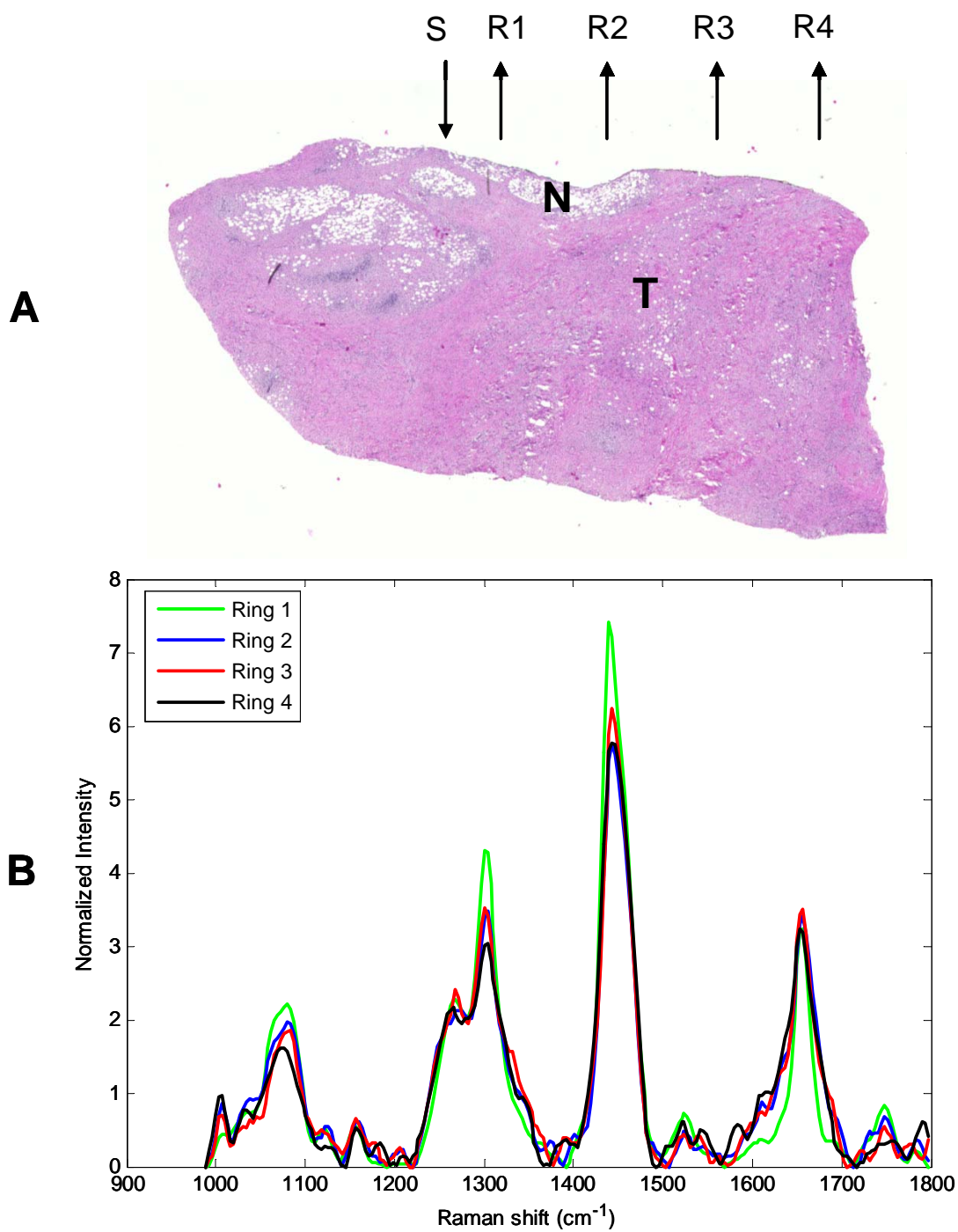
Figure 7.6 (A) H&E stained tissue section of invasive lobular carcinoma sample with pockets of normal fat ("N") near surface of otherwise darkly stained tumor tissue ("T"). Arrows again represent placements of fibers. (B) SORS spectra for each detector ring from tissue in A.

and the tumor. Since it has been shown that normal tissue margins tend to shrink by an average of 33% during formalin fixation [21], it is possible that this normal layer was at least 2 mm thick when the spectra were obtained.

Figure 7.7 shows an example set of composite spectra obtained in the hospital from the different margins of a single partial mastectomy specimen. Sites 1, 3, and 5 were deemed negative by pathology, although site 5 contained a mix of normal fibrous and scar tissue. Sites 2, 4, and 6 were found to be positive for ductal carcinoma *in situ* (DCIS), at depths of ~0.2, 0.5, and 1.3 mm below the surgical margin, respectively. These spectra show the same trends in relative peak ratios and widths between normal breast tissue and tumor-containing breast tissue seen in Figure 7.4, with the exception of the fibrous, scar-tissue-containing site 5.
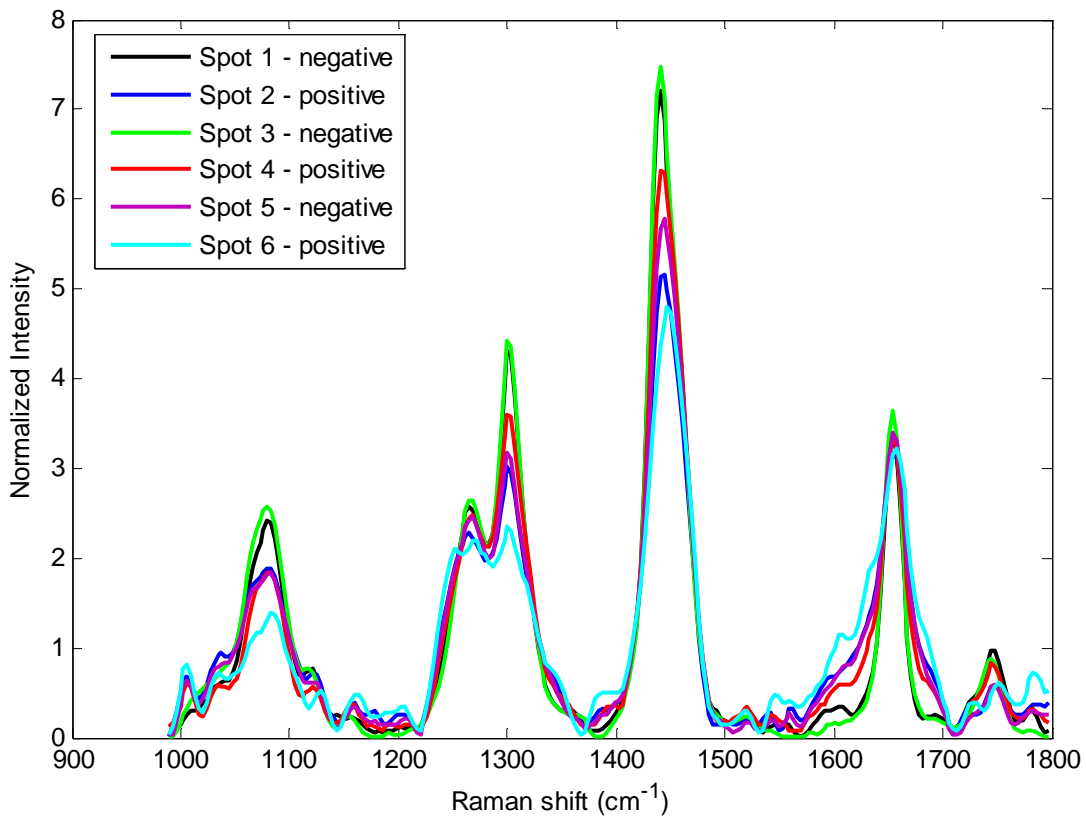
Figure 7.7 Composite spectra from each margin of an excised partial mastectomy specimen. Spectra 1, 3, and 5 were from negative margins, while 2, 4, and 6 were from positive margins.

Table 7.2. Confusion matrix for margin analysis on clinical specimens.

		Spectral Margin Status		
		Negative	Positive	
Histopathology	Negative	20	2	Specificity: 91%
Margin Status	Positive	1	10	Sensitivity: 91%
		NPV: 95%	PPV: 83%	

The SMLR-based margin analysis of the clinical specimens is displayed in Table 7.2. Overall, the classification performance was similar to the *in vitro* analysis, though instead of a single false positive and false negative, this analysis produced two false positives and one false negative. Given the small sample size, that reduced the PPV to 83%, although sensitivity, specificity, and NPV were all at least 91%. Those two false positives were spectra from very fibrous (representing >90% of tissue components) normal areas, although the scar tissue site in Figure 7.7 classified correctly. The false negative originated from a site at which the pathologist had a difficult time determining the exact margin size, but determined that it most likely constituted a tumor-positive margin.

7.5 Discussion

This manuscript presents the design and implementation of a multi-separation SORS probe for use in evaluating margin status following partial mastectomies. The design, as shown in Figure 7.2, was based on results from our earlier experimental and simulation-based studies [9, 18], and from the SNR simulation results from Figure 7.1. To ensure that the SNRs were comparable across the different detector rings, a series of measurements was performed using the

common soft tissue optical phantom of chicken breast. As seen in Figure 7.3, the design of adding an additional collection fiber for each further-offset ring worked well to keep the SNR of each ring no more than ~30% different from the others. Given the exponential shape of Figure 7.1, it would be very difficult to design a probe to both sample the desired depths in tissue and achieve even better equilibration of SNR among the various detector rings. Besides the SNR balancing, the probe design from Figure 7.2 also appeared to sample tissue to the expected depths based on earlier experimental [9] and simulation [18] results. This conclusion is supported by the success shown in Tables 7.1 and 7.2 for classifying spectra according to margin status; in addition, for a very limited sample size of layered tissues with known thicknesses, composite spectra detected significant tumor contributions under 1.5 mm and some tumor contributions under 2 mm, but none under 2.5 mm of normal human breast tissue (data not shown).

The ability of the detector rings to sample different volumes is seen in Figures 7.5 and 7.6. From Figure 7.5A, it is clear that the SORS probe was placed over two very different regions of tissue for that specimen. A very large area of normal fatty tissue was found directly under the excitation fiber and the first 2-3 detector rings, while the outermost 1-2 detector rings were placed against the tumor. Comparing Figure 7.5B to the pure normal and fat spectra from Figure 7.4, rings 1 and 2 show essentially no tumor spectral signatures. Given this, a standard Raman probe placed in the same spot would not detect any positive margin findings at this point. The 3rd and 4th rings of the probe were able to pick up slight tumor contributions though, indicating that they successfully sampled a different volume of tissue than the inner rings. A similar situation was seen in Figure 7.6, although there, only the first detector ring was sensitive to a small (< 1 mm thick) fat layer on the surface, while the outer rings sampled deeper / more

radially distal tissue volumes. It should be noted that in the processing of samples, the fat regions tend to shrink [21], so the measurement surface of that specimen was likely much more level during signal acquisition. Also, the specimen was cut after fixation and before sectioning to make the section contain only the interrogated tissue region, so the fibers were never placed over the very edge of any sample.

Given these findings regarding sampling depths and volumes, it was decided to use the composite spectra for margin analysis on intact breast specimens in the laboratory and in the clinic. Since the SNR is approximately equal in all four rings (see Figure 7.3), averaging them provides information about the entire sampling volume in a single spectrum. This method also simplifies the analysis procedure; if spectra from individual rings were used, it could be tricky to determine how to correlate certain ones with pathology findings. For example, although all spectra in Figures 7.5B and 7.6B were from tissue sites that would be deemed positive margins within the spatial extent of the probe, it is unlikely that the innermost rings were actually picking up any signal from tumor tissues. A possible approach for using the individual spectra would be to call a measurement site "positive" if any of the 4 spectra are predicted to be from a positive margin, but the issue comes in the training of such an algorithm for a retrospective analysis. Many normal-looking spectra, like ring 1 from Figure 7.5B, would be labeled as tumor and would likely cause difficulties for discrimination algorithms trying to create decision boundaries.

The results from using SMLR to classify the composite SORS spectra according to margin status are shown in Tables 7.1 and 7.2 for the laboratory and clinical measurements, respectively. The performance of the algorithm was similar in each case, with only one false negative for the laboratory measurements, and one false negative and two false positives for the clinical cases. Thus, sensitivity and specificity were both >90% for both analyses, and the NPV

and PPV disparities can be attributed to the different relative sample sizes of negative and positive margins for each analysis. In this clinical application, perhaps the most important variable is NPV, since a surgeon needs to be confident in any diagnosis of negative margin status to prevent recurrence of the disease. For both analyses, the NPV was determined by having a single false negative, though both such findings have likely explanations. For the *in vitro* false negative, the normal layer overlying the tumor was found to be ~1.5 mm thick, but prior to formalin fixation, this layer was likely around or slightly greater than 2 mm thick [21], which would surpass the sampling capabilities of the SORS probe. For the clinical false negative, the solid area of tumor was ~3.5 mm below the measurement surface, though there appeared to be smaller regions of tumor infiltrating up to within ~1 mm of the surface.

The false positive findings were from very dense, fibrous normal tissues, which have Raman signatures that can resemble those from tumors compared with those from fat. Both tumors and fibrous normal tissue contain a great deal of protein content, which is reflected in spectra with the presence of the 1006 cm^{-1} peak associated with phenylalanine residues in collagen, the greater width of the 1656 cm^{-1} peak from the amide I mode in peptide bonds, and the ratio of the amide III mode at 1265 cm^{-1} to the lipid-related peak at 1303 cm^{-1}. Several other fibrous-rich normal breast tissues were classified correctly, though, including the noted measurement site 5 from Figure 7.7 above.

Although these analyses were performed on fairly small sample sizes, they were still well-powered at the 95% level. A similar total number of spectra were obtained from both the laboratory and clinical studies, although only six total specimens were investigated to date to test the feasibility of using SORS for clinical breast margin analysis. A simpler binary diagnostic algorithm would seem like a more appropriate approach in these analyses, but the SMLR

algorithm was able to significantly reduce the dimensionality of the data from 232 variables (one per wavenumber) to three to perform its classification. In addition, SMLR provides a probability of class membership that would be very useful in a clinical application. A surgeon could act differently if the probability of a margin being negative is 99% versus 51%, although in either case, the diagnosis would be "negative." While it may not be possible to state broad, sweeping conclusions from this work's sample sizes, it has demonstrated the feasibility and promise of using SORS to evaluate margin status on intact breast specimens both in a laboratory and a clinical setting.

7.6 Acknowledgments

7.7 References

1.   American Cancer. Society, "Cancer Facts and Figures 2009," (American Cancer Society, Atlanta, 2009).

2.   K. I. Bland, and E. M. C. III, eds. *The Breast: Comprehensive Management of Benign and Malignant Disorders* (Saunders, St. Louis, 2004).

3.   A. Taghian, M. Mohiuddin, R. Jagsi, S. Goldberg, E. Ceilley, and S. Powell, "Current perceptions regarding surgical margin status after breast-conserving therapy: results of a survey," Annals of surgery **241**, 629-639 (2005).

4.   K. C. Horst, M. C. Smitt, D. R. Goffinet, and R. W. Carlson, "Predictors of local recurrence after breast-conservation therapy," Clin Breast Cancer **5**, 425-438 (2005).

5.   E. K. Valdes, S. K. Boolbol, I. Ali, S. M. Feldman, and J. M. Cohen, "Intraoperative touch preparation cytology for margin assessment in breast-conservation surgery: does it work for lobular carcinoma?," Ann Surg Oncol **14**, 2940-2945 (2007).

6.   T. P. Olson, J. Harter, A. Munoz, D. M. Mahvi, and T. Breslin, "Frozen section analysis for intraoperative margin assessment during breast-conserving surgery results in low rates of re-excision and local recurrence," Ann Surg Oncol **14**, 2953-2960 (2007).

7.   G. C. Balch, S. K. Mithani, J. F. Simpson, and M. C. Kelley, "Accuracy of intraoperative gross examination of surgical margin status in women undergoing partial mastectomy for breast malignancy," Am Surg **71**, 22-27; discussion 27-28 (2005).

8.   A. S. Haka, Z. Volynskaya, J. A. Gardecki, J. Nazemi, J. Lyons, D. Hicks, M. Fitzmaurice, R. R. Dasari, J. P. Crowe, and M. S. Feld, "In vivo margin assessment during partial mastectomy breast surgery using raman spectroscopy," Cancer Res **66**, 3317-3322 (2006).

9.   M. D. Keller, S. K. Majumder, and A. Mahadevan-Jansen, "Spatially offset Raman spectroscopy of layered soft tissues," Opt Lett **34**, 926-928 (2009).

10.   M. V. Schulmerich, J. H. Cole, J. M. Kreider, F. Esmonde-White, K. A. Dooley, S. A. Goldstein, and M. D. Morris, "Transcutaneous Raman Spectroscopy of Murine Bone In Vivo," Appl. Spectrosc. **63**, 286-295 (2009).

11.   N. A. Macleod, and P. Matousek, "Deep noninvasive Raman spectroscopy of turbid media," Appl Spectrosc **62**, 291A-304A (2008).

12.   N. A. Macleod, A. Goodship, A. W. Parker, and P. Matousek, "Prediction of sublayer depth in turbid media using spatially offset Raman spectroscopy," Analytical chemistry **80**, 8146-8152 (2008).

13.   N. Stone, R. Baker, K. Rogers, A. W. Parker, and P. Matousek, "Subsurface probing of calcifications with spatially offset Raman spectroscopy (SORS): future possibilities for the diagnosis of breast cancer," Analyst **132**, 899-905 (2007).

14.   M. V. Schulmerich, K. A. Dooley, T. M. Vanasse, S. A. Goldstein, and M. D. Morris, "Subsurface and transcutaneous Raman spectroscopy and mapping using concentric illumination rings and collection with a circular fiber-optic array," Appl Spectrosc **61**, 671-678 (2007).

15.   P. Matousek, "Deep non-invasive Raman spectroscopy of living tissue and powders," Chem Soc Rev **36**, 1292-1304 (2007).

16.   M. V. Schulmerich, K. A. Dooley, M. D. Morris, T. M. Vanasse, and S. A. Goldstein, "Transcutaneous fiber optic Raman spectroscopy of bone using annular illumination and a circular array of collection fibers," Journal of biomedical optics **11**, 060502 (2006).

17.   P. Matousek, E. R. Draper, A. E. Goodship, I. P. Clark, K. L. Ronayne, and A. W. Parker, "Noninvasive Raman spectroscopy of human tissue in vivo," Appl Spectrosc **60**, 758-763 (2006).

18.   M. D. Keller, R. H. Wilson, M.-A. Mycek, and A. Mahadevan-Jansen, "Numerical simulations of spatially offset Raman spectroscopy for breast tumor margin analysis," Optics express (in preparation).

19.   C. A. Lieber, and A. Mahadevan-Jansen, "Automated method for subtraction of fluorescence from biological Raman spectra," Appl Spectrosc **57**, 1363-1367 (2003).

20.   B. Krishnapuram, L. Carin, M. A. T. Figueiredo, and A. J. Hartemink, "Sparse multinomial logistic regression: Fast algorithms and generalization bounds," Ieee Transactions on Pattern Analysis and Machine Intelligence **27**, 957-968 (2005).

21.   B. H. Yeap, S. Muniandy, S. K. Lee, S. Sabaratnam, and M. Singh, "Specimen shrinkage and its influence on margin assessment in breast cancer," Asian journal of surgery / Asian Surgical Association **30**, 183-187 (2007).

CHAPTER VIII

SUMMARY AND CONCLUDING REMARKS

8.1 Summary and Integration

This dissertation focused on the development of optical spectroscopy as a tool for improving intraoperative evaluation of surgical margin status following partial mastectomies. Such a tool could have a major impact on breast cancer patients and the health care system by significantly reducing the number of re-excisions performed due to tumor-positive margins. Both combined autofluorescence and diffuse reflectance spectroscopy and Raman spectroscopy were pursued toward this end because of unique advantages possessed by each modality or combination of modalities.

The preliminary studies discussed in Chapter 3 [1] laid the foundation for the work that follows in the primary manuscripts (Chapters 4-7). They showed that Raman spectroscopy can classify breast tissues as normal, invasive cancer, carcinoma *in situ*, or fibroadenoma with 99% accuracy using a direct multi-class discrimination algorithm. While the overall classification accuracy for combined autofluorescence and diffuse reflectance was only 84%, the sensitivity and specificity for discriminating normal tissue from malignant tissues in general were close to 90% each. Based on classification performance, their objective nature, and the ability to be implemented rapidly in the operating room, both approaches would therefore improve on current intraoperative margin evaluation techniques. Each approach had its own advantages and disadvantages for further development. Combined fluorescence and reflectance, in its conventional form and in the ultraviolet/visible region (UV/Vis), cannot interrogate tissue as

deeply as would be desired for margin analysis, but it can be adapted into a wide-field multi-spectral imaging system to examine significant (1 inch diameter) portions of the excised specimens in a single recording. In addition, techniques such as including polarization optics had been demonstrated to enhance the depth information from these modalities [2]. Conversely, the near-infrared (NIR) light used for biological Raman spectroscopy has a deeper penetration depth compared with UV/Vis, although slight separations between the source and collection elements are still needed to collect significant signal from below approximately several hundred microns from the surface of tissue. Raman also has the advantage of providing more accurate classification, but because of its weak signal strength and equipment requirements, no work has been published on adapting Raman into a wide-field imaging modality.

Due to its significantly stronger signal and the availability in the laboratory of a multi-spectral imaging setup, the combined fluorescence and reflectance approach was investigated first. Chapter 4 details the clinical *ex vivo* study in which point-based spectra were acquired from 40 patients, and a probabilistic classification scheme was developed to discriminate between normal and malignant tissues with 85% specificity and 96% sensitivity. This study also showed the feasibility of obtaining multi-spectral images from an entire margin at once, as well as the ability of such images to demarcate between normal and malignant regions. One other finding of note was that fluorescence spectra from normal tissues in patients undergoing neo-adjuvant chemotherapy were significantly different in the region around 500 nm compared with normal spectra from non-chemo-treated patients. While these results were promising, I was never able to successfully get around the issue of the limited sampling depths of these modalities – approximately a few hundred microns for fluorescence, and slightly greater for reflectance. Polarized spectral imaging has been successfully implemented for enhancing superficial layer

spectra by rejecting deeper signatures [3, 4], but margin analysis requires the opposite situation. There had been demonstrations of enhancing fluorescence from deeper layers via polarization [2], but only in point form. A likely reason for the inability of polarized fluorescence imaging to do the same is the fundamental difference in photon paths between point spectroscopy form and imaging, as investigated by a previous student in the lab [5]. One could also use source-detector offsets with fluorescence and reflectance to increase the sampling depth. If the solution to the depth problem were to continue using a small-footprint, contact probe, though, I decided that investigating the use of spatially offset Raman would likely be more worthwhile given the classification advantages of Raman versus fluorescence and reflectance.

Chapter 5 then deals with my investigations into the feasibility of using SORS for discriminating two layers of soft tissue; specifically, layered constructs of normal human breast tissue over invasive breast cancer samples. SORS had only previously been used for detecting hard tissue under soft tissue; this problem is relatively straightforward because hard tissue like bone has strong Raman peaks not seen in soft tissue. Using the chemometric approach of a classical least squares algorithm, the relative contributions of the normal and tumor layers to the observed Raman spectra at a variety of S-D offsets were successfully determined. These results showed that relatively thick (~3-5 mm) tumor samples could be detected under up to 2 mm of normal breast tissue, but they also raised questions about the detection limits for this approach.

To answer those questions, a SORS Monte Carlo code was developed and is described in Chapter 6. The code was validated by comparing it to experimental results from Chapter 5. The code was used to show that the inclusion of coverslips in the initial experiments had only a minimal impact on the detected signals. It was then used to show how changing the tumor thickness affects the observed relative tumor contributions for normal tissue layers of 0.5, 1.0,

1.5, and 2.0 mm. For the two smaller normal layers, the size of the tumor layer dramatically affected the observed relative tumor contribution, while the effects were less dramatic under thicker normal layers. Similar findings were seen when an additional normal layer was added under the tumor – that is, the presence of this additional layer altered the shape of relative tumor contribution vs. S-D offset to a greater extent as both the top normal and tumor layers decreased in thickness.

Comparing points where the simulations and experiments did not agree in Chapter 6, it was determined that while the simulations could produce results of relative tumor contributions between 0 and 5%, in the experiments, the CLS results gave a value of 0 for relative tumor contributions at these same points. Thus, it was determined that this discrepancy likely indicated a lower threshold of tumor spectral contribution that could be detected above the noise in the experimental signals. By then applying this threshold to the numerous simulations over a range of normal and tumor layer thicknesses, it was determined that SORS is likely sensitive to a tumor layer only a few cells thick under 1 mm of normal tissue, and to a tumor layer of ~1 mm thick under a 2 mm normal layer. The simulations and experiments also indicated that a maximum S-D offset of about 3.5 mm would be ideal to achieve the above sampling depth characteristics while staying insensitive to any deeper tumors and while still being able to record spectra with adequate SNR in a clinically feasible time frame.

Based on the above results, a multi-separation SORS probe was designed. Chapter 7 describes this design and the initial testing on layered constructs (like those used in Chapter 5) to ensure that it was sensitive to tumors under 2 mm of normal breast tissue, but not under thicker normal layers. The SORS probe was then used to acquire spectra from intact, frozen-thawed human breast tissue specimens. Wherever possible, these measurements were done on small

layers of normal tissue overlying a tumor region. Using composite spectra obtained by averaging the four individual detector rings from the probe, margin status was evaluated with 95% specificity and 91% sensitivity. Similar measurements were also obtained from freshly excised specimens in the clinic from a small (N=6) patient cohort undergoing partial or total mastectomy. Results obtained in the same manner as for the laboratory measurements showed 91% each sensitivity and specificity, and a 95% negative predictive value. Thus, although sample sizes were limited, the feasibility of using SORS for evaluating surgical margins following partial mastectomies was demonstrated.

8.2 Major Conclusions

- Combined autofluorescence and diffuse reflectance spectroscopy can provide very good, but not excellent discrimination between normal and malignant human breast tissues. This discrimination can be extended into a wide-field multi-spectral imaging mode, but in both cases, the sampling depth is ultimately too limited for them to be implemented for surgical margin evaluation following partial mastectomies.

- Spatially offset Raman spectroscopy can discriminate between two layers of soft tissue whose spectra differ only in terms of relative ratios and widths of peaks. For the specific case of detecting breast tumors under normal breast tissue, this can be done with tumor layers as small as 1 mm thick under normal layers as thick as 2 mm. These sampling characteristics are nearly ideal for the case of margin analysis.

- It is possible to create an accurate, comprehensive Raman scattering Monte Carlo model without the need for over-simplifying assumptions. Such a model is an extremely valuable tool in answering questions that are difficult or impractical to study

experimentally, such as examining the effects on relative spectral contributions of numerous combinations of precise tissue layer thicknesses.

- A SORS probe can be designed that samples normal breast tissue to the clinically relevant depth of 2 mm by using multiple detector rings to simultaneously acquire spectra with comparable SNRs. A composite spectrum created by averaging these spectra contains all of the information needed to accurately determine margin status in both frozen-thawed and freshly excised breast tumor specimens.

8.3 Recommendations

The results presented in this dissertation lead to a number of future recommendations. On the most basic level, it appears that for breast surgical margin evaluation, SORS is a significantly stronger candidate than fluorescence and reflectance, so all comments will be directed toward that technique. For the next person to work on this project, there are two immediate research directions to pursue. On the experimental side, clinical SORS measurements need to be obtained from a larger (~30 total) patient population with the existing probe to be able to perform a well-powered statistical analysis of the technique's ability to evaluate margin status in a clinical environment. The other immediate recommendation is to continue working with Robert Wilson and Dr. Mary-Ann Mycek at the University of Michigan on the refinement of a Raman Monte Carlo code designed to model irregularly shaped tissue layers. In this way, the detection limits of a variety of tissue interface geometries could be investigated, rather than modeling everything as a planar slab.

After validating the use of the current SORS probe in a larger population, the next step will be to develop a method to examine larger areas of the tissue. The most straightforward way

would be to create a probe with multiple "units" of fibers arranged like the current SORS probe. If a large enough number of these units could be incorporated, it may prove necessary to use optical or mechanical switching techniques to avoid having to acquire multiple sets of detection equipment, which would create a cost burden toward the adoption of this technique. It may be advantageous to develop a completely different fiber-based array pattern for a larger probe as well; the developed Raman Monte Carlo code could prove useful for such an exercise. Another method to interrogate larger areas of tissue would make use of a de-focused collection system, as demonstrated by the initial developers of SORS [6]. This method would require a very high-powered laser and is even less efficient than standard SORS though.

There are a number of other factors related to this work worth addressing for future investigation. It is well known that as a woman ages, much of her dense, fibroglandular breast tissue is replaced by fat. These two types of normal breast tissue have distinct Raman spectra, so it is possible that SORS could encounter trouble trying to discriminate proteinacious tumors from dense normal tissue rather than from fatty tissue. A report by Feld et al. found that while they did observe differences in their tissue composition metrics (ratio of fat to collagen) as a function of age, these differences were considerably smaller than differences in the same metric between all types of normal tissue and malignant tissues [7]. Some of the normal samples used in the preliminary studies included in this dissertation were very fibrous as well, but the discrimination algorithm had no trouble correctly classifying all normal tissues [1].

Related to age, it may be interesting to examine how menopausal and other hormonal statuses affect the breast spectra. Studies in our lab on the cervix have shown that Raman can detect changes according to both menopausal status and location in the menstrual cycle [8, 9]. Similar hormone-related changes appear to exist in breast tissue [10, 11], but it is unclear how

much those changes would affect the Raman spectra. In practice, most breast cancer patients are older (peak age is in the 50's) and likely post-menopausal as well.

The final recommendations deal with treatment of the data. While the most relevant classification scheme is a binary one (i.e. negative versus positive margins), it is possible that classification could be improved by sub-dividing a general category, such as normal-fatty and normal-fibrous, or malignant-IDC and malignant-DCIS, etc. Based on the patient population for the study, it is unlikely that many "benign" tissues such as fibroadenomas would be encountered. A recent report also demonstrated the possible utility of combining Raman with NIR diffuse reflectance to be able to extract the "intrinsic Raman" signal that one would have observed if not for tissue scattering and absorption [12]. This could be a worthwhile development to investigate, especially for the furthest S-D offsets since the photons being detected there have typically encountered numerous scattering and potential absorption events.

8.4 Contributions to the Field and Societal Impact

Throughout the course of my Ph.D. work, I have made numerous contributions to my research field and have positively impacted society in a variety of ways. To my knowledge, I was the first person to demonstrate the ability to use SORS to discriminate layered soft tissues. Rather than simply showing the feasibility of a new technique and then moving on, I have developed this technique to be specifically suited for intraoperative surgical margin evaluation during BCT. As outlined in more detail at the end of Chapter 2, the successful implementation of this technique would have significant benefits for breast cancer patients and for the health care system. Beyond the scope of breast cancer, SORS could be implemented for other medical procedures with specific depth sampling requirements in soft tissues, such as helping to evaluate

or outline tumor margins extending beneath the visible surface of the skin or the prostate.

The development of a robust, detailed Raman Monte Carlo code has the potential to be a lasting contribution to the vibrational spectroscopy research field. Previously published Raman Monte Carlo algorithms were all lacking in terms of complexity and flexibility, but the code I developed (along with Robert Wilson of the University of Michigan) is the most complete one to date. As such, it could easily see widespread use for researchers working with Raman spectroscopy in either biological or non-biological fields.

While the general ability of fluorescence and reflectance to classify breast tissues was not a novel contribution to the field, some aspects of that study were. In particular, I was the first, to my knowledge, to show the changes in autofluorescence spectra associated with chemotherapy treatment, and how that change is similar to one seen in radiation-treated tissues [13]. I was also the first, again to my knowledge, to show that multi-spectral images of breast tissues could clearly delineate normal from malignant tissues with high spatial resolution. Although this will not likely have a lasting effect on margin analysis, it could prove useful in other medical applications with shallower depth sampling requirements, such as demarcating tumors on the surface of exposed tissues.

8.5 Protection of Research Subjects

As stated in the methods sections of the relevant chapters, all tissue samples were collected, after having been de-identified, with approval from the Vanderbilt Institutional Review Board (#050551) and the Department of Defense Human Research Protection Office. For clinical measurements, informed written consent was obtained by a participating surgeon in a process approved by the Vanderbilt IRB (#060554) and the DOD HRPO. Since measurements

were taken on tissues after they were excised, the patient's medical care was not directly affected by the research studies.

8.6 References

1.   S. K. Majumder, M. D. Keller, F. I. Boulos, M. C. Kelley, and A. Mahadevan-Jansen, "Comparison of autofluorescence, diffuse reflectance, and Raman spectroscopy for breast tissue discrimination," J Biomed Opt **13**, 054009 (2008).

2.   N. Ghosh, S. K. Majumder, H. S. Patel, and P. K. Gupta, "Depth-resolved fluorescence measurement in a layered turbid medium by polarized fluorescence spectroscopy," Opt Lett **30**, 162-164 (2005).

3.   A. N. Yaroslavsky, E. V. Salomatina, V. Neel, R. Anderson, and T. Flotte, "Fluorescence polarization of tetracycline derivatives as a technique for mapping nonmelanoma skin cancers," J Biomed Opt **12**, 014005 (2007).

4.   D. Roblyer, R. Richards-Kortum, K. Sokolov, A. K. El-Naggar, M. D. Williams, C. Kurachi, and A. M. Gillenwater, "Multispectral optical imaging device for in vivo detection of oral neoplasia," J Biomed Opt **13**, 024019 (2008).

5.   S. C. Gebhart, S. K. Majumder, and A. Mahadevan-Jansen, "Comparison of spectral variation from spectroscopy to spectral imaging," Appl Opt **46**, 1343-1360 (2007).

6.   C. Eliasson, M. Claybourn, and P. Matousek, "Deep subsurface Raman spectroscopy of turbid media by a defocused collection system," Appl Spectrosc **61**, 1123-1127 (2007).

7.   A. S. Haka, K. E. Shafer-Peltier, M. Fitzmaurice, J. Crowe, R. R. Dasari, and M. S. Feld, "Diagnosing breast cancer by using Raman spectroscopy," Proc Natl Acad Sci U S A **102**, 12371-12376 (2005).

8.   E. M. Kanter, S. Majumder, E. Vargis, A. Robichaux-Viehoever, G. J. Kanter, H. Shappell, H. W. Jones, and A. Mahadevan-Jansen, "Multiclass discrimination of cervical precancers using Raman spectroscopy," Journal of Raman Spectroscopy **40**, 205-211 (2009).

9.   E. M. Kanter, S. Majumder, G. J. Kanter, E. M. Woeste, and A. Mahadevan-Jansen, "Effect of hormonal variation on Raman spectra for cervical disease detection," American Journal of Obstetrics and Gynecology **200**, - (2009).

10.   S. P. Weinstein, E. F. Conant, C. M. Sehgal, I. P. Woo, and J. A. Patton, "Hormonal variations in the vascularity of breast tissue," J Ultrasound Med **24**, 67-72; quiz 74 (2005).

11.   R. Ramakrishnan, S. A. Khan, and S. Badve, "Morphological changes in breast tissue with menstrual cycle," Mod Pathol **15**, 1348-1356 (2002).

12.   W. C. Shih, K. L. Bechtel, and M. S. Feld, "Intrinsic Raman spectroscopy for quantitative biological spectroscopy Part I: Theory and simulations," Opt. Express **16**, 12726-12736 (2008).

13.   W. C. Lin, A. Mahadevan-Jansen, M. D. Johnson, R. J. Weil, and S. A. Toms, "In vivo optical spectroscopy detects radiation damage in brain tissue," Neurosurgery **57**, 518-525; discussion 518-525 (2005).

APPENDIX 1

ROLE OF THE STUDENT IN THE MANUSCRIPTS

Chapter III (Preliminary Studies) – I am co-first author of the full-length manuscript that was condensed to comprise this chapter. It was published in September 2008 in the *Journal of Biomedical Optics*.

Chapter IV – I am first author on this paper, which has been accepted for publication in an upcoming issue of *Lasers in Surgery and Medicine*.

Chapter V – I am the first author of this paper, which was published in April 2009 in *Optics Letters*.

Chapter VI – I am the co-first author of this paper, and am responsible for all of the writing except for two paragraphs in the Methods section. A slightly modified version has been submitted to *Applied Spectroscopy* for review.

Chapter VII – I am the first author of this paper. A version without the clinical data has been submitted to *Journal of Biomedical Optics* for review.